



Metal-rich SX Phe stars in the *Kepler* field

James M. Nemec,^{1,2*} Luis A. Balona,³ Simon J. Murphy,⁴ Karen Kinemuchi⁵ and Young-Beom Jeon⁶

¹Department of Physics and Astronomy, Camosun College, Victoria, British Columbia, V8P 5J2, Canada

²International Statistics and Research Corp., Brentwood Bay, British Columbia, V8M 1R3, Canada

³South African Astronomical Observatory, PO Box 9, Observatory 7935, Cape Town, South Africa

⁴Sydney Institute for Astronomy (SIfa), School of Physics, The University of Sydney, NSW 2006, Australia

⁵Apache Point Observatory, Sunspot, New Mexico 88349, USA

⁶Korea Astronomy and Space Science Institute, Daejeon, 34055, Korea

Accepted 2016 November 23. Received 2016 October 29; in original form 2016 August 29

ABSTRACT

A spectroscopic and photometric analysis has been carried out for 32 candidate SX Phe variable blue straggler stars in the *Kepler* field. Radial velocities (RVs), space motions (U , V , W), projected rotation velocities ($v \sin i$), spectral types and atmospheric characteristics (T_{eff} , $\log g$, [Fe/H], ξ_t , ζ_{RT} , etc.) are presented for 30 of the 32 stars. Although several stars are metal-weak with extreme halo orbits, the mean [Fe/H] of the sample is near-solar, thus the stars are more metal-rich than expected for a typical sample of Pop. II stars and more like halo metal-rich A-type stars. Two-thirds of the stars are fast rotators with $v \sin i > 50 \text{ km s}^{-1}$, including four stars with $v \sin i > 200 \text{ km s}^{-1}$. Three of the stars have (negative) RVs $> 250 \text{ km s}^{-1}$, five have retrograde space motions and 21 have total speeds (relative to the Local Standard of Rest) $> 400 \text{ km s}^{-1}$. All but one of the 30 stars have positions in a Toomre diagram consistent with the kinematics of *bona fide* halo stars (the exception being a thick-disc star). Observed Rømer time delays, pulsation frequency modulations and light curves suggest that at least one-third of the stars are in binary (or triple) systems with orbital periods ranging from 2.3 d to more than four years.

Key words: stars: abundances – blue stragglers – stars: kinematics and dynamics – stars: oscillations – stars: Population II – stars: variables: δ Scuti.

1 INTRODUCTION

SX Phoenecis stars are the Pop. II counterparts of Pop. I δ Scuti pulsating variable stars (see Breger 1980; Eggen & Iben 1989; Nemec 1989; Nemec & Mateo 1990a,b). The best known and nearest examples are the stars SX Phe, DY Peg, BL Cam and KZ Hya. These and other such field SX Phe stars (i.e. those not in star clusters) generally have the kinematics of halo (or thick-disc) stars, asymmetric and large-amplitude light curves and low metallicities (Eggen 1970, 1979; Breger 1975, 1977a,b; McNamara et al. 1978, 2007). For many years, SX Phe stars were suspected of being Pop. II blue stragglers (BSs), but this was established only when short-period variable stars were found among the BSs in globular clusters (Niss 1981; Jørgensen 1982; Jørgensen & Hansen 1984; Jensen & Jørgensen 1985; Nemec & Harris 1987; DaCosta, Norris & Villumsen 1986; Nemec 1989; Nemec & Cohen 1989; Mateo et al. 1990; Nemec et al. 1994, 1995; Sarajedini 1993; Fusi Pecci

et al. 1992; McNamara 1997; Gilliland et al. 1998; Rodríguez & López-González 2000; Bruntt et al. 2001). The leading theory of the formation mechanism for BSs involves mass transfer in a close binary system (Hoyle 1964; McCrea 1964; Eggen & Iben 1989; Leonard 1989). Since many BSs are now known to be eclipsing binaries (Niss et al. 1978; Margon & Cannon 1989; Mateo et al. 1990; Nemec & Mateo 1990a,b; Hobbs & Mathieu 1991; Hodder et al. 1992; Kallrath et al. 1992; Helt et al. 1993; Yan & Mateo 1994; Nemec et al. 1995; Kaluzny et al. 1996, 2007; Kaluzny 2000; Park & Nemec 2000; Preston & Sneden 2000; Carnegy et al. 2001, 2005; Cohen & Sarajedini 2012), it follows that SX Phe stars are also likely to have a binary (or triple star) nature.

When the first globular cluster SX Phe stars were discovered, they were found to have pulsation amplitudes, A_V , larger than 0.10 mag and simple light curves consistent with radial pulsation and one or two dominant periods. Their location in the faint extension of the Cepheid instability strip implies pulsation due to Eddington's κ -mechanism operating in the He II partial ionization zone (see Fiorentino et al. 2014, 2015). They also were found to obey a well-defined period–luminosity relationship that can be used to estimate distances (see Nemec et al. 1994; McNamara 1997, 2011;

* E-mail: jmn@isr.bc.ca (JMN); lab@sao.ac.za (LAB); simon@simonmurphy.info (SJM)

Petersen & Hog 1998; Sandage & Tamman 2006). Because globular clusters (and Local Group dwarf galaxies) tend to be distant, the SX Phe stars in these systems are quite faint. Moreover, the BSs in globular clusters tend to be centrally concentrated (Nemec & Harris 1987; Nemec & Cohen 1989; Leigh, Sills & Knigge 2011; Ferraro et al. 2015) and as a consequence, the SX Phe stars are often located in the crowded central regions and therefore are much less amenable to spectroscopic and photometric analysis than those in the field.

Subsequent discoveries revealed that SX Phe stars include lower amplitude pulsators and stars that exhibit more complex radial and non-radial oscillations than previously thought to be the case. Particularly noteworthy was the observation that the A_V amplitude distribution shown in fig. 2 of Kaluzny (2000) shows an increase in the number of SX Phe stars down to the detection limit ($\sim 0.02\text{--}0.03$ mag) of the Warsaw variability surveys, from which it was concluded that ‘a significant fraction of SX Phe stars residing in the survey clusters were most likely missed.’ Over the years, many more faint and pulsationally complex SX Phe stars have been found in 47 Tuc (Gilliland et al. 1998), NGC 3201 (Mazur et al. 2003), NGC 5466 (Jeon et al. 2004), ω Cen (Olech et al. 2005) and other clusters. The catalogue compiled by Cohen & Sarajedini (2012) lists ~ 250 SX Phe stars in 46 galactic globular clusters (see their fig. 5).

SX Phe stars are now known to be ubiquitous, with many having been identified in our Galaxy (Ramsay et al. 2011; Palaversa et al. 2013; Preston 2015), in the Magellanic Clouds (Soszynski et al. 2002, 2003) and in most Local Group dwarf galaxies (Nemec & Mateo 1990a; Mateo et al. 1998; Pych et al. 2001; Poretti et al. 2008; McNamara 2011; Vivas & Mateo 2013; Ferraro et al. 2015; Fiorentino et al. 2014, 2015; Momany 2015; Coppola et al. 2015; Martínez-Vázquez et al. 2016). Despite these numerous discoveries, discrimination between SX Phe stars and δ Sct stars can be confusing and is particularly blurred where multiple and composite stellar populations have overlapping age, metallicity and kinematic distributions.

In 2012, Balona & Nemec (hereafter BN12) identified 34 candidate SX Phe stars in the *Kepler* field. The stars were found by cross-referencing a list of 1424 *Kepler*-field δ Sct stars (Balona 2014a) with the UCAC3 proper motion catalogue (Zacharias et al. 2010) and selecting those stars with high proper motions, $\mu > 30 \text{ mas yr}^{-1}$, and large tangential velocities, $V_t > 120 \text{ km s}^{-1}$. Several of the candidates are located more than 0.5 kpc above the Galactic plane, thereby strengthening the conclusion that the sample consists of Pop. II stars. An H–R diagram showing the locations of the 34 candidate SX Phe stars (and 1554 δ Sct stars) relative to stellar evolutionary tracks for masses ranging from 0.8 to $2.0 M_\odot$ was plotted by BN12, where the luminosities and effective temperatures were taken from the *Kepler* Input Catalogue (KIC; Brown et al. 2011). Since the physical quantities given in the KIC were derived mainly from photometric relations established for stars cooler than 7000 K, the atmospheric parameters given in the KIC were not expected to be particularly reliable. BN12 found that there was little to distinguish the *Kepler* light curves of the candidate SX Phe stars from those of δ Sct stars. Furthermore, whereas many field SX Phe stars have one or two dominant pulsation modes and rather high amplitudes, almost all of the *Kepler*-field candidates were found to have relatively low amplitudes and complex Fourier spectra. Thus, BN12 concluded that previous ground-based field SX Phe star investigations probably suffer from a selection bias that resulted in the omission of stars with the lowest amplitudes and most complex pulsations.

The goal of this study was to derive reliable estimates of the physical characteristics of the BN12 SX Phe candidates. Extensive asteroseismic investigations using *Kepler* photometry have already been reported for two of the stars: KIC 11754974, an SX Phe pulsator in a 343-d non-eclipsing binary system (Murphy et al. 2013b); and KIC 9244992, an SX Phe star in which both the surface and core exhibit slow, nearly uniform rotation (Saio et al. 2015). Since the SX Phe stars in the *Kepler* field are unique in having four years of almost-continuous high-precision photometry, estimation of their evolutionary status and atmospheric and physical characteristics based on high-resolution spectra is possible and obviously desirable. Moreover, if the stars are Pop. II BSs, then determining whether they are binary or triple systems (with a range of separations, including coalesced binaries) and better characterizing their orbital properties becomes important.

In Section 2, the results of the spectroscopic analyses are presented, including atmospheric properties, radial velocities (RVs), space motions and stellar population classifications (e.g. halo, thick disc). In Section 3, frequency analyses are described for the complete BN12 sample; the results based on all the available long- and short-cadence (SC) Q0–Q17 *Kepler* photometry are presented, including the finding that one-third of the SX Phe pulsators are in binary systems with orbital periods ranging from a few days to more than four years. A summary of the paper is given in Section 4.

2 SPECTROSCOPY

High-resolution echelle spectra for 32 of the BN12 candidate SX Phe stars were acquired in 2013 and 2014 with the ESPaDOnS spectrograph mounted on the Canada–France–Hawaii 3.6-m telescope (CFHT). Two stars fainter than 15th magnitude, KIC 5390069 and KIC 7300184, were too faint to be observed. A total of 178 SX Phe star spectra were taken by the CFHT Queue Service Observing team, with the number of spectra taken per star ranging from 3 to 11, over three to seven independent epochs. Details of the individual spectra are summarized in Table 1.

In 2013, ESPaDOnS was used in ‘star+sky’ mode (spectral resolving power $\lambda/\Delta\lambda \sim 66\,000$) with spectral resolution (Gaussian full width at half-maximum, FWHM, of instrumental profile) $\sim 0.0083 \text{ nm}$ at 550 nm , 2.5 pixels per resolution element and velocity resolution 4.5 km s^{-1} . In 2014, ‘star-only’ mode was used, which widened the stellar spectra, increased the resolving power to $\sim 80\,000$, reduced the FWHM of the instrumental profile to $\sim 0.0070 \text{ nm}$ and improved the velocity resolution to 3.8 km s^{-1} . Each spectrum covers the wavelength range $370\text{--}1030 \text{ nm}$, spread over 40 orders. Almost all the observations were made under photometric conditions. Starting in 2014, several IAU faint RV standard stars, selected from the list given by Udry, Mayor & Queloz (1999), were observed each night in addition to the programme stars (Table 1). All raw spectra were preprocessed using the ‘LIBRE-ESPRIT’/‘UPENA’ CFHT pipeline (see Donati et al. 1997). The reductions included barycentric velocity corrections, small RV corrections based on the telluric lines and rectification of the spectra. The Versatile Wavelength Analysis (vwa) ‘RAINBOW’ program (Bruntt et al. 2010b, Bruntt et al. 2010a) was used to merge the overlapping echelle orders and to improve, where necessary, the normalization of the continuum level. Sample spectra for the 32 observed stars are shown in Fig. 1.

High-resolution spectra also were taken at the Apache Point Observatory (APO) with the ARCES echelle spectrograph on the Astrophysical Research Consortium 3.5-m telescope. Some of the spectra were of well-known field SX Phe stars taken for comparison

Table 1. Summary of CFHT and APO spectra. The stars are ordered by KIC number (column 1) and the other columns contain: (2) the spectrum number (CFHT or APO); (3) the UTC mid-exposure date and time; (4) mid-exposure barycentric Julian Day; (5) exposure time (s); (6) signal-to-noise ratio; (7) airmass at the mid-time of the observation; (8) barycentric RV (km s^{-1}); and (9) projected equatorial velocity, $v \sin i$ (km s^{-1}). For the SB2 system KIC 6780873, the RV and $v \sin i$ entries are for the primary component.

KIC (1)	Spectrum (2)	UTC date (mid) (3)	BJD (mid) (4)	Exp.(s) (5)	S/N (6)	AM (7)	RV (8)	$v \sin i$ (9)
(a) <i>Kepler</i> -field SX Phe stars								
1162150	APO (15a)	2012/10/25, 04:31:53	2456225.6893	600	30	1.60	-11 ± 9	195 ± 7
	1650050 (15b)	2013/08/26, 08:15:58	2456530.8490	1800	148	1.06	-15 ± 7	226 ± 2
	1650642 (15c)	2013/08/29, 08:49:18	2456533.8720	1800	155	1.10	-16 ± 6	230 ± 2
	APO (15d)	2014/06/13, 05:59:35	2456821.7521	1200	30	1.26	-13 ± 6	194 ± 4
	APO (15e)	2014/06/13, 06:28:49	2456821.7724	1200	26	1.18	-13 ± 9	219 ± 5
	1733894 (15f)	2014/08/18, 11:25:36	2456887.9809	1200	106	1.43	-17 ± 5	228 ± 2
3456605	1650650 (24a)	2013/08/29, 11:48:46	2456533.9968	1350	51	1.79	-7.5 ± 0.5	13.6 ± 0.8
	1653557 (24b)	2013/09/14, 08:02:23	2456549.8388	1350	52	1.11	-6.4 ± 0.5	10.0 ± 1.0
	1741394 (24c)	2014/09/17, 06:19:24	2456917.7672	1200	52	1.06	-8.4 ± 0.5	16.2 ± 0.8
4168579	1650649 (23a)	2013/08/29, 11:24:43	2456533.9801	1200	38	1.63	33 ± 6	207 ± 6
	1653555 (23b)	2013/09/14, 07:17:38	2456549.8077	1200	37	1.07	23 ± 9	201 ± 5
	1670335 (23c)	2013/11/19, 04:25:45	2456615.6832	1200	45	1.21	19 ± 4	196 ± 4
	1670336 (23d)	2013/11/19, 04:46:26	2456615.6976	1200	39	1.26	20 ± 4	208 ± 9
	1670337 (23e)	2013/11/19, 05:07:07	2456615.7119	1200	39	1.34	24 ± 3	197 ± 7
	1733877 (23f)	2014/08/18, 06:01:35	2456887.7560	1200	40	1.24	24 ± 8	178 ± 6
4243461	1649174 (4a)	2013/08/22, 07:18:51	2456526.8091	1200	38	1.06	58.2 ± 1.3	53.0 ± 2.8
	1649175 (4b)	2013/08/22, 07:39:32	2456526.8235	1200	35	1.06	57.8 ± 0.3	50.0 ± 2.2
	1649176 (4c)	2013/08/22, 08:00:13	2456526.8378	1200	35	1.07	59.0 ± 1.9	50.1 ± 3.3
	1650640 (4d)	2013/08/29, 07:59:07	2456533.8368	1200	37	1.09	58.8 ± 1.2	56.7 ± 2.2
	1654451 (4e)	2013/09/17, 05:02:14	2456552.7129	1200	46	1.08	58.6 ± 0.8	52.2 ± 2.4
	1733876 (4f)	2014/08/18, 05:39:33	2456887.7403	1200	36	1.20	61.8 ± 0.9	55.3 ± 2.0
	1740694 (4g)	2014/09/14, 05:46:20	2456914.7437	1200	40	1.06	62.4 ± 1.4	53.3 ± 3.7
	1753084 (4h)	2014/10/31, 05:09:04	2456961.7143	1200	36	1.21	62.9 ± 1.7	52.8 ± 1.6
4662336	1650048 (14a)	2013/08/26, 07:27:05	2456530.8151	1200	48	1.07	-11.4 ± 0.2	81.5 ± 1.6
	1650049 (14b)	2013/08/26, 07:47:46	2456530.8295	1200	52	1.06	-11.1 ± 0.4	84.1 ± 1.5
	1650647 (14c)	2013/08/29, 10:41:23	2456533.9499	1200	60	1.39	-10.1 ± 0.6	82.4 ± 1.6
	1741395 (14d)	2014/09/17, 06:41:53	2456917.7827	1200	52	1.07	-16.9 ± 1.7	84.1 ± 1.3
4756040	1650485 (20a)	2013/08/28, 09:45:15	2456532.9110	1200	46	1.19	3.3 ± 0.7	43.0 ± 1.0
	1650486 (20b)	2013/08/28, 10:05:55	2456532.9254	1200	46	1.25	8.3 ± 0.5	34.0 ± 1.1
	1653556 (20c)	2013/09/14, 07:39:01	2456549.8226	1200	46	1.10	4.7 ± 1.0	43.4 ± 1.1
	1741396 (20d)	2014/09/17, 07:04:15	2456917.7983	1200	46	1.08	3.2 ± 1.0	44.2 ± 0.6
5036493	APO (26a)	2012/10/25, 09:56:58	2456225.6652	600	17	1.28	-1.8 ± 1.8	24.9 ± 2.5
	1653322 (26b)	2013/09/13, 05:09:41	2456548.7192	1200	80	1.16	-3.4 ± 1.0	20.6 ± 0.5
	1655649 (26c)	2013/09/22, 07:29:17	2456557.8156	1200	80	1.11	-3.5 ± 0.7	18.4 ± 0.6
	1741397 (26d)	2014/09/17, 07:27:08	2456917.8144	1200	64	1.09	-5.8 ± 0.4	16.1 ± 0.7
5705575	1650644 (22a)	2013/08/29, 09:37:19	2456533.9053	1200	39	1.21	-31.7 ± 2.4	88.6 ± 1.7
	1653554 (22b)	2013/09/14, 06:56:00	2456549.7926	1200	37	1.08	-33.7 ± 1.0	92.6 ± 1.8
	1656478 (22c)	2013/09/26, 04:57:03	2456561.7092	1200	49	1.09	-35.0 ± 2.1	89.3 ± 1.7
	1670338 (22d)	2013/11/19, 05:28:43	2456615.7269	1200	37	1.49	-30.4 ± 1.4	83.3 ± 2.2
	1670339 (22e)	2013/11/19, 05:49:24	2456615.7412	1200	37	1.61	-31.9 ± 0.9	85.4 ± 2.1
	1670340 (22f)	2013/11/19, 06:10:04	2456615.7556	1200	34	1.76	-31.8 ± 2.0	95.8 ± 4.4
	1733896 (22g)	2014/08/18, 12:09:53	2456888.0116	1200	34	1.71	-42.6 ± 2.2	88.5 ± 2.6
	1740703 (22h)	2014/09/14, 08:52:26	2456914.8734	1200	36	1.26	-47.3 ± 2.8	87.4 ± 2.0
	1755698 (22i)	2014/11/10, 06:54:20	2456971.7871	1200	23	1.83	-40.0 ± 5.7	84.6 ± 2.8
6130500	1649381 (9a)	2013/08/23, 07:07:09	2456527.8013	1200	42	1.10	-18.8 ± 1.0	42.9 ± 1.7
	1649382 (9b)	2013/08/23, 07:27:51	2456527.8157	1200	34	1.09	-19.3 ± 0.8	48.6 ± 0.9
	1649383 (9c)	2013/08/23, 07:48:33	2456527.8301	1200	35	1.08	-17.1 ± 1.4	52.1 ± 1.0
	1650648 (9d)	2013/08/29, 11:02:48	2456533.9648	1200	35	1.51	-18.1 ± 1.3	51.2 ± 1.4
	1654724 (9e)	2013/09/18, 06:31:00	2456553.7751	1200	29	1.08	-19.0 ± 1.3	49.2 ± 1.1
	1733878 (9f)	2014/08/18, 06:23:21	2456887.7710	1200	36	1.20	-16.0 ± 1.1	47.2 ± 2.2
6227118	1653323 (27a)	2013/09/13, 05:31:29	2456548.7343	1200	60	1.13	6.4 ± 3.2	135.9 ± 1.9
	1655648 (27b)	2013/09/22, 07:06:51	2456557.8000	1200	71	1.10	2.1 ± 1.8	133.0 ± 2.3
	1740707 (27c)	2014/09/14, 10:05:51	2456914.9248	1200	54	1.46	7.5 ± 4.4	129.4 ± 2.2
	1755701 (27d)	2014/11/10, 07:48:04	2456971.8248	1200	29	2.18	8.5 ± 2.0	132.5 ± 3.4
6445601	1648978 (2a)	2013/08/21, 11:11:41	2456525.9711	1200	41	1.42	-7.7 ± 1.6	71.3 ± 2.4
	1648979 (2b)	2013/08/21, 11:32:17	2456525.9855	1200	42	1.52	-8.4 ± 3.2	72.6 ± 1.8
	1648980 (2c)	2013/08/21, 11:53:04	2456525.9999	1200	41	1.65	-4.0 ± 0.5	70.1 ± 1.7

Table 1 – *continued*

KIC (1)	Spectrum (2)	UTC date (mid) (3)	BJD (mid) (4)	Exp.(s) (5)	S/N (6)	AM (7)	RV (8)	$v \sin i$ (9)
6520969	1650645 (2d)	2013/08/29, 09:58:49	2456533.9203	1200	39	1.27	-4.8 ± 0.9	70.4 ± 3.2
	1654452 (2e)	2013/09/17, 05:23:57	2456552.7285	1200	44	1.10	-4.2 ± 1.3	72.2 ± 2.1
	1740705 (2f)	2014/09/14, 09:37:09	2456914.9045	1200	38	1.42	-5.7 ± 1.8	70.8 ± 1.7
	1650643 (21a)	2013/08/29, 09:15:49	2456533.8904	1200	49	1.18	-299.8 ± 1.2	$<4.2 \pm 1.6$
	1653553 (21b)	2013/09/14, 06:34:45	2456549.7778	1200	41	1.08	-299.7 ± 0.8	$<6.9 \pm 1.2$
	1740704 (21c)	2014/09/14, 09:14:52	2456914.8890	1200	38	1.35	-299.4 ± 0.5	$<5.4 \pm 1.4$
	1649178 (5a)	2013/08/22, 08:27:28	2456526.8571	1200	36	1.09	8.9 ± 0.3	[11]
	1649179 (5b)	2013/08/22, 08:48:09	2456526.8714	1200	34	1.10	8.4 ± 0.3	[11]
	1649180 (5c)	2013/08/22, 09:08:51	2456526.8858	1200	45	1.12	10.2 ± 0.4	[11]
6780873	1650646 (5d)	2013/08/29, 10:19:56	2456533.9349	1200	39	1.34	-26.81 ± 0.13	11 ± 1
	1654453 (5e)	2013/09/17, 05:45:33	2456552.7435	1200	36	1.09	-24.13 ± 0.15	12 ± 1
	1740695 (5f)	2014/09/14, 06:08:57	2456914.7600	1200	40	1.09	43.08 ± 0.14	11 ± 1
	1741393 (5g)	2014/09/17, 05:56:60	2456917.7515	1200	40	1.09	-22.56 ± 0.14	11 ± 1
	1753085 (5h)	2014/10/31, 05:32:15	2456961.7311	1200	35	1.22	12.99 ± 0.20	15 ± 3
	1755692 (5i)	2014/11/10, 04:31:38	2456971.6881	1200	25	1.17	-3.79 ± 0.18	11 ± 1
	1650474 (16a)	2013/08/28, 05:51:16	2456532.7481	1200	42	1.14	5.7 ± 1.4	101 ± 3
	1650475 (16b)	2013/08/28, 06:11:58	2456532.7625	1200	43	1.12	4.4 ± 3.8	109 ± 3
	1653552 (16c)	2013/09/14, 06:12:57	2456549.7624	1200	44	1.09	0.6 ± 1.0	104 ± 3
7020707	1733891 (16d)	2014/08/18, 10:18:20	2456887.9339	1200	40	1.26	2.5 ± 2.9	106 ± 3
	1649377 (8a)	2013/08/23, 05:57:44	2456527.7524	1200	39	1.13	-17.9 ± 2.3	39 ± 4
	1649378 (8b)	2013/08/23, 06:18:25	2456527.7668	1200	51	1.11	-18.9 ± 2.5	42 ± 3
	1649379 (8c)	2013/08/23, 06:39:06	2456527.7812	1200	39	1.09	-20.6 ± 1.8	43 ± 1
	1650637 (8d)	2013/08/29, 06:48:41	2456533.7876	1200	39	1.09	-22.1 ± 2.4	39 ± 4
	1654454 (8e)	2013/09/17, 06:07:30	2456552.7580	1200	35	1.10	-20.0 ± 2.9	42 ± 3
	1733884 (8f)	2014/08/18, 07:59:33	2456887.8372	1200	39	1.09	-18.2 ± 1.5	38 ± 1
	1740698 (8g)	2014/09/14, 07:15:49	2456914.8056	1200	39	1.15	-20.6 ± 1.6	46 ± 1
	1753086 (8h)	2014/10/31, 05:55:39	2456961.7466	1200	36	1.46	-17.4 ± 1.7	40 ± 1
7301640	1755694 (8i)	2014/11/10, 05:18:57	2456971.7203	1200	25	1.47	-17.2 ± 2.4	40 ± 2
	1649384 (10a)	2013/08/23, 08:10:45	2456527.8456	1200	36	1.09	-10 ± 6	124 ± 4
	1649385 (10b)	2013/08/23, 08:31:27	2456527.8600	1200	37	1.09	-11 ± 5	121 ± 3
	1649386 (10c)	2013/08/23, 08:52:09	2456527.8744	1200	35	1.10	-8 ± 5	128 ± 4
	1653559 (10d)	2013/09/14, 08:46:24	2456549.8695	1200	36	1.21	-10 ± 6	111 ± 7
7621759	1733885 (10e)	2014/08/18, 08:21:40	2456887.8533	1200	35	1.09	-17 ± 4	122 ± 4
	1649181 (6a)	2013/08/22, 09:31:44	2456526.9018	1200	33	1.14	17.8 ± 3.0	77.6 ± 2.0
	1649182 (6b)	2013/08/22, 09:52:26	2456526.9169	1200	35	1.17	17.3 ± 3.5	79.9 ± 2.4
	1649183 (6c)	2013/08/22, 10:13:07	2456526.9305	1200	33	1.21	18.1 ± 4.4	83.2 ± 3.4
	1653558 (6d)	2013/09/14, 08:25:14	2456549.8548	1200	33	1.18	14.5 ± 3.3	75.9 ± 2.2
7765585	1733881 (6e)	2014/08/18, 06:54:30	2456887.7927	1200	35	1.16	17.3 ± 2.4	76.9 ± 1.4
	1653324 (28a)	2013/09/13, 05:53:11	2456548.7492	1200	38	1.11	6.7 ± 2.7	125 ± 6
	1655645 (28b)	2013/09/22, 05:40:49	2456557.7401	1200	45	1.10	6.9 ± 1.6	125 ± 6
	1669659 (28c)	2013/11/16, 05:27:58	2456612.7270	1200	30	1.37	-14.3 ± 2.6	124 ± 13
	1733882 (28d)	2014/08/18, 07:15:60	2456887.8076	1200	34	1.14	-3.1 ± 4.1	123 ± 5
	1740696 (28e)	2014/09/14, 06:31:20	2456914.7757	1200	36	1.09	4.1 ± 4.0	122 ± 3
7819024	1755699 (28f)	2014/11/10, 07:17:38	2456971.8036	1200	20	1.91	-1.5 ± 2.0	121 ± 3
	1650482 (19a)	2013/08/28, 08:42:28	2456532.8672	1200	35	1.14	-57.0 ± 2.1	95.1 ± 5.3
	1650483 (19b)	2013/08/28, 09:03:10	2456532.8815	1200	37	1.17	-66.0 ± 3.5	100.0 ± 2.9
	1650484 (19c)	2013/08/28, 09:23:51	2456532.8959	1200	36	1.20	-62.2 ± 2.2	97.8 ± 1.8
	1654189 (19d)	2013/09/16, 05:53:05	2456551.7487	1200	56	1.10	-63.5 ± 2.1	90.9 ± 1.8
	1733895 (19e)	2014/08/18, 11:47:25	2456887.9959	1200	31	1.60	-58.8 ± 2.9	91.2 ± 4.5
	1740702 (19f)	2014/09/14, 08:28:38	2456914.8568	1200	34	1.23	-55.7 ± 2.9	97.5 ± 2.9
8004558	1753090 (19g)	2014/10/31, 06:56:43	2456961.7896	1200	37	1.60	-48.4 ± 2.4	97.9 ± 2.7
	1755697 (19h)	2014/11/10, 06:29:30	2456971.7699	1200	22	1.68	-62.8 ± 2.0	92.2 ± 2.3
	1648976 (1a)	2013/08/21, 10:28:14	2456525.9403	1200	51	1.47	-260 ± 4	80 ± 5
	1648977 (1b)	2013/08/21, 10:48:56	2456525.9546	1200	42	1.58	-261 ± 4	84 ± 4
8110941	1650636 (1c)	2013/08/29, 06:27:30	2456533.7728	1200	52	1.10	-254 ± 5	82 ± 9
	1733883 (1d)	2014/08/18, 07:38:02	2456887.8222	1200	42	1.10	-254 ± 5	76 ± 5
	1740697 (1e)	2014/09/14, 06:53:45	2456914.7902	1200	43	1.14	-251 ± 4	95 ± 8
	1753087 (1f)	2014/10/31, 06:20:11	2456961.7636	1200	40	1.64	-251 ± 4	92 ± 7
	1755693 (1g)	2014/11/10, 04:55:24	2456971.7039	1200	26	1.40	-242 ± 4	94 ± 7
	1653325 (29a)	2013/09/13, 06:15:24	2456548.7647	1200	44	1.10	4.3 ± 0.2	$<7.8 \pm 0.6$
	1655646 (29b)	2013/09/22, 06:03:09	2456557.7557	1200	48	1.10	4.4 ± 0.4	$<7.2 \pm 0.5$

Table 1 – *continued*

KIC (1)	Spectrum (2)	UTC date (mid) (3)	BJD (mid) (4)	Exp.(s) (5)	S/N (6)	AM (7)	RV (8)	$v \sin i$ (9)
8196006	1669658 (29c)	2013/11/16, 05:05:27	2456612.7114	1200	34	1.29	4.4 ± 0.5	$<7.6 \pm 0.5$
	1741400 (29d)	2014/09/17, 08:34:35	2456917.8611	1200	39	1.22	4.3 ± 0.2	$<7.1 \pm 2.1$
	1653326 (30a)	2013/09/13, 06:37:34	2456548.7803	1200	41	1.10	-4.6 ± 1.6	90.5 ± 1.6
	1655848 (30b)	2013/09/23, 09:54:21	2456558.9164	1200	46	1.54	-2.4 ± 1.9	96.4 ± 2.3
	1670136 (30c)	2013/11/18, 04:51:24	2456614.7017	1200	36	1.23	-2.2 ± 1.8	93.3 ± 2.6
8330910	1741401 (30d)	2014/09/17, 08:57:55	2456917.8776	1200	38	1.24	-6.1 ± 3.0	92.8 ± 2.3
	1648981 (3a)	2013/08/21, 12:15:07	2456526.0154	1200	44	1.59	20 ± 7	220 ± 6
	1648982 (3b)	2013/08/21, 12:35:50	2456526.0298	1200	43	1.73	22 ± 15	222 ± 6
	1654192 (3c)	2013/09/16, 06:58:02	2456551.7944	1200	51	1.10	24 ± 9	231 ± 6
9244992	1741402 (3d)	2014/09/17, 09:20:29	2456917.8933	1200	43	1.29	19 ± 9	224 ± 5
	1649185 (7a)	2013/08/22, 10:45:22	2456526.9530	1200	32	1.27	-15.8 ± 0.4	$<7.4 \pm 0.6$
	1649186 (7b)	2013/08/22, 11:06:03	2456526.9674	1200	33	1.32	-15.9 ± 0.5	$<7.2 \pm 0.4$
	1649187 (7c)	2013/08/22, 11:26:44	2456526.9818	1200	32	1.40	-15.9 ± 0.3	$<5.8 \pm 0.5$
	1654191 (7d)	2013/09/16, 06:36:30	2456551.7794	1200	36	1.11	-16.8 ± 0.6	$<5.8 \pm 0.5$
9267042	1733887 (7e)	2014/08/18, 08:50:09	2456887.8731	1200	34	1.11	-15.4 ± 0.4	$<7.1 \pm 0.5$
	1649575 (12a)	2013/08/24, 08:39:11	2456528.8647	1200	42	1.16	-8 ± 4	109.8 ± 3.4
	1649576 (12b)	2013/08/24, 08:59:53	2456528.8790	1200	37	1.19	-11 ± 5	115.4 ± 9.8
	1649577 (12c)	2013/08/24, 09:20:35	2456528.8934	1200	37	1.23	-9 ± 3	115.2 ± 2.9
	1650639 (12d)	2013/08/29, 07:37:38	2456533.8217	1200	47	1.12	-16 ± 4	120.7 ± 3.0
	1654455 (12e)	2013/09/17, 06:30:10	2456552.7740	1200	37	1.13	-8 ± 3	124.2 ± 4.1
	1733889 (12f)	2014/08/18, 09:34:01	2456887.9029	1200	39	1.21	-14 ± 5	118.9 ± 4.2
	1740699 (12g)	2014/09/14, 07:38:17	2456914.8215	1200	39	1.19	-16 ± 7	120.4 ± 4.4
	1754691 (12h)	2014/11/07, 04:36:12	2456968.6912	1200	22	1.26	-10.5 ± 0.9	94.8 ± 3.9
	1754692 (12i)	2014/11/07, 04:57:36	2456968.7061	1200	21	1.31	-12.2 ± 0.7	97.3 ± 2.1
9535881	1754693 (12j)	2014/11/07, 05:19:03	2456968.7210	1200	19	1.39	-11.3 ± 0.3	103.4 ± 0.9
	1755695 (12k)	2014/11/10, 05:42:19	2456971.7369	1200	24	1.55	-11.8 ± 1.3	113.0 ± 3.9
	1650651 [25a]	2013/08/29, 12:11:48	2456534.0127	1200	41	2.01	7.1 ± 0.7	59.4 ± 1.2
	1654190 [25b]	2013/09/16, 06:15:04	2456551.7642	1200	45	1.12	6.7 ± 0.5	51.7 ± 1.2
	1741398 [25c]	2014/09/17, 07:49:37	2456917.8298	1200	45	1.17	6.9 ± 1.3	53.1 ± 0.7
9966976	1753092 [25d]	2014/10/31, 07:27:07	2456961.8111	1200	27	1.68	2.9 ± 1.4	59.1 ± 1.6
	1653327 (31a)	2013/09/13, 06:59:20	2456548.7952	1200	47	1.12	-2 ± 5	122.6 ± 1.5
	1655845 (31b)	2013/09/23, 08:43:48	2456558.8673	1200	53	1.32	-1 ± 5	125.6 ± 2.4
	1670137 (31c)	2013/11/18, 05:12:58	2456614.7167	1200	38	1.35	-1 ± 6	122.3 ± 2.2
10989032	1741399 (31d)	2014/09/17, 08:12:28	2456917.8458	1200	42	1.19	3 ± 6	123.7 ± 2.2
	1653560 (32a)	2013/09/14, 09:08:06	2456549.8845	1200	34	1.31	-44 ± 2	44.4 ± 1.6
	1655844 (32b)	2013/09/23, 08:21:29	2456558.8517	1200	43	1.28	-43 ± 3	47.4 ± 1.6
	1670135 (32c)	2013/11/18, 04:29:40	2456614.6866	1200	34	1.25	-32 ± 2	47.6 ± 1.9
	1740691 (32d)	2014/09/14, 05:11:51	2456914.7205	1200	36	1.22	-14 ± 2	41.8 ± 0.9
	1740708 (32e)	2014/09/14, 10:28:24	2456914.9403	1200	31	1.63	-8 ± 2	46.0 ± 1.4
	1741390 (32f)	2014/09/17, 05:24:18	2456917.7290	1200	35	1.18	-15 ± 2	45.2 ± 1.4
	1741405 (32g)	2014/09/17, 09:51:03	2456917.9142	1200	33	1.50	-22 ± 2	47.4 ± 1.4
11649497	1755702 (32h)	2014/11/10, 08:10:06	2456971.8404	1200	18	2.50	-37 ± 3	47.9 ± 2.0
	1649572 (11a)	2013/08/24, 07:34:50	2456528.8198	1200	39	1.16	-21.7 ± 0.3	$<5.6 \pm 0.3$
	1649573 (11b)	2013/08/24, 07:55:31	2456528.8342	1200	39	1.17	-21.1 ± 0.3	$<5.9 \pm 0.4$
	1649574 (11c)	2013/08/24, 08:16:13	2456528.8486	1200	42	1.18	-21.4 ± 0.3	$<5.3 \pm 0.6$
	1650638 (11d)	2013/08/29, 07:16:26	2456533.8069	1200	39	1.16	-21.2 ± 0.3	$<4.7 \pm 0.4$
	1654456 (11e)	2013/09/17, 06:52:03	2456552.7891	1200	38	1.19	-21.3 ± 0.3	$<5.8 \pm 0.3$
11754974	1733888 (11f)	2014/08/18, 09:12:12	2456887.8876	1200	40	1.22	-21.9 ± 0.2	$<6.1 \pm 0.3$
	APO (13a)	2012/10/28, 05:53:24	2456228.7455	900	19	2.44	-301 ± 4	27.4 ± 2.2
	APO (13b)	2012/10/28, 06:10:57	2456228.7576	900	22	2.71	-299 ± 4	25.0 ± 2.5
	1649578 (13c)	2013/08/24, 09:43:25	2456528.9093	1200	60	1.31	-300.2 ± 1.0	25.7 ± 2.1
	1649579 (13d)	2013/08/24, 10:04:06	2456528.9236	1200	66	1.37	-306.8 ± 2.0	36.6 ± 1.4
	1650641 (13e)	2013/08/29, 08:21:22	2456533.8521	1200	62	1.20	-313.2 ± 2.2	25.7 ± 2.5
	1733890 (13f)	2014/08/18, 09:55:49	2456887.9180	1200	57	1.28	-302.1 ± 0.8	25.5 ± 1.5
	1740700 (13g)	2014/09/14, 08:00:31	2456914.8370	1200	59	1.26	-301.3 ± 0.9	25.6 ± 1.6
12643589	1755696 (13h)	2014/11/10, 06:05:49	2456971.7536	1200	35	1.66	-302.3 ± 1.7	31.3 ± 1.7
	1650476 [17a]	2013/08/28, 06:33:57	2456532.7776	1200	48	1.19	-61.3 ± 0.3	29.2 ± 0.5
	1650477 [17b]	2013/08/28, 06:54:38	2456532.7920	1200	38	1.18	-61.6 ± 0.5	28.8 ± 0.4
	1650478 [17c]	2013/08/28, 07:15:20	2456532.8063	1200	38	1.18	-61.7 ± 0.4	28.5 ± 0.5
	1654187 [17d]	2013/09/16, 05:10:20	2456551.7188	1200	37	1.20	-61.2 ± 0.4	28.5 ± 0.5
	1733892 [17e]	2014/08/18, 10:40:16	2456887.9489	1200	35	1.41	-59.5 ± 0.7	28.5 ± 0.7

Table 1 – *continued*

KIC/HD (1)	Spectrum (2)	UTC date (mid) (3)	BJD (mid) (4)	Exp.(s) (5)	S/N (6)	AM (7)	RV (8)	$v \sin i$ (9)
12688835	1650479 (18a)	2013/08/28, 07:38:01	2456532.8221	1200	35	1.18	-26 ± 10	217 ± 15
	1650480 (18b)	2013/08/28, 07:58:43	2456532.8365	1200	35	1.19	-20 ± 10	239 ± 15
	1650481 (18c)	2013/08/28, 08:19:25	2456532.8508	1200	35	1.21	-28 ± 12	238 ± 15
	1654188 (18d)	2013/09/16, 05:31:20	2456551.7334	1200	37	1.19	-25 ± 10	234 ± 15
	1733893 (18e)	2014/08/18, 11:02:28	2456887.9643	1200	31	1.48	-51 ± 10	221 ± 5
(b) IAU radial velocity standard stars								
HD 144579	1733875 (a)	2014/08/18, 05:26:16	2456887.2267	30	182	1.08	-59.17 ± 0.41	3.65 ± 0.13
	1733879 (b)	2014/08/18, 06:36:44	2456887.2757	30	165	1.17	-58.98 ± 0.41	3.66 ± 0.11
	1740690 (c)	2014/09/14, 04:56:45	2456914.2062	30	186	1.19	-58.97 ± 0.41	3.66 ± 0.34
	1741391 (d)	2014/09/17, 05:38:18	2456917.2351	30	177	1.35	-59.05 ± 0.42	3.76 ± 0.24
HD 154417	1733874 (a)	2014/08/18, 05:19:15	2456887.2218	30	213	1.06	-16.61 ± 0.13	5.14 ± 0.17
	1733880 (b)	2014/08/18, 06:39:14	2456887.2775	30	217	1.09	-16.50 ± 0.13	4.85 ± 0.14
	1740692 (c)	2014/09/14, 05:27:38	2456914.2277	30	230	1.15	-16.69 ± 0.13	4.33 ± 0.16
	1741392 (d)	2014/09/17, 05:42:09	2456917.2378	30	224	1.22	-16.44 ± 0.18	4.37 ± 0.14
HD 171391	1733886 (a)	2014/08/18, 08:36:14	2456887.3586	30	349	1.26	7.69 ± 0.20	3.67 ± 0.28
	1740693 (b)	2014/09/14, 05:31:31	2456914.2304	30	391	1.16	7.75 ± 0.19	3.63 ± 0.19
	1741389 (c)	2014/09/17, 05:09:09	2456917.2148	30	384	1.16	7.72 ± 0.19	3.97 ± 0.38
	1753083 (d)	2014/10/31, 04:54:05	2456961.2044	30	380	1.52	7.78 ± 0.19	3.58 ± 0.16
	1754690 (e)	2014/11/07, 04:19:19	2456968.1803	30	111	1.48	7.96 ± 0.19	4.04 ± 0.50
HD 182572	1740701 (a)	2014/09/14, 08:14:35	2456914.3436	30	282	1.15	-100.13 ± 0.34	2.96 ± 0.12
	1741403 (b)	2014/09/17, 09:34:00	2456917.3988	30	349	1.59	-100.07 ± 0.33	2.81 ± 0.15
	1753088 (c)	2014/10/31, 06:36:40	2456961.2756	30	327	1.56	-99.66 ± 0.32	2.87 ± 0.12
	1755691 (d)	2014/11/10, 04:16:12	2456971.1781	30	180	1.12	-99.53 ± 0.33	2.95 ± 0.12
HD 187691	1740706 (a)	2014/09/14, 09:51:18	2456914.4108	30	288	1.46	0.22 ± 0.12	3.45 ± 0.14
	1741404 (b)	2014/09/17, 09:36:41	2456917.4006	30	324	1.44	0.22 ± 0.12	4.03 ± 0.15
	1753091 (c)	2014/10/31, 07:11:56	2456961.3001	30	323	1.65	0.21 ± 0.12	3.94 ± 0.14
	1754694 (d)	2014/11/07, 05:33:51	2456968.2320	30	143	1.24	0.36 ± 0.12	2.76 ± 0.14
	1754695 (e)	2014/11/07, 05:35:02	2456968.2328	30	126	1.24	0.34 ± 0.12	3.47 ± 0.17
	1754696 (f)	2014/11/07, 05:36:12	2456968.2337	30	143	1.25	0.38 ± 0.12	3.31 ± 0.19
	1755700 (g)	2014/11/10, 07:32:58	2456971.3147	30	129	2.55	0.37 ± 0.12	4.08 ± 0.18

purposes, including three RV standard stars selected again from the Udry et al. list. The resolution of the APO spectra, $R \sim 31\,500$ (or 2.5 pixels), is lower than that for the CFHT spectra, and the wavelength coverage was from 320 to 1000 nm, dispersed over 107 orders. The default slit (size 1.6 arcsec \times 3.2 arcsec) was used for all the observations, and the readout noise typically was less than $7 \text{ e}^- \text{ pixel}^{-1}$ with a gain of $3.8 \text{ e}^- \text{ ADU}^{-1}$. All the spectra were preprocessed with `IRAF`. Because of their lower resolution and lower signal-to-noise ratios (S/N), the APO spectra were used mainly for additional RV and rotation velocity information. Details of the APO observations of the *Kepler*-field SX Phe stars also are given in Table 1.

While acquiring the APO spectra, KIC 1162150 (*15) and KIC 6227118 (*27) were seen in the 3.5-m telescope finder fields to be optical doubles with very close, relatively bright neighbours. Finding charts made from the DSS digital sky survey are shown in Fig. 2 for these and two other stars. KIC 1162150 is seen to be located among a clump of relatively bright stars and the image of KIC 6227118 is quite asymmetric. It is possible that photometric observations (and possibly our spectroscopy) for these two stars are contaminated by light from the neighbour stars.

2.1 Radial velocities

Barycentric RVs were measured for each spectrum using the cross-correlation methods implemented in the routines ‘fxcor’ and ‘xcsao’ in `IRAF` (Tonry & Davis 1979; Kurtz & Mink 1998) and the ‘RCROS’ program of Díaz et al. (2011) and by fitting synthetic spectra. Since only minor differences were found using the different methods,

we chose to adopt the ‘fxcor’ values, where the cross-correlation function (CCF) was based on appropriate template synthetic spectra. The resultant RVs for the individual spectra are presented in Table 1 and mean RVs are given in Table 2.

The RV zero-points were checked using the IAU standard star observations. When the mean RVs for the five standards observed with ESPaDOnS were compared with those given by Udry et al. (1999), the mean difference (ours minus the Udry et al. value) was $0.38 \pm 0.06 \text{ km s}^{-1}$. This mean is comparable with the $\pm 0.3 \text{ km s}^{-1}$ uncertainty in the Udry et al. RV values. Our velocities also show good agreement with those from other studies: for HD 171391, Massarotti et al. (2008) found $\text{RV} = 7.59 \pm 0.05 \text{ km s}^{-1}$, compared with our mean value (five spectra) of $7.78 \pm 0.05 \text{ km s}^{-1}$; and for HD 182572, Nidever et al. (2002) measured $\text{RV} = -100.29 \text{ km s}^{-1}$, compared with our $-99.84 \pm 0.15 \text{ km s}^{-1}$ (four spectra). Comparisons for the three IAU RV standard stars observed at APO likewise showed excellent agreement between our RVs and the standard values: mean difference between our estimates and the Udry et al. values amounted to $-0.4 \pm 0.4 \text{ km s}^{-1}$.

2.1.1 Stars with high RV

Three of the stars have large negative RVs: KIC 6520969 (*21) with $\text{RV} = -299.5 \pm 0.1 \text{ km s}^{-1}$; KIC 8004558 (*1) with $\text{RV} = -254.1 \pm 1.5 \text{ km s}^{-1}$; and KIC 11754974 (*13) with $\text{RV} = -307 \pm 4 \text{ km s}^{-1}$. Two of the stars (KIC 8004558 and 11754974) were already of interest because of their resemblance to field SX Phe stars (see table 3 of BN12). Since all three stars have retrograde motions and low metallicities (Figs 6 and 13), there is little doubt that they

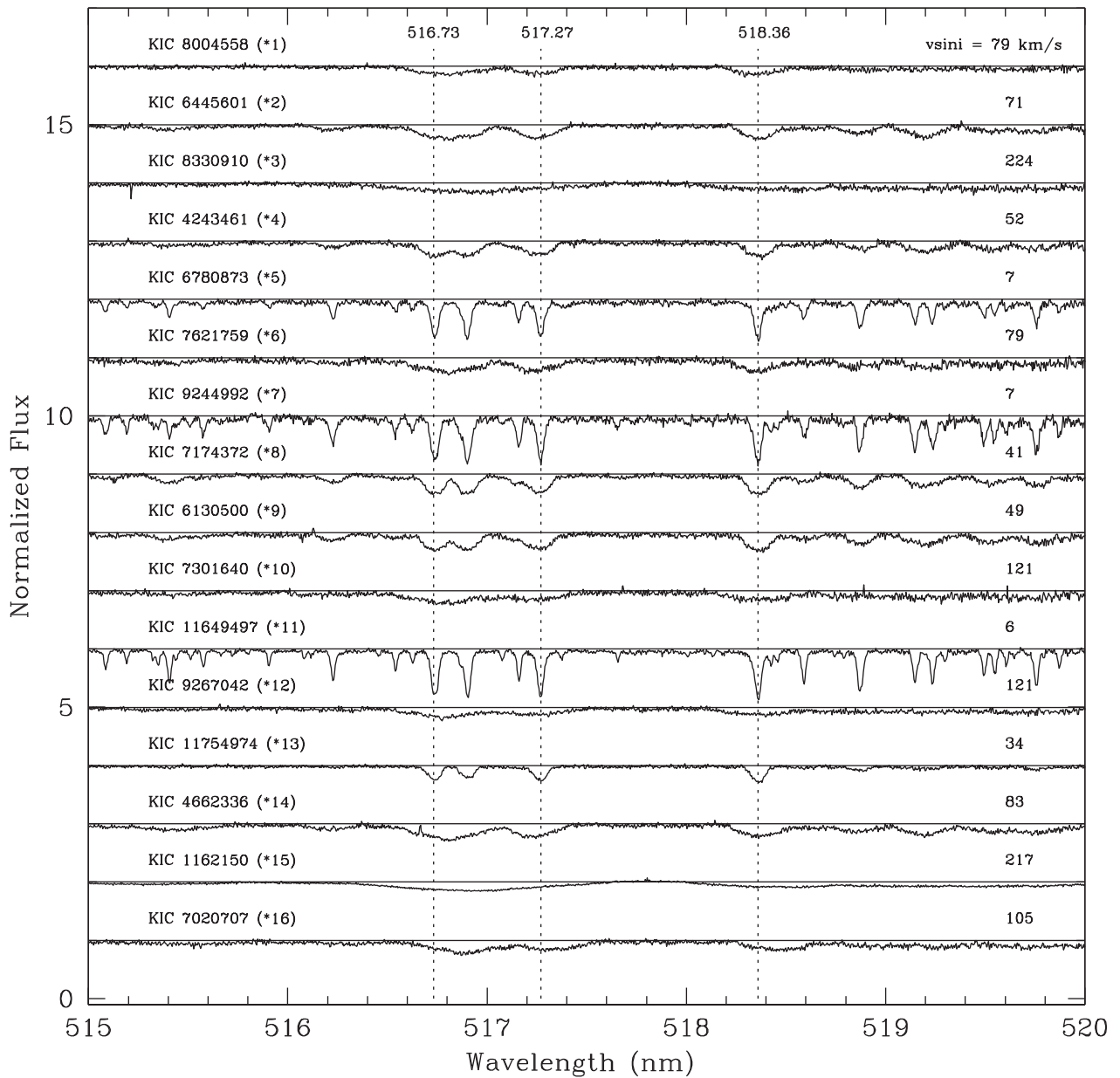


Figure 1. ESPaDOnS (CFHT) spectra for the wavelength region 515–520 nm, illustrating the wide range of line broadenings. Each spectrum is identified by the KIC number (and, in parentheses, the CFHT star number). The dashed vertical lines identify the Mg triplet lines and on the right-hand side of the diagram, the average $v \sin i$ (km s^{-1}) values are given. The ordering is by CFHT star number.

are *bona fide* SX Phe stars. Their metal abundances are comparable to those of the SX Phe BSs found in metal-rich globular clusters, for example, 47 Tuc (Gilliland et al. 1998; Bruntt et al. 2001) and M71 (Hodder et al. 1992; McCormac et al. 2014). The 47 Tuc stars observed with *Hubble Space Telescope* (*HST*) also resemble the *Kepler* stars in exhibiting multiperiodic variations and of having similarly low amplitudes ($\sim 5\text{--}50$ mmag).

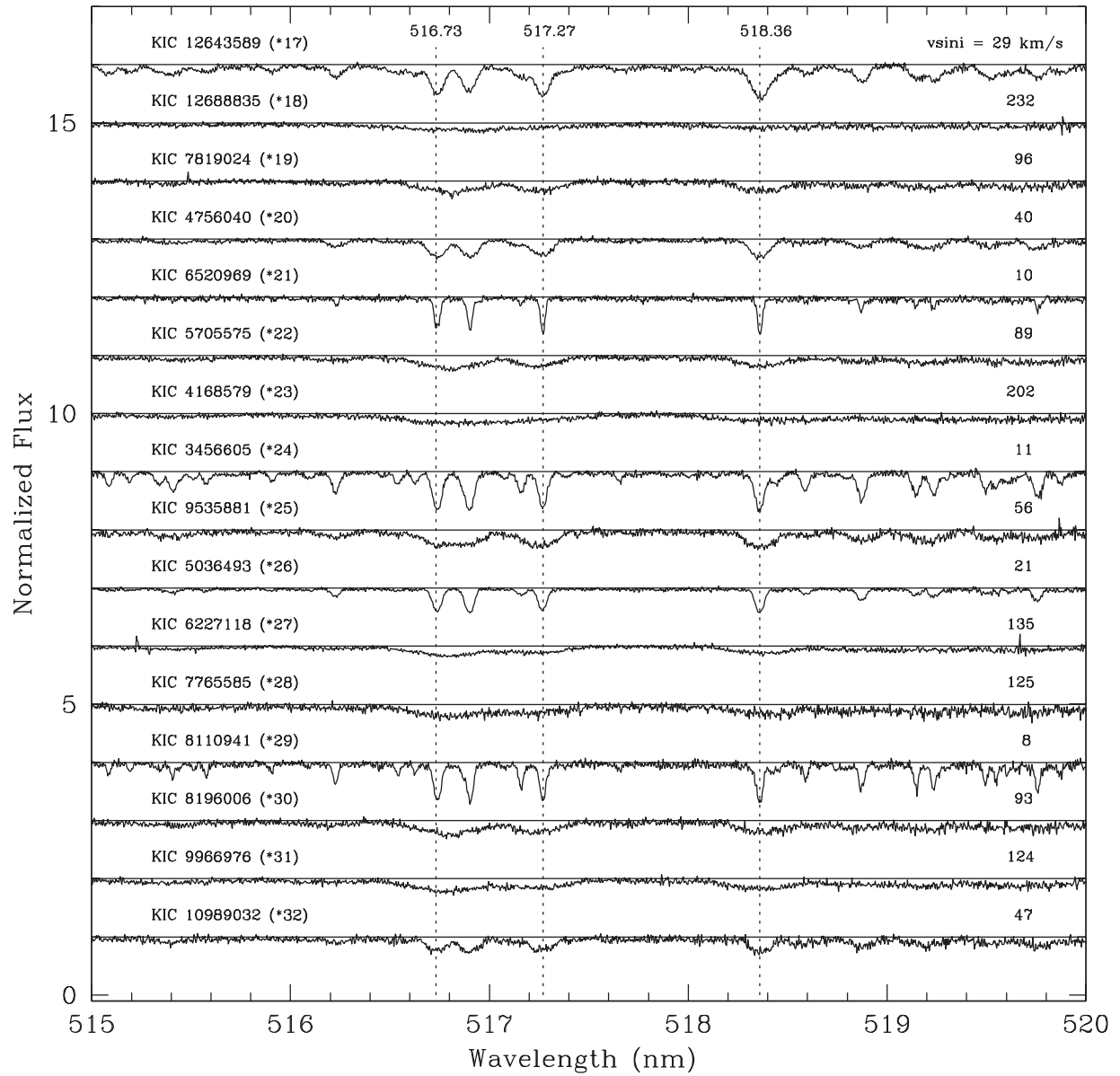
KIC 11754974 is known to reside in a 343 d binary system (Murphy et al. 2013b) and based on an analysis of the complete set of *Kepler* Q0–Q17 photometry, we show below that KIC 8004558 also is a photometric time-delay (TD) binary (orbital period ~ 262 d). In both cases, the variable star is thought to be the more massive primary ($M \sim 1.5 M_{\odot}$) and the secondary has a mass $\sim 0.5 M_{\odot}$. No photometric or spectroscopic evidence could be found to suggest that KIC 6520969 (*21) is a binary system.

2.1.2 RV variations

There are several reasons why one might expect some of the programme stars to show RV variations: (1) all of the stars exhibit light variations due to radial and non-radial pulsations (usually multiperiodic); (2) at least 10 of the pulsators are in binary systems (see Section 3.3 below); and (3) the two misclassified stars, KIC 9535881 and KIC 12643589, are known to be close eclipsing binaries.¹

Since the spectroscopic part of this study was intended only as a first-look survey, the sampling design is far from optimal for analysing temporal variations in the spectra and only a relatively

¹ Squared parentheses around the CFHT star numbers for KIC 9535881 [*25] and KIC 12643589 [*17] have been used throughout this paper to distinguish these two stars from the 32 *bona fide* candidate SX Phe pulsators.

Figure 1 – *continued*

small number of spectra were taken for each star (typically 5 and at most 11). Moreover, owing to the wide range of line widths of the sample stars, the uncertainties of the individual RV measurements range from $\sim \pm 10 \text{ km s}^{-1}$ for the four rapidly rotating stars to only a few tenths of a km s^{-1} for the narrow-lined metal-rich (and standard) stars that have high S/N spectra. Furthermore, the spacing of the observations is not ideal for identifying RV variations, in particular: (1) the ~ 300 d gaps between the 2012, 2013 and 2014 observations are a potential cause of aliasing difficulties; (2) many of the stars were observed only once in 2014; and (3) the spacing may be inappropriate for detecting certain orbital and pulsation periods (i.e. cycle-count and Nyquist aliasing). Finally, the IAU RV standards observed at CFHT were observed only in 2014 and thus year-to-year offsets in the RVs are possible (although this seems unlikely given the constancy of the RVs for several programme stars).

Despite these potential problems, time series graphs show some evidence of RV variability for approximately half of the 30 candidate

stars with spectra. Stars were ranked by RV range, where $\Delta \text{RV} = \text{RV}(\text{max}) - \text{RV}(\text{min})$. In the absence of variability and assuming a normal distribution of RVs, $\Delta \text{RV}/\sqrt{n} \sim \sigma_{\text{RV}}$, where σ_{RV} is the standard deviation of the RVs and n is the number of measured RVs for a given star. For the non-variable standard stars, a typical value for $\Delta \text{RV}/\sqrt{n}$ is ~ 0.1 , which is comparable to the uncertainties given in Table 1.

KIC 6780873 (*5) has narrow spectral lines and the largest RV range, $\Delta \text{RV} = 69.9 \pm 0.3 \text{ km s}^{-1}$. Fig. 3 shows that five of its nine spectra exhibit line doubling, identified by two distinct peaks in the CCF; thus, it is clearly a double-lined spectroscopic binary (SB2). In Table 1, only the RVs for the primary star (assumed to be the SX Phe star) are given; these were calculated using the stronger and wider of the two CCF peaks (i.e. the peak with the larger area and larger height above the baseline). The observed RVs of the SX Phe star vary from $-26.81 \pm 0.13 \text{ km s}^{-1}$ to $+43.08 \pm 0.14 \text{ km s}^{-1}$. The RVs for both components, noted in Fig. 3 and plotted in Fig. 4, are consistent with KIC 6780873 being a close binary with a

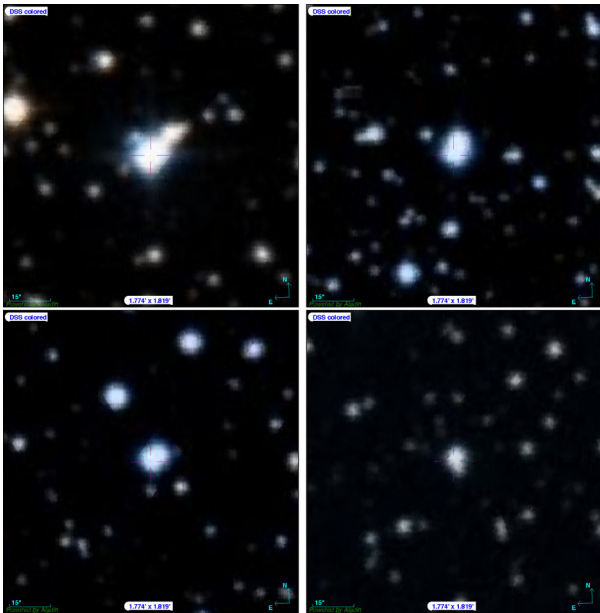


Figure 2. Finding charts for four stars that appear non-circular due to close neighbours: KIC 1162150 (*15, upper left), KIC 5036493 (*26, upper right), KIC 6227118 (*27, lower left) and KIC 7621759 (*6, lower right). All are colour DSS images from the Aladin Sky Atlas, 1.774 arcmin \times 1.819 arcmin across, with north to the top and east to the left. For KIC 5036493, the brighter bluer star to the south is the SX Phe candidate.

9.161 ± 0.001 d orbital period (see Section 3.3). The widths of the CCFs suggest that $v \sin i$ for the primary is larger than that of the secondary, 11 ± 2 km s $^{-1}$ versus 5 ± 2 km s $^{-1}$. The observation of spectral lines due to the secondary suggests that the less luminous companion star is a low-mass main-sequence star and not a giant or white dwarf.

The other SX Phe candidates with large ΔRV values are: KIC 12688835 (*18), 10989032 (*32), 7765585 (*28), 7819024 (*19), 8004558 (*1), 5705575 (*22), 11754974 (*13) and 9267042 (*12). All except KIC 12688835 and KIC 7765585 are binary systems (see Section 3.3). The large ΔRV of KIC 12688835 (*18) is based on four 2013 spectra with $RV \sim -25$ km s $^{-1}$ and a single 2014 spectrum with $RV = -51 \pm 10$ km s $^{-1}$; owing to the large uncertainties that result from broad spectral lines, this evidence for its RV variability must be considered tentative. Likewise, the evidence for the RV variation of KIC 7765585 (*28) hinges primarily on one of the RVs being significantly different from the rest. The measured $\Delta RV = 14 \pm 6$ km s $^{-1}$ for KIC 11754974 (*13), the 344-d non-eclipsing binary studied by Murphy et al. (2013b), is consistent with the photometric K_1 value of 8.2 ± 0.2 km s $^{-1}$ (see Section 3.3); the significant RV differences seen for the three 2013 August spectra, if real, hint at additional variability.

Two other TD binaries exhibit small RV ranges consistent with their photometrically predicted small K_1 values (see Table 9): KIC 4243461 (*4) was found to have $\Delta RV = 5.1 \pm 2.0$ km s $^{-1}$, which is to be compared with the predicted $K_1 = 5.3 \pm 0.2$ km s $^{-1}$; and KIC 9966976 (*31) has $\Delta RV = 5 \pm 5$ km s $^{-1}$ (the large uncertainty being due to its large $v \sin i$) compared with the predicted $K_1 = 0.64 \pm 0.04$ km s $^{-1}$. A third TD binary, KIC 7300184, which was not observed spectroscopically, is also predicted (based on $K_1 = 0.02 \pm 0.02$ km s $^{-1}$) to have a small RV range.

Finally, several of the above-mentioned stars show broadened CCFs and structure that is (or may be) due to RV variation in a binary

system (see Section 3.3), but might also be caused by rotation, large amounts of macrotubulence, noise, etc. The CCFs for four such stars are shown in Fig. 5. As noted earlier, KIC 8004558 (*1) is a high-velocity 262-d binary system; if the CCFs for its eight spectra are fitted with a Gaussian, the RVs appear to shift from -260 ± 4 to -242 ± 4 km s $^{-1}$, consistent with binary motion. KIC 10989032 (*32) exhibits the second largest ΔRV (37.5 ± 1.2 km s $^{-1}$) and the *Kepler* Q0–Q17 light curve shows it to be a close semidetached binary system with an orbital period of 2.3 d. If it is a single-line spectroscopic binary and its broadening is due to stellar rotation, then $v \sin i \sim 45 \pm 2$ km s $^{-1}$ (see Section 2.3). The star is listed in the Villanova Eclipsing Binary (EB) catalogue² where its P_{orb} is given as 2.305 097 d. The RV curve derived from the eight available spectra appears to be sinusoidal and thus suggests that the orbits have been circularized (see Section 3 below).

Higher SNR spectroscopic observations and more sophisticated analysis methods (such as the ‘broadening functions’ advocated by Rucinski 1999) might help to better assess the RV variations of the programme stars.

2.2 Distances and space motions

Membership in the galactic halo stellar population is one of the defining features of an SX Phe star. Height above the Galactic plane and space motions are often used to discriminate between Pop. II and Pop. I stars, where stars with vertical height greater than ~ 500 pc and total speed greater than ~ 200 km s $^{-1}$ almost certainly are Pop. II stars.

Galactic coords (l, b), $E(B-V)$ reddenings, distances, d (pc), and vertical heights above the Galactic plane, z (pc), for the programme stars are given in Table 2. The KIC distances are derived from the Sloan photometry that gives estimates of T_{eff} and $\log g$. The radii in the KIC follow from the gravities and model masses and the T_{eff} and radius information gives the luminosity, L . From L and the observed apparent magnitude, Brown et al. (2011) calculate the distance, from which the $E(B-V)$ reddening and the A_v extinctions are estimated using the simple exponential fall-off model given by their equations 8–13 (see BN12). The only programme star for which the KIC does not give $E(B-V)$ and consequently, distance information, is KIC 11754974, the star studied by Murphy et al. (2013b).

Brown et al. (2011) warned that where there is a clumpy distribution of interstellar matter, ‘the result is systematic misclassification’ in the KIC due to ‘a scattered and confused relation between T_{eff} and colour and other failings’. For this reason, new distance and reddening estimates were derived. These were made using the online ‘cumulative reddening versus distance’ tool created for the ‘3D Dust Mapping’ project (see Green et al. 2014, 2015) available at <http://argonaut.skymaps.info/query>. This tool requires as input a direction indicator (l, b or RA, Dec.) and the distance modulus, $\mu_V (=m_V - M_V)$, and calculates $E(B-V)$ and d (pc), where the interstellar extinction is based on dust maps (see Schlegel et al. 1998; Schlafly & Finkbeiner 2011) rather than an exponential model.

For each star, μ_v was derived using the apparent visual magnitude m_v given in column 4 of Table 5 and by estimating the absolute visual magnitude, M_V , by assuming for the mass the value $1.5 M_\odot$ (i.e. estimated mean for SX Phe stars) and by substituting the spectroscopic estimates of $\log g$ and T_{eff} (given in Table 4, columns 4

² The Villanova EB catalogue (Prša et al. 2011; Slawson et al. 2011; Matijević et al. 2012) is available online at <http://keplerebs.villanova.edu>.

Table 2. Locations and kinematics for the 34 SX Phe candidates. The columns contain: (1 and 2) KIC and CFHT star numbers; (3) galactic latitude and longitude ($^{\circ}$); (4 and 5) $E(B-V)$ reddening (mag) and distance d (pc), from the KIC and based on dust maps; (6) height above the Galactic plane z (pc), KIC values and assuming the new distances; (7) mean RV \pm standard error (with number of measured spectra given in parentheses) – for binary systems, the systemic RVs are given and underlined; (8) space motions, U, V, W and total speed, T , all relative to the LSR.

KIC no. (1)	CFHT no. (2)	Galactic coords. l (J2000) b (3)	$E(B-V)$ KIC, new (4)	d (pc) KIC, new (5)	z (pc) KIC, new (6)	$\langle \text{RV} \rangle$ (km s $^{-1}$) (7)	(U, V, W, T) (km s $^{-1}$) (8)
1162150	15	69.5124, 9.7968	0.160, 0.07	729, 1060	124, 180	-14.8 ± 0.9 (6)	99, -5, 234, 254
3456605	24	72.2362, 8.1478	0.203, 0.14	956, 1690	135, 240	-7.4 ± 0.6 (3)	-335, -70, -186, 389
4168579	23	72.6974, 8.8075	0.257, 0.17	1644, 3620	252, 550	22.9 ± 1.7 (6)	-345, 70, -841, 912
4243461	4	69.8106, 14.9474	0.153, 0.11	983, 1580	254, 410	57.2 ± 1.8 (8)	-331, -169, 456, 588
4662336	14	73.0933, 9.2758	0.204, 0.12	1059, 1760	171, 280	-11.3 ± 0.4 (4)	-455, -93, -233, 520
4756040	20	73.2980, 8.9596	0.206, 0.11	1048, 1780	163, 280	5.9 ± 1.4 (4)	-149, 35, -343, 376
5036493	26	74.8907, 6.7575	0.223, 0.27	996, 1890	117, 220	-4.9 ± 0.7 (4)	-355, -62, -187, 406
5390069	–	75.5152, 6.5051	0.174, 0.19	693, 4200	78, 480	–	–
5705575	22	73.4695, 11.2094	0.209, 0.09	1412, 2220	275, 430	-38.1 ± 1.0 (9)	-364, 125, -1214, 1274
6130500	9	74.6166, 9.9930	0.212, 0.12	1235, 2170	214, 380	-18.3 ± 0.5 (6)	147, 145, -586, 622
6227118	27	76.0714, 7.6323	0.364, 0.12	4172, 850	539, 110	5.3 ± 1.7 (4)	-68, 22, -125, 144
6445601	2	74.5439, 10.9821	0.185, 0.08	1026, 2260	195, 430	-4.5 ± 0.5 (6)	-416, -191, 439, 634
6520969	21	74.1754, 11.9396	0.212, 0.08	1718, 2850	355, 590	-299.5 ± 0.1 (3)	112, -395, 571, 703
6780873	5	74.9284, 11.0447	0.153, 0.06	729, 2090	140, 400	10.1 ± 0.3 (9)	-603, -128, -27, 617
7020707	16	73.5340, 14.8428	0.166, 0.04	1236, 1970	317, 510	2.4 ± 1.3 (4)	-297, -122, 196, 376
7174372	8	71.9764, 18.9932	0.136, 0.05	1135, 2970	369, 970	-19.2 ± 0.6 (9)	-1120, -404, 102, 1195
7300184	–	76.8302, 8.7823	0.181, 0.27	832, 4240	127, 650	–	–
7301640	10	77.0021, 8.5969	0.212, 0.26	1068, 2110	160, 320	-12.0 ± 1.8 (5)	95, 93, -431, 451
7621759	6	76.8876, 9.5983	0.207, 0.19	1120, 2550	187, 430	17.0 ± 0.6 (5)	543, 128, 189, 588
7765585	28	77.0330, 9.6755	0.115, 0.18	455, 1820	76, 310	1.1 ± 3.3 (6)	707, 158, 128, 736
7819024	19	75.4361, 13.1002	0.184, 0.05	1310, 1950	297, 440	-63.7 ± 4.4 (8)	-298, -61, -259, 399
8004558	1	72.7607, 20.3549	0.135, 0.05	1519, 1430	528, 500	-254.1 ± 1.5 (7)	-198, -290, -92, 363
8110941	29	77.6587, 9.6836	0.184, 0.15	910, 1760	153, 300	4.4 ± 0.3 (4)	-52, -62, 414, 422
8196006	30	79.3018, 7.0045	0.198, 0.32	850, 1820	104, 220	-3.5 ± 0.8 (4)	-133, 26, -311, 339
8330910	3	79.6884, 6.8192	0.228, 0.31	1036, 1770	123, 210	20.9 ± 1.1 (4)	572, 142, -9, 590
9244992	7	80.6380, 7.8965	0.288, 0.22	1858, 1470	255, 200	-15.9 ± 0.2 (5)	-37, 40, -334, 338
9267042	12	75.8193, 17.8478	0.156, 0.05	2170, 1580	665, 480	-11.5 ± 1.0 (11)	506, -124, 774, 933
9535881	[25]	79.4210, 11.1577	0.168, 0.07	864, 1940	167, 380	5.0 ± 0.1 (4)	247, 55, 71, 263
9966976	31	80.7107, 10.1734	0.221, 0.09	1396, 1400	247, 250	-0.1 ± 1.1 (4)	362, 62, 68, 374
10989032	32	82.0254, 11.1154	0.230, 0.10	1931, 2710	372, 520	-25.0 ± 0.3 (8)	-997, -236, 436, 1113
11649497	11	79.6609, 19.5242	0.138, 0.04	1374, 1950	459, 650	-21.5 ± 0.2 (6)	-246, 48, -273, 371
11754974	13	80.5370, 17.8823	–, 0.04	–, 1250	–, 380	-307 ± 4 (8)	-379, -393, 76, 552
12643589	[17]	82.5739, 17.7885	0.111, 0.05	592, 1200	181, 370	-60.9 ± 0.1 (5)	568, 144, -365, 691
12688835	18	82.7967, 17.5845	0.159, 0.03	2445, 1890	739, 570	-31.2 ± 7.6 (5)	318, 14, 34, 321

and 6) into the following equations:

$$\log(R/R_{\odot}) = 0.5 [\log M/M_{\odot} - \log(g/g_{\odot})],$$

$$\log(L/L_{\odot}) = 2 \log(R/R_{\odot}) + 4 \log(T_{\text{eff}}/T_{\text{eff}, \odot}),$$

$$M_V = 4.79 - 2.5 \log(L/L_{\odot}).$$

For the Sun, we adopted $T_{\text{eff}, \odot} = 5772$ K and $\log g_{\odot} = 4.438$, and for the programme stars, the bolometric corrections, which are small, were ignored. The derived reddenings, distances and vertical heights are given next to the KIC values in Table 2.

The new reddenings are smaller than the KIC values for all but six of the stars, and in general, the distances are greater.³ The average reddening is 0.12 mag, the average distance is 2.1 kpc and the average height above the Galactic plane is 400 pc. The new

³ Increasing (decreasing) the assumed mass by 0.25 M_{\odot} has little impact on μ_v and $d(\text{pc})$: the μ_v is larger (smaller) by ~ 0.17 mag and the distance is larger (smaller) by ~ 150 pc; the effect of such a change on $E(B-V)$ depends on the distance and gradient in the $E(B-V)$ versus μ_v graph, but is usually small.

reddenings and distances improve upon the KIC values in two ways: (1) T_{eff} and $\log g$ are now based on measurements of high-dispersion spectra, whereas the KIC estimates are based on photometry and have been shown, at least for cooler stars, to be systematically too low by over 200 K (Pinsonneault et al. 2012; see below); and (2) the patchy distribution of the interstellar gas and dust, which is evident in the appearance of multiple discrete interstellar lines in several of the CFHT spectra⁴ is now taken into account.

⁴ The distinction between stellar and interstellar Na I D lines is clear for almost all the stars. This is especially true for the three stars with large RVs where the interstellar Na I D lines are shifted ~ 0.5 nm to the right of the stellar lines. For several of the stars, two or three individual sets of interstellar lines are seen, each presumably arising from a separate interstellar cloud. For several of the stars, the interstellar Na I lines are saturated, an extreme example being KIC 9244992 (*) that has one of the largest E_{B-V} reddenings. A large range in line strengths was observed for the interstellar neutral potassium (K I) line at 769.8 nm. Surprisingly, KIC 3456605 with $E_{B-V} = 0.14$ has a particularly strong and broad interstellar K I line. Detailed quantitative analysis of the interstellar lines, such as that performed by Poznanski, Prochaska & Bloom (2012), might be useful for investigating these and other spectral features but is beyond the scope of this paper.

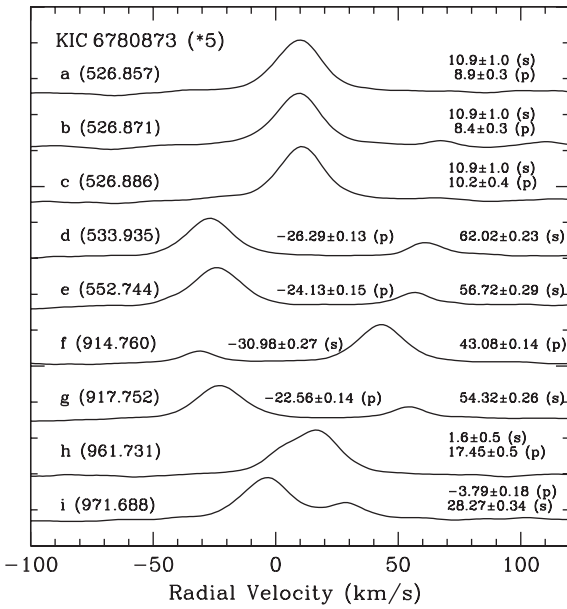


Figure 3. CCFs for the nine spectra of KIC 6780873, a 9.3-d close binary system shown here to be double-lined. Each CCF has been labelled with a letter (a–i) identifying the measured spectrum, and the time of the observations (BJD minus 2456000). Using the peak strengths, each CCF ‘bump’ has been identified as being due to either the primary (p) or secondary (s) star. Also given (right side) are the RVs (km s^{-1}) for each component.

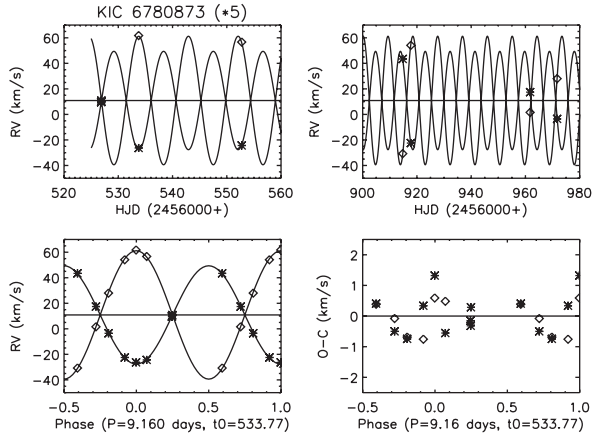


Figure 4. The top two panels show the individual RVs for KIC 6780873 (*5), the 2013 data on the left and the 2014 data on the right, overplotted with model curves assuming eccentricity $e = 0$, orbital period $P_{\text{orb}} = 9.16$ d, HJD time of maximum RV for the secondary = 2456533.77, RV semi-amplitudes for the primary and secondary $K_1 = 38.5 \text{ km s}^{-1}$ and $K_2 = 50.3 \text{ km s}^{-1}$, and systemic RV $\gamma = 10.885 \text{ km s}^{-1}$. The bottom-left panel shows the observed RVs (asterisks for the primary and open diamonds for the secondary) and the corresponding primary and secondary phased RV curves. The bottom-right panel shows the O–C residuals, where the averages for the primary and secondary are 0.009 km s^{-1} and -0.011 km s^{-1} , respectively, and corresponding standard deviations of the residuals about the means, 0.65 and 0.60 km s^{-1} .

Galactic U , V , W space velocities were estimated by combining the mean RVs given in Table 2 (column 7), the new distances (column 5), and the proper motion information summarized in BN12. The velocities are with respect to the Local Standard of Rest (LSR), assuming for the solar motion the values $(U, V, W)_{\odot} = (-8.5 \pm$

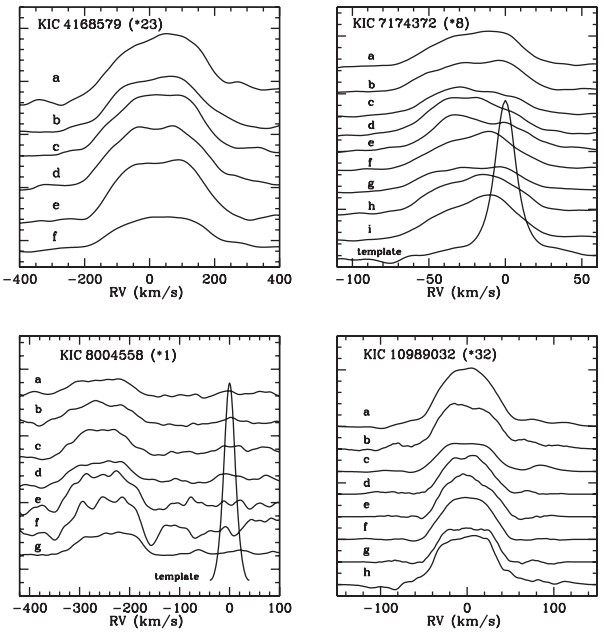


Figure 5. CCFs for four of the BN12 stars, where the ‘letter’ labels on the left identify the individual spectra (see Table 1). For KIC 10989032 (*32, KOI 7397), which is a close binary system with an orbital period of 2.3 d, the CCFs have been Doppler shifted so that the mean RV is zero. KIC 7174372 (*8) and KIC 8004558 (*1) also are probable binary systems (see Section 3.3). Also shown for KIC 7174372 and KIC 8004558 are the much narrower autocorrelation CCFs for the template synthetic spectra.

$0.29, 13.38 \pm 0.43, 6.49 \pm 0.26 \text{ km s}^{-1}$ (Coşkunoğlu et al. 2011). The calculations were made using the general method given by Johnson & Soderblom (1987), as implemented in the IDL ‘Astrolib’ routine ‘gal_uvw’, which assumes U positive in the anticentre direction, V positive in the direction of galactic rotation and W positive in the direction of the north Galactic pole (i.e. left-handed Galactic system). Also calculated were total space motions, T , equal to $(U^2 + V^2 + W^2)^{1/2}$. The resulting velocities are given in column 8 of Table 2.

The ‘Toomre diagram’ is a graphical summary of U , V , W space motions, which is useful for discriminating halo, thick-disc and thin-disc stars (Sandage & Fouts 1987; Venn et al. 2004). Of course, population discrimination based solely on kinematic information is subject to error because the underlying velocity distributions for the different stellar populations overlap by various amounts (Nemec & Linnell Nemec 1991, 1993), a problem that is compounded when the complexity of the distributions is increased by possible galaxy mergers and local streaming events (see, for example, Bensby et al. 2007; Carollo et al. 2007, 2010). The Toomre diagram also ignores chemical composition and age differences (see Carollo et al. 2016). Despite these limitations, the diagram has proven to be useful for identifying Pop. II stars (see, for example, Schuster et al. 2012; Ramírez et al. 2013).

A Toomre diagram for the candidate SX Phe stars is plotted in Fig. 6. The (red) dashed vertical line at -220 km s^{-1} separates the stars with prograde motions from those with retrograde motions and the (blue) dashed curve divides the halo population stars from the thick-disc stars that have total space velocities $80 < T < 180 \text{ km s}^{-1}$. Also plotted in Fig. 6 are the points for 24 of the Kepler-field RR Lyrae stars, where the U , V , W velocities were calculated using the proper motions and distances given in BN12 and the mean velocities

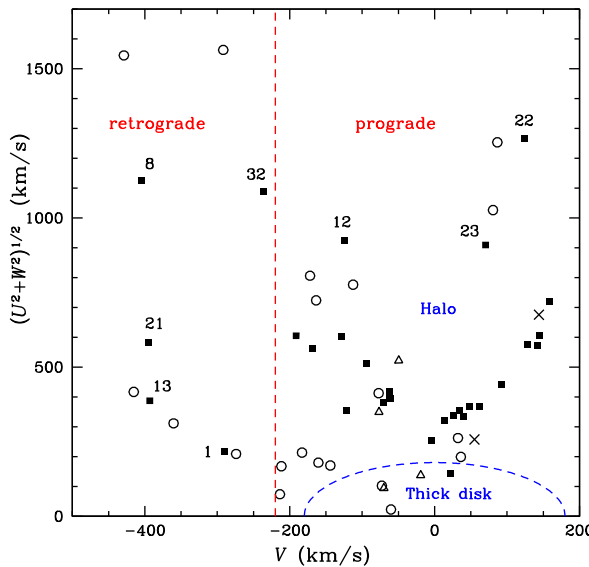


Figure 6. Toomre diagram for the candidate SX Phe stars in the *Kepler* field (solid squares). For comparison purposes, 24 of the *Kepler*-field RR Lyrae stars are also plotted (open circles for metal-poor, open triangles for metal-rich). The vertical line at $v = -220 \text{ km s}^{-1}$ separates stars undergoing retrograde and prograde motion (asymmetric drift) and the curved line at total space velocity $T = 180 \text{ km s}^{-1}$ separates the thick disc and halo stars. The labels for the most extreme SX Phe stars are the CFHT star numbers. The two close binaries that were misclassified as candidate SX Phe stars, KIC 9535881 [*25] and KIC 12643589 [*17], are plotted as crosses.

from Nemec et al. (2013). The metal-poor RR Lyrae stars (i.e. those with $[\text{Fe}/\text{H}] < -1.0 \text{ dex}$) are shown as open circles and the four ‘metal-rich’ RR Lyrae stars (V782 Cyg, V784 Cyg, V2470 Cyg and KIC 11125706) are plotted as open triangles.

Based on the new distances and velocities, we conclude that: (1) half of the stars have z -heights greater than 400 pc; (2) in the Toomre diagram, all the stars (except possibly KIC 6227118 that is located just inside the thick-disc boundary) have total space motions $T > 180 \text{ km s}^{-1}$, including 16 stars with T greater than 500 km s^{-1} ; (3) five of the stars orbit the Galaxy in a retrograde direction;⁵ and (4) the space motions of the SX Phe stars, in particular, the fraction on retrograde orbits, are not substantially different from those of the *Kepler*-field RR Lyrae stars. Each of these findings supports the argument that most, if not all, of the SX Phe candidate stars belong kinematically to the galactic halo stellar population, a conclusion that remains unchanged regardless of whether the z -heights and space motions are based on the new spectroscopic values or on the information in the KIC. Finally, if the galactic halo consists of ‘two broadly overlapping structural components’ as advocated by Carollo et al. (2007, 2016), then the stars with retrograde orbits may be members of the outer-halo component.

⁵ Other well-known field SX Phe stars on retrograde orbits include SX Phe itself, BL Cam (=GD 428) and KZ Hya (see table 1 of Nemec & Mateo 1990b). Given the extreme retrograde motion of the Sloan Digital Sky Survey (SDSS) halo BS J1300+0422 (Tillich et al. 2010), it would be of interest to see if it too is pulsationally unstable.

2.3 Spectral types

SX Phe (and δ Sct) stars usually have spectral types in the range A3 to F2, corresponding to surface temperatures ranging from $\sim 8600 \text{ K}$ to $\sim 6900 \text{ K}$. They also define the blue and red edges of the instability strip at absolute magnitudes $\langle M_V \rangle \sim 1.5$ to 3.5 (i.e. L/L_\odot from ~ 15 to 3). The SX Phe stars found among BSs in globular clusters tend to have, on average, lower luminosities and masses than Pop. I δ Sct stars.

Spectral types and luminosity classes for the programme stars were determined using the rectified CFHT spectra and are given in Table 3 (columns 5–8). Separate classifications were made based on the appearance of the hydrogen lines, the Ca II K-line, and the overall metallic-line spectrum, using the following criteria: (H) the hydrogen Balmer lines have their maximum strength at A2 with the cores and the wings of the lines decreasing in strength as the temperatures decrease; (K) the Ca II K line at 393.3 nm increases in strength towards later spectral types, starting from a line depth comparable to that of the Mg II 448.1 nm line near A0, to a depth that surpasses that of He I at F0; and (M) the line strengths of neutral metals steadily increase towards later spectral types.⁶

For the early-A stars, the luminosity class was established using the hydrogen lines that are luminosity-sensitive and permit discrimination within the main-sequence band. For the early-F stars, the metal lines, which are sensitive to both temperature and luminosity, were used – the primary luminosity indicator being the Fe/Ti $\lambda 4172–9$ blend. The most uncertain luminosity classes are those for the late-A stars where the hydrogen and metal-line criteria do not quite overlap (see Gray & Garrison 1989). Inspection of Table 3 reveals that most of the stars are of luminosity class V and thus are on or near the upper main sequence. Of particular interest is the main-sequence character of KIC 6227118 (*27), whose distance, $\log g$ and $\log L/L_\odot$ in the KIC were found to be outliers by BN12 (see their table 1) and the high-luminosity character of KIC 9244992 (*7) that is consistent with its apparently advanced evolutionary state (see fig. 2 of BN12 and Saio et al. 2015).

For single main-sequence stars application of any one of the above indicators usually gives the same spectral type; however, such agreement is not necessarily expected for A–F stars, especially those having chemical peculiarities, such as the Am stars (at least half of which are spectroscopic binaries), or for SX Phe stars, whose BS nature and possibility of coalescence or mass transfer in binary systems complicates matters. The greatest disparities in spectral type were found for KIC 8004558 and KIC 11754974, both of which are binary systems (see Section 3.3).

Assignment of spectral type can also be problematic for spectra that have broad metal lines (see Fig. 2). Since rotation broadens spectral lines, rapid rotators (at least those with i significantly greater than 0°) have lines that are wider and correspondingly shallower than those for slow rotators. Placing too much emphasis on line depth rather than width may lead to an erroneous classification. To mitigate this problem and improve upon the metal-line spectral types, the spectra of the rapid rotators were compared with the spectra of rapidly rotating standard stars selected from the high

⁶ The G band at 430 nm, which is a useful temperature indicator for mid-to-late F-type stars, was also used to assess the spectral type of KIC 12643589 [*17], one of the two misclassified SX Phe stars and the star with the latest spectral type. Its G-band spectral type is F6 V, which is to be compared with the F5 V type from H_V and F5/F6 from the metal lines. All the spectral indicators are consistent with a relatively cool temperature, $\sim 6500 \text{ K}$.

Table 3. Spectral types, luminosity classes, mean projected rotational velocities, $\langle v \sin i \rangle$ (km s $^{-1}$), and mean radial-tangential macroturbulent velocities, $\langle \zeta_{RT} \rangle$ (km s $^{-1}$), for the *Kepler*-field candidate SX Phe stars. The columns contain: (1) KIC number; (2) CFHT number; (3) RA (J2000) h:m:s; (4) Dec. $^{\circ} : ' : ''$; (5) spectral type based on the K-line, the hydrogen lines and the metal lines; (6) luminosity class; (7) weighted average of the $v \sin i$ values given in Table 1, with the number of spectra measured given in parentheses; (8) mean $v \sin i$ values derived using the goodness-of-fit method; and (11) the average ζ_{RT} derived using the goodness-of-fit method. In the last two columns, the uncertainty is the standard deviation of the mean, and in (11), the number of lines that were measured is given in parentheses.

KIC no. (1)	CFHT no. (2)	RA (J2000) h:m:s (3)	Dec. $^{\circ} : ' : ''$ (4)	Spectral type			Lum. Class (8)	$\langle v \sin i \rangle$		$\langle \zeta_{RT} \rangle$ GOF (11)
				K (5)	H (6)	M (7)		FT (9)	GOF (10)	
1162150	15	19:25:16.66	+37:17:22.84	—	F1	A7	V	225 ± 5 (6)	—	—
3456605	24	19:38:34.22	+38:30:45.46	F0	F0	F0	II/IIIa	13.7 ± 1.7 (3)	11 ± 3	16 ± 3 (20)
4168579	23	19:36:41.30	+39:13:34.36	A8	F1	A9	V	197 ± 4 (6)	—	—
4243461	4	19:01:45.58	+39:19:09.88	A9	A9	A9	V	53.2 ± 0.8 (8)	53 ± 3	29 ± 6 (08)
4662336	14	19:35:29.34	+39:47:26.20	A9	A9	A9	III	83.2 ± 0.6 (4)	—	—
4756040	20	19:37:26.19	+39:49:17.59	A7	F1	F0	V	42.3 ± 2.1 (4)	48 ± 2	18 ± 4 (05)
5036493	26	19:51:29.03	+40:07:58.53	A3	A7	A3	V	19.0 ± 1.1 (4)	18 ± 1	15 ± 1 (27)
5705575	22	19:27:19.60	+40:59:57.71	A5	A9	A6	V	88.2 ± 1.1 (9)	—	—
6130500	9	19:35:48.64	+41:27:13.79	—	—	F0	IV:	49.3 ± 1.1 (6)	48 ± 1	25 ± 2 (20)
6227118	27	19:50:33.67	+41:35:04.07	A6	A8	A5	V	133 ± 2 (4)	—	—
6445601	2	19:30:55.42	+41:50:28.11	F2	F2	F2	V	71.3 ± 0.4 (6)	70 ± 2	25 ± 4 (20)
6520969	21	19:25:27.08	+41:56:30.11	A3	A7	A3	V	$<5.8 \pm 0.8$ (3)	$<8 \pm 1$	15 ± 2 (35)
6780873	5	19:31:32.23	+42:12:22.83	F1	F1	F1	IV	$<8 \pm 1$ (3)	$<8 \pm 1$	16 ± 1 (13)
7020707	16	19:09:46.88	+42:35:07.20	—	F1	F0	V	105 ± 2 (4)	—	—
7174372	8	18:45:48.25	+42:43:36.90	A9	A9	A9	III	41.6 ± 1.0 (9)	41 ± 1	26 ± 2 (21)
7301640	10	19:48:28.67	+42:51:41.00	A9	A9	A9	V	123 ± 2 (5)	—	—
7621759	6	19:43:22.63	+43:14:43.47	F1	F1	F1	IV/V	77.7 ± 1.0 (5)	—	—
7765585	28	19:43:22.71	+43:24:29.74	A9	A9	A9	V	122 ± 1 (6)	—	—
7819024	19	19:22:38.01	+43:33:08.38	A9	F1	A9	V	95.1 ± 1.3 (8)	—	—
8004558	1	18:40:04.07	+43:52:18.06	A2.5	F0	A2	V	84.2 ± 2.6 (7)	—	—
8110941	29	19:44:57.95	+43:57:15.65	F0	F0	F0	III	$<7.5 \pm 0.2$ (4)	$<6 \pm 1$	11 ± 1 (19)
8196006	30	20:02:23.14	+44:01:32.08	—	F0	F2	V	92.6 ± 1.3 (4)	—	—
8330910	3	20:04:23.03	+44:15:22.01	—	—	—	—	224 ± 3 (4)	—	—
9244992	7	20:01:57.43	+45:37:15.59	F0	F0	F0	II	$<6.7 \pm 0.3$ (5)	$<6 \pm 1$	12 ± 3 (13)
9267042	12	18:58:52.07	+45:44:57.85	A7	A7	A3	V	106 ± 3 (11)	—	—
9535881	[25]	19:42:14.31	+46:10:40.94	F0.5	F0.5	F0.5	V	54.6 ± 1.7 (4)	62 ± 2	18 ± 5 (09)
9966976	31	19:50:46.42	+46:49:28.71	F0	F0	F0	V	123 ± 1 (4)	—	—
10989032	32	19:49:34.46	+48:24:38.88	A5	A5	A5	V	45.0 ± 0.9 (8)	44 ± 1	15 ± 2 (26)
11649497	11	18:56:55.73	+49:44:33.42	—	A6	F0	III	$<5.6 \pm 0.2$ (6)	$<5 \pm 1$	12 ± 2 (07)
11754974	13	19:08:15.95	+49:57:15.56	A3	F1	A2	V	28.8 ± 1.7 (8)	31 ± 1	13 ± 2 (21)
12643589	[17]	19:13:17.13	+51:43:35.59	—	F5	F5.5	V	28.7 ± 0.1 (5)	32 ± 2	18 ± 2 (06)
12688835	18	19:15:01.07	+51:50:55.34	A3	A7	A3	V	230 ± 5 (5)	—	—

$v \sin i$ standard star lists provided by Gray & Garrison (1989), Gray & Corbally (1994, 2009), and Gray, Graham & Hoyt (2001).

Owing to instrumental artefacts, arising perhaps as remnants of the merging of the orders in the echelle spectra, certain lines were less useful than others for classification purposes. For instance, the H δ line was often unnatural in shape. For this reason, the assigned hydrogen line type was always determined from H γ and occasionally checked against H δ . Often, it was difficult to find the continuum near the Ca II K-line, in which case a Ca II K-line type is not provided in Table 3. In general, the least weight was placed on the K-line when it was used in the classifications.

2.4 Rotational and macroturbulent velocities

The spectra exhibit a wide range of line widths, with two-thirds of the stars having broad lines (see Fig. 2). Stellar rotation is usually the dominant broadening mechanism; however, macroturbulence and pulsations may also be contributing factors. For stars with narrow lines (which tend to be the slowest rotators but may, like Procyon, be fast rotators seen pole-on), the line profile shapes are determined mainly by instrumental and natural broadening, photospheric ther-

mal motions, Coulomb interactions of neighbouring particles and microturbulence.

2.4.1 Projected equatorial rotation velocities

The projected equatorial rotation velocity, $v \sin i$, was measured for each spectrum using the Fourier transform (FT) method pioneered by Carroll (1928, 1933) and further developed by Gray (1973, 1975, 1978), Smith & Gray (1976) and others (Dravins 1982; Reiners & Schmitt 2002; Reiners & Royer 2004; Simón-Díaz & Herrero 2007, 2014).⁷ Since most of the available spectra have S/N < 100, no attempt was made to measure differential rotations or to investigate line bisectors. The $v \sin i$ values given in Table 1 (column 9) were derived using the ‘RCROS’ program of Díaz et al.

⁷ The v in $v \sin i$ is the equatorial velocity and the inclination angle, i , is the angle between the observer’s line of sight and the direction of the rotation axis. This i is not to be confused with the orbital inclination angle used in Section 3 to describe the binary systems, where i is the angle between the line of sight and the line perpendicular to the orbital plane.

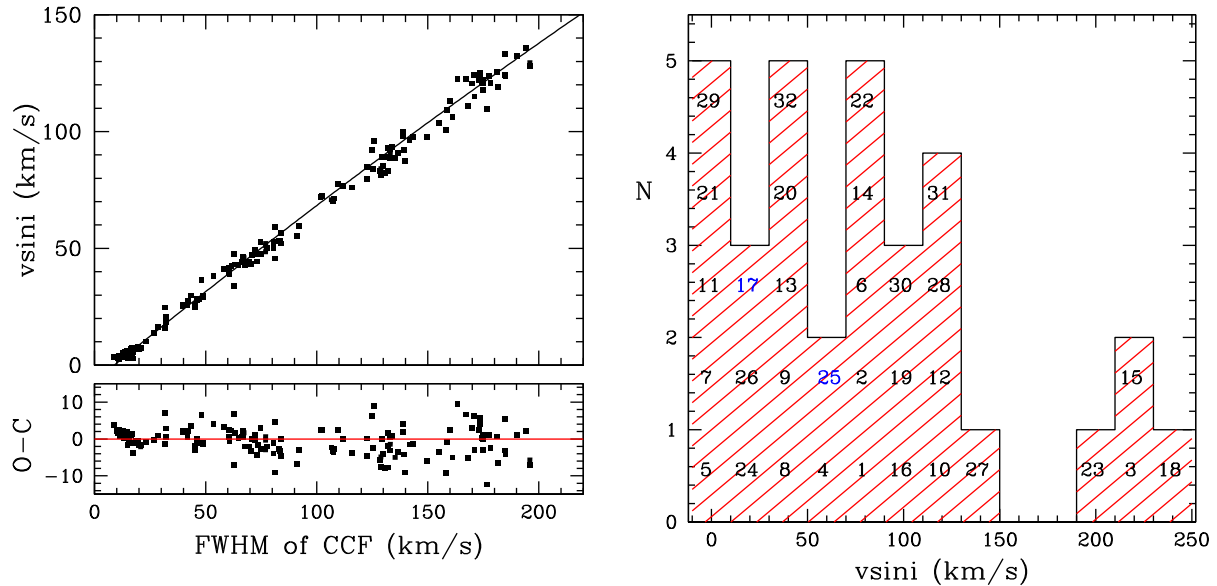


Figure 7. Left: the upper panel shows the correlation between the $v \sin i$ values derived using the Díaz et al. (2011) Fourier transform method and the Gaussian FWHM of the CCF (object-template). The lower panel shows the residuals from the quadratic fit, the rms scatter about zero amounting to ~ 6 km s $^{-1}$. Right: histogram of the derived mean $v \sin i$ values for the *Kepler*-field candidate SX Phe stars. The labels are the CFHT star numbers (see Table 1) and are coloured blue for the two close binaries misclassified as candidate SX Phe stars: KIC 9535881 [*25] and KIC 12643589 [*17].

(2011). This algorithm calculates the CCF between an object spectrum and a template spectrum, where user-specified wavelength intervals (e.g. 200–400 Å) replace individual lines. The $v \sin i$ values follow from the location of the first zero in the FT of the CCF central maximum (assuming a linear limb darkening law with $\epsilon = 0.6$ and taking account of wavelength-dependence). For our spectra, the method has several advantages over measuring individual line profiles, the greatest being that in the FTs; the first zeros were usually well defined with sidelobe signatures significantly higher than the background noise level. Using simulations, Díaz et al. concluded that ‘for the usual values of S/N and instrumental broadening, the variation in the first zero position caused by additional broadening and noise is below 1 per cent.’ Selection of the template spectra depended on the amount of line broadening. For the spectra with broad lines, both narrow- and broad-lined templates appropriate for A- and early-F spectral types were used, including synthetic spectra with $v \sin i$ values equal to 10, 50 and 100 km s $^{-1}$. For the stars with narrow-lined spectra (including the RV standards), the adopted template spectrum consisted of either a synthetic solar spectrum, an A-star spectrum or the spectrum of one of the very narrow-lined programme or standard stars.

The derived $v \sin i$ values correlate well with the measured Gaussian FWHM values of the CCFs (see the left-hand panel of Fig. 7). Because the four fastest rotators have CCFs that deviate from a Gaussian distribution they have been excluded from the graph; no corrections were made for the ~ 4 km s $^{-1}$ instrumental broadening. The quadratic least-squares fit is given by $y = -2.859 \times 10^{-4}x^2 + 0.781x - 6.888$, where x is the FWHM of the CCF and y is the value of $v \sin i$. The residuals have an rms scatter of approximately 6 km s $^{-1}$. The uncertainties in the $v \sin i$ values depend on the width of the CCF central maximum, the height of the CCF peak and the noise in the CCF. The largest random errors occur for the fastest rotators with the broadest lines. For the narrow-lined spectra, the rotational broadening is comparable in magnitude to the instrumental and other broadenings mentioned above and hence the $v \sin i$ values are upper limits.

Weighted-average $v \sin i$ values based on the FT method applied to all the spectra are given in column 9 of Table 3 and a histogram of the $\langle v \sin i \rangle$ values is plotted in the right-hand panel of Fig. 7. Although the number of stars is relatively small, the distribution appears approximately uniform between 0 and 150 km s $^{-1}$, with the four fastest rotators having $\langle v \sin i \rangle$ values greater than 195 km s $^{-1}$. The four slowest rotators have $\langle v \sin i \rangle$ values smaller than 8 km s $^{-1}$ and about two-thirds of the stars have $v \sin i$ values larger than 50 km s $^{-1}$. Since main-sequence A-type stars generally have $v \sin i$ values ranging from the resolution limit of the instrumentation to nearly as high as the rotational break-up limit ~ 350 km s $^{-1}$ and because F-type stars tend to rotate much more slowly (see fig. 18.21 of Gray 2005, fig. 1 of Royer, Zorec & Gómez 2007 and fig. 11 of Bruntt et al. 2010a), the observed range of line broadenings meets expectations for a sample of A- and early-F type stars.

2.4.2 Macroturbulent velocities

The existence of granulation cells larger than the mean free path of a photon (i.e. macroturbulence; see Gray 2005, Chapter 17) is often invoked to explain line broadening in excess of that attributed to rotation. It has been suggested that gravity waves, possibly originating with non-radial oscillations (Lucy 1976; de Jager 1990; Aerts et al. 2009, 2014; Cantiello et al. 2009; Simón-Díaz et al. 2010; Balona 2011; Schiude et al. 2013; Grassitelli et al. 2015), may cause or contribute to macroturbulent broadening. In many cases, the amount of line broadening due to macroturbulence may be as much or more than that caused by rotation (e.g. Markova et al. 2014).

The radial-tangential macroturbulent velocity dispersion, ζ_{RT} (Gray 1973, 1975, 1978), was estimated for 16 BN12 stars using the ‘IACOB-broad’ tool of Simón-Díaz & Herrero (2014). Artificial line profiles were fitted to unblended high-SNR lines in the observed spectra by varying $v \sin i$ and ζ_{RT} , where the combined FT and goodness-of-fit (GOF) methodology was used to

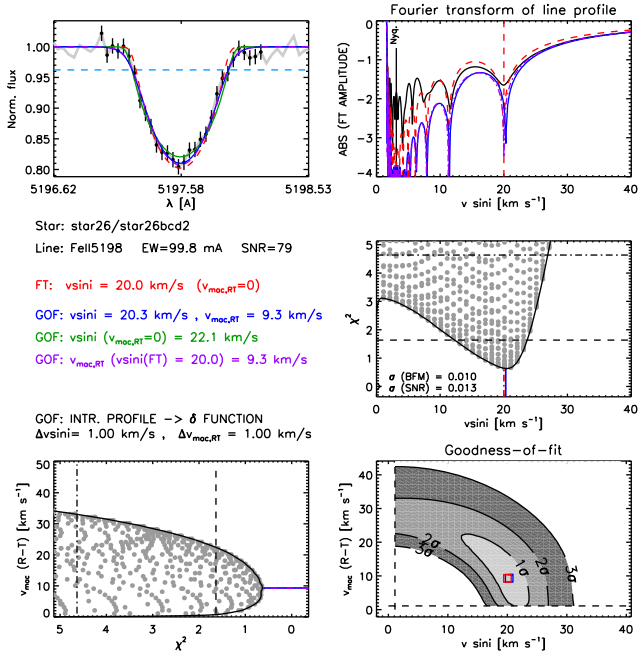


Figure 8. Example output from the ‘iacob-broad tool’ that was used to estimate radial-tangential macroturbulent velocity, ζ_{RT} , and the projected rotation velocity, $v \sin i$. Here, the strong Fe II line at 5197.58 Å was measured in the co-added spectrum of KIC 5036493 (*26). The resulting FT and GOF $v \sin i$ values for this line are in excellent agreement with the $(v \sin i)$ value derived using ‘rcros’, $19.0 \pm 1.1 \text{ km s}^{-1}$. The resulting ζ_{RT} of $9 \pm 8 \text{ km s}^{-1}$ (the uncertainty follows from the contour plot in the bottom-right panel) is smaller than, but consistent with, the mean value of $\langle \zeta_{\text{RT}} \rangle = 15 \pm 1 \text{ km s}^{-1}$ derived from measurements of this line and 26 other lines in the same spectrum.

infer the optimum (minimum χ^2) values of $v \sin i$ and ζ_{RT} for each line. These values were then averaged over lines to give the final estimates for each star, which are given in the last two columns of Table 3.

An application of the iacob-broad tool is illustrated in Fig. 8. The upper-left panel shows observed and fitted profiles for the 5197.58 Å Fe II line in the spectrum of KIC 5036493 (*26). The upper-right panel shows the FT of the observed line profile, where the first dip corresponds to the $v \sin i$ value if $\zeta_{\text{RT}} = 0$; the middle-right and lower-left panels show χ^2 plots; and the middle-left panel summarizes the FT and GOF estimates. Here, and for most of the other stars, the FT and GOF values are consistent. Plots similar to the bottom-right contour graph, where the ‘banana-shaped’ contours reflect the relation $v_{\text{tot}}^2 = [(v \sin i)^2 + \zeta_{\text{RT}}^2)]^{1/2}$ introduced by Saar & Osten (1997), have been presented by Ryans et al. (2002), Dall et al. (2010) and Bruntt et al. (2010b). Since the GOF $v \sin i$ values agree extremely well with those derived using the ‘rcros’ FT method (see Section 2.4.1), the latter were adopted and only the ζ_{RT} retained.

Fig. 9 shows that the derived macroturbulent velocity dispersions fall in the range $10\text{--}30 \text{ km s}^{-1}$, with an apparent trend of increasing ζ_{RT} with increasing $v \sin i$. Without knowing the inclination angle, it is hard to know whether there is a correlation between the equatorial velocity and ζ_{RT} .

For main-sequence stars, the ‘granulation boundary’ that marks the onset of convection (Böhm-Vitense 1958; Böhm-Vitense & Canterna 1974; Gray & Nagel 1989; Paxton et al. 2011, 2013, 2015)

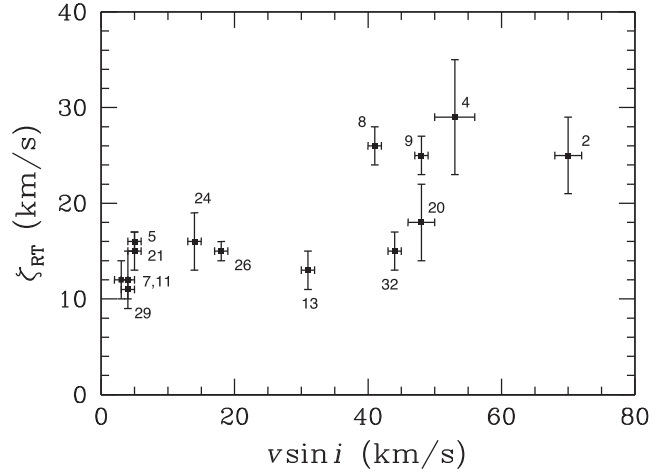


Figure 9. Macroturbulent velocity dispersion, ζ_{RT} , versus projected equatorial velocity, $v \sin i$, for 14 SX Phe stars. The labels are the CFHT star numbers.

occurs near spectral type F0, corresponding to $B-V \sim 0.3$ and $T_{\text{eff}} \sim 7000 \text{ K}$. This boundary appears to be coincident with the red edge of the Cepheid instability strip (Böhm-Vitense & Nelson 1976). Since the stars considered here are mainly mid-to-late A-type pulsators with $(B-V)_0 < 0.30 \text{ mag}$ (see Table 4), they tend to lie on the hot side of the granulation boundary in the instability strip. Such stars might be expected to have reversed-C shaped line bisectors (Gray & Toner 1986; Gray 2009) and possibly significant atmospheric velocity fields (Landstreet 1999; Landstreet et al. 2009). In addition, many may have chemical abundance anomalies (Preston 1974; Adelman 2004) that are undoubtedly related to magnetic fields (Donati & Landstreet 2009) and diffusion (Michaud et al. 1976).

The hotter and more luminous OB-stars (for which microturbulence is assumed to be negligible) tend to have very large ζ_{RT} values, possibly as high as $\sim 150 \text{ km s}^{-1}$, which appear to increase with increasing T_{eff} and $v \sin i$ (see Ryans et al. 2002; Markova et al. 2014; Simon-Diaz & Herrero 2014). On the cool side of the granulation boundary, the F-, G- and K-type stars (see Gray 1988) tend to show an increase in ζ_{RT} with increasing temperature (and luminosity). For the Sun $\zeta_{\text{RT}} \sim 3.5 \text{ km s}^{-1}$ and F5 V stars, values reach $\sim 6 \text{ km s}^{-1}$ (see fig. 17.10 of Gray 2005; Bruntt et al. 2010a; Doyle et al. 2014). Fig. 3 of Valenti & Fischer (2005) shows that for stars with $T_{\text{eff}} = 6200 \text{ K}$, the upper limit of ζ_{RT} is $\sim 9\text{--}10 \text{ km s}^{-1}$. Such cool stars tend to be slow rotators, have C-shaped line bisectors (Gray 1988, 2009; Gray & Nagel 1989) and show chromospheric emission in ultraviolet (UV) spectra (Böhm-Vitense & Dettmann 1980; Gray & Toner 1986). Simple interpolation suggests that our programme stars might be expected to have intermediate ζ_{RT} values, which is, in fact, borne out by the observation that the average $\langle \zeta_{\text{RT}} \rangle = 18 \pm 2 \text{ km s}^{-1}$ for the measured stars.

Recent precise $v \sin i$ and ζ_{RT} measurements made by Gray (2014) for five narrow-lined A0–A2 main-sequence stars show them to have much lower ζ_{RT} values than the hot but slightly cooler stars studied here. It is perhaps significant that our sample stars are all pulsating while the stars studied by Gray are outside the instability strip and do not appear to pulsate. This observation lends support to the notion that the relatively high macroturbulent velocity dispersions of the SX Phe stars are due to (or at least related to) non-radial pulsations.

Table 4. Atmospheric characteristics for 32 of the 34 candidate SX Phe stars in the *Kepler* field. For all the stars, the first row gives the SME estimates, and when vwa/MOOG estimates (based on the EW/COG method) were also made, they are given on the second row. Assumed and uncertain values are given in parentheses. The KIC and CFHT star numbers are given in the first two columns. The third to ninth columns give, respectively, the derived surface gravity, effective temperature, microturbulent velocity and metal abundance. For comparison purposes, the table also contains the KIC and Huber et al. (2014) photometrically based values.

KIC no. (1)	CFHT no. (2)	log g (cm s $^{-2}$)		T_{eff} (K)		ξ_t (km s $^{-1}$)	[Fe/H] (dex)	
		KIC, H14 (3)	This paper (4)	KIC, H14 (5)	This paper (6)	This paper (7)	KIC, H14 (8)	This paper (9)
1162150	15	3.46, 3.49	3.61 ± 0.10	6871, 7090	7390 ± 50	(7 ± 2)	-0.01, +0.02	-0.20 ± 0.30
3456605	24	3.94, 3.94	3.99 ± 0.05	7112, 7353	7460 ± 90	3.8 ± 0.1	-0.18, -0.18	$+0.50 \pm 0.10$
			4.2 ± 0.2		7630 ± 50	2.8 ± 0.2		$+0.58 \pm 0.11$
4168579	23	3.79, 3.84	3.57 ± 0.08	7534, 7757	7750 ± 90	5.3 ± 2.0	-0.09, -0.1	$+0.08 \pm 0.20$
4243461	4	4.15, 4.20	4.33 ± 0.05	6918, 7159	7740 ± 50	6.8 ± 0.2	-0.24, -0.22	$+0.11 \pm 0.15$
4662336	14	3.89, 3.88	3.95 ± 0.05	7211, 7452	7450 ± 50	5.9 ± 0.1	-0.13, -0.14	-0.05 ± 0.15
4756040	20	4.09, 4.09	4.08 ± 0.05	7603, 7837	7720 ± 50	4.9 ± 0.3	-0.01, -0.02	-0.15 ± 0.20
			4.1 ± 0.2		7650 ± 100	2.8 ± 0.2		-0.12 ± 0.15
5036493	26	3.95, 3.97	(4.7 ± 0.2)	7962, 8148	8430 ± 100	2.7 ± 0.2	+0.00, +0.07	-0.02 ± 0.15
			4.5 ± 0.2		8250 ± 100	2.4 ± 0.3		-0.22 ± 0.20
5705575	22	3.99, 4.03	4.00 ± 0.05	7583, 7785	7860 ± 50	(10 ± 2)	-0.16, -0.18	-0.1 ± 0.2
6130500	9	4.14, 4.11	4.1 ± 0.2	7581, 7801	7820 ± 100	5.3 ± 1.0	-0.01, -0.02	-0.07 ± 0.20
6227118	27	1.03, 2.84	(4.5 ± 0.3)	7217, 7197	7500 ± 200	4.2 ± 1.0	-0.15, -0.5	$(+0.04 \pm 0.20)$
6445601	2	4.09, 4.11	3.90 ± 0.15	7186, 7419	7450 ± 60	6.0 ± 0.5	-0.17, -0.16	$+0.3 \pm 0.2$
6520969	21	3.96, 3.78	(3.80)	8355, 8572	8250 ± 50	2.7 ± 0.3	-0.13, -0.2	-0.7 ± 0.2
			4.3 ± 0.2		7730 ± 100	2.4 ± 0.2		-0.84 ± 0.16
6780873	5	4.35, 4.36	4.03 ± 0.08	6874, 7158	7530 ± 50	3.7 ± 0.4	-1.09, -1.1	$(+0.0 \pm 0.3)$
			4.3 ± 0.2		7200 ± 100	1.3 ± 0.3		$(+0.16 \pm 0.20)$
7020707	16	4.00, 3.95	3.93 ± 0.05	7447, 7689	7560 ± 50	(10 ± 2)	-0.21, -0.2	-0.2 ± 0.2
7174372	8	4.10, 4.10	3.4 ± 0.2	7228, 7457	7740 ± 100	3.4 ± 0.5	-0.30, -0.3	-0.2 ± 0.2
			3.7 ± 0.2		7380 ± 100	2.1 ± 0.2		$+0.11 \pm 0.20$
7301640	10	4.07, 4.13	4.2 ± 0.2	7014, 7239	8000 ± 100	(14 ± 2)	-0.01, +0.02	$+0.45 \pm 0.15$
7621759	6	4.05, 4.02	(4.02)	6966, 7316	7800 ± 80	(11 ± 2)	-0.26, -0.24	(-0.24)
7765585	28	4.80, 4.31	(4.31)	6714, 6853	7800 ± 150	(9 ± 2)	+0.15, +0.07	$+0.15 \pm 0.10$
7819024	19	4.10, 4.10	4.13 ± 0.10	7534, 7758	7690 ± 50	7.0 ± 1.5	-0.27, -0.32	$+0.00 \pm 0.20$
8004558	1	3.90, 3.89	4.3 ± 0.2	7674, 7899	7950 ± 100	5.2 ± 0.4	-0.45, -0.44	-0.3 ± 0.2
8110941	29	4.13, 4.13	4.13 ± 0.05	6839, 7177	7350 ± 150	2.9 ± 0.5	-0.09, -0.06	$+0.1 \pm 0.2$
			4.0 ± 0.2		7300 ± 150	2.5 ± 0.5		$+0.06 \pm 0.20$
8196006	30	4.25, 4.28	4.27 ± 0.05	7015, 7232	7740 ± 65	(10 ± 2)	-0.44, -0.44	$+0.16 \pm 0.20$
8330910	3	4.06, 4.07	(4.13)	7379, 7599	8000 ± 60	(7 ± 2)	-0.20, -0.24	-0.1 ± 0.3
9244992	7	3.51, 3.52	3.52 ± 0.15	6592, 6902	7550 ± 100	4.5 ± 0.7	-0.14, -0.16	$+0.1 \pm 0.3$
9267042	12	3.80, 3.76	4.28 ± 0.10	8128, 8354	8200 ± 80	(8 ± 2)	-0.11, -0.14	-0.02 ± 0.20
9535881	[25]	4.18, 4.07	3.97 ± 0.05	7161, 7397	7520 ± 70	6.1 ± 0.8	-0.22, -0.2	-0.03 ± 0.15
9966976	31	3.93, 3.92	4.32 ± 0.06	7638, 7872	7740 ± 50	(7 ± 2)	+0.05, +0.07	$+0.02 \pm 0.10$
10989032	32	4.07, 4.08	(4.10)	8610, 8851	8630 ± 100	(5 ± 2)	-0.01, +0.07	$+0.3 \pm 0.3$
11649497	11	4.02, 4.03	3.98 ± 0.05	7656, 7904	7650 ± 80	4.4 ± 0.1	-0.10, -0.04	$+0.2 \pm 0.2$
11754974	13	–, 3.98	3.98 ± 0.05	–, 7231	7500 ± 50	2.3 ± 0.2	–, +0.01	-1.1 ± 0.2
			4.0 ± 0.2		7300 ± 150	2.1 ± 0.3		-1.4 ± 0.2
12643589	[17]	4.44, 4.39	4.40 ± 0.15	6501, 6657	7000 ± 50	4.3 ± 0.4	-0.26, -0.34	$+0.14 \pm 0.20$
12688835	18	3.86, 3.81	4.3 ± 0.4	8531, 8759	8330 ± 80	(7 ± 3)	-0.28, -0.3	-0.15 ± 0.10

2.5 Other atmospheric characteristics

In addition to $v \sin i$ and ζ_{RT} velocities, several other atmospheric characteristics were derived from the spectra. These include: effective temperature, T_{eff} ; surface gravity, $\log g$; microturbulent velocity, ξ_t and metal abundance, [Fe/H]. Since the *Kepler* SX Phe sample consists of stars exhibiting a wide range of linewidths and metallicities, stars with radial speeds as high as 300 km s $^{-1}$, close and wide binary systems, etc. and spectra with a wide range of SNRs, it was necessary to employ several different methods for the spectral data analyses. In general, synthetic spectra were fitted to observed spectra, where χ^2 minimization techniques were used to optimize atmospheric parameters. In all cases, 1D plane-parallel atmospheres in local thermodynamic equilibrium were assumed. Specifically, the ATLAS9 model atmospheres of Kurucz (see Castelli &

Kurucz 2004) were used for the radiative transfer calculations. Basic spectral line information (excitation potentials, loggf values) was taken from the VALD3 website (Piskunov et al. 1995; Kupka et al. 1999) and for the assumed composition mix, the Asplund et al. (2009) solar abundances were adopted.

All the spectra (both individual and co-added) were measured using the ‘Spectroscopy Made Easy’ (SME) program of Valenti & Piskunov (1996). Initially, wavelength ranges were limited to the same ‘windows’ used by Valenti & Fischer (2005), supplemented by regions around the first three Balmer lines. The results were then refined using simultaneous fitting of the 25 wavelength windows as advocated by Brewer et al. (2015 – see their table 2), where the initial estimates served as starting values. A sample fit for a portion of the KIC 7020707 spectrum can be found in Nemec et al. (2015).

Table 5. Mean magnitudes and colours for the *Kepler*-field SX Phe candidates. The columns contain: (1 and 2) KIC and CFHT star numbers; (3) mean *Kepler* Kp magnitude from the KIC; (4–6) mean Johnson v magnitudes, $B-V$ colours and $U-B$ colours – the top row is from Everett et al. (2012) and the lower rows are new photometric observations; (7 and 8) dereddened $B-V$ and $U-B$ colours, assuming both the KIC and new reddenings (given in Table 2); (9) Gunn–Thuan (SDSS) $g-r$ colour from the KIC catalogue and from the Kepler-INT Survey (KIS); (10–12) $r-i$, $H-K$ and $J-K$ colours given in the KIC.

KIC no.	CFHT no.	Kp (KIC)	V	$B-V$	$U-B$	$(B-V)_0$ Everett et al. (2012), new (this paper)	$(U-B)_0$ KIC, new	$g-r$ KIC, KIS	$r-i$ (KIC)	$H-K$ (KIC)	$J-K$ (KIC)
(1)	(2)	(3)	(4)	(5)	(6)	(7)	(8)	(9)	(10)	(11)	(12)
1162150	15	11.240	–	–	–	–, –	–, –	0.233, 0.352	0.012	0.032	0.292
3456605	24	13.108	13.181	0.452	0.154	0.25, 0.31	0.01, 0.05	0.235, 0.422	0.015	0.058	0.208
4168579	23	13.612	13.720	0.373	0.021	0.12, 0.20	–0.16, –0.10	0.205, 0.347	0.032	0.028	0.172
4243461	4	13.786	13.856	0.360	0.070	0.21, 0.25	–0.04, –0.01	0.185, 0.361	–0.009	0.019	0.170
			13.765	0.335	0.043	0.18, 0.23	–0.07, –0.04				
4662336	14	13.105	13.258	0.389	0.070	0.19, 0.27	–0.08, –0.02	0.225, 0.394	0.030	0.032	0.198
4756040	20	13.315	13.396	0.345	0.019	0.14, 0.24	–0.13, –0.06	0.160, 0.371	–0.012	0.005	0.181
5036493	26	12.553	12.626	0.315	0.110	0.09, 0.05	–0.05, –0.08	0.103, 0.242	–0.049	0.167	0.138
5390069	–	15.110	15.241	0.475	0.132	0.30, 0.29	0.01, 0.00	0.310, 0.411	0.075	0.059	0.275
5705575	22	13.692	13.718	0.341	0.011	0.13, 0.25	–0.14, –0.05	0.162, 0.313	–0.019	–0.058	0.075
			13.579	0.338	0.041	0.13, 0.25	–0.11, –0.04				
6130500	9	13.869	13.880	0.331	0.054	0.12, 0.21	–0.10, –0.03	0.174, 0.321	–0.010	0.017	0.128
6227118	27	12.932	13.013	0.366	0.066	0.00, 0.25	–0.20, –0.02	–0.015, 0.306	–0.016	0.090	0.177
6445601	2	13.595	13.679	0.383	0.050	0.20, 0.30	–0.08, –0.01	0.216, 0.411	0.028	0.036	0.215
6520969	21	13.422	13.486	0.187	–0.061	–0.03, 0.11	–0.21, –0.12	0.023, 0.222	–0.066	0.026	0.126
6780873	5	13.746	13.827	0.386	0.049	0.23, 0.33	–0.06, 0.01	0.231, 0.434	0.069	0.041	0.214
			13.773	0.447	–0.052	0.29, 0.39	–0.16, –0.13				
7020707	16	13.433	–	–	–	–, –	–, –	0.141, 0.310	–0.016	0.007	0.144
7174372	8	13.621	13.633	0.374	0.109	0.24, 0.32	0.01, 0.07	0.162, 0.345	0.002	0.053	0.165
			13.640	0.331	0.053	0.20, 0.28	–0.04, –0.03				
7300184	–	15.430	15.563	0.504	0.163	0.32, 0.23	0.03, –0.03	0.377, 0.485	0.100	0.061	0.288
7301640	10	13.862	13.971	0.367	0.125	0.16, 0.11	–0.03, –0.06	0.285, 0.430	0.039	0.046	0.180
7621759	6	13.912	14.033	0.467	0.002	0.26, 0.28	–0.15, –0.13	0.267, 0.446	0.070	–0.044	0.137
7765585	28	13.980	14.085	0.451	0.165	0.34, 0.27	0.08, 0.04	0.288, 0.395	0.039	0.096	0.263
			14.010	0.424	0.095	0.31, 0.24	0.01, 0.02				
7819024	19	13.799	13.886	0.317	–0.078	0.13, 0.27	–0.21, –0.11	0.140, 0.327	–0.002	0.024	0.179
			13.781	0.325	–0.055	0.14, 0.28	–0.19, –0.13				
			13.793	0.309	–0.051	0.13, 0.26	–0.18, –0.13				
8004558	1	13.350	13.296	0.310	–0.121	0.18, 0.26	–0.22, –0.16	0.053, 0.251	–0.040	0.071	0.163
			13.390	0.255	–0.123	0.12, 0.21	–0.22, –0.20				
8110941	29	13.749	13.798	0.449	0.082	0.27, 0.30	–0.05, –0.03	0.286, 0.472	0.049	0.068	0.253
8196006	30	13.810	13.903	0.435	0.079	0.24, 0.12	–0.06, –0.15	0.265, –	0.069	0.095	0.278
8330910	3	13.457	13.520	0.389	0.072	0.16, 0.08	–0.09, –0.15	0.216, 0.407	0.033	0.050	0.229
9244992	7	13.998	14.206	0.571	0.191	0.28, 0.35	–0.02, 0.03	0.429, 0.561	0.156	0.110	0.286
9267042	12	13.424	13.447	0.233	–0.004	0.08, 0.18	–0.12, –0.04	0.001, 0.175	–0.117	–0.023	0.086
			13.409	0.202	0.006	0.05, 0.15	–0.11, –0.07				
9535881	[25]	13.402	13.466	0.349	0.010	0.18, 0.28	–0.11, –0.04	0.204, 0.395	0.030	0.006	0.163
9966976	31	13.491	13.577	0.356	0.039	0.14, 0.27	–0.12, –0.03	0.173, 0.278	–0.025	0.027	0.142
			13.517	0.285	0.018	0.06, 0.20	–0.14, –0.06				
10989032	32	13.866	13.933	0.240	0.056	0.01, 0.14	–0.11, –0.02	0.013, 0.199	–0.106	–0.034	–0.002
11649497	11	13.432	13.454	0.252	0.089	0.11, 0.21	–0.01, 0.06	0.083, 0.270	–0.059	–0.035	0.105
11754974	13	12.678	12.605	0.255	–0.158	–, 0.22	–, –0.19	0.148, 0.234	–0.046	–0.010	0.128
			12.570	0.259	–0.174	–, 0.22	–, –0.25				
12643589	[17]	13.754	13.858	0.457	0.028	0.35, 0.41	–0.05, –0.01	0.305, 0.459	0.071	0.023	0.267
			13.831	0.493	–0.028	0.38, 0.44	–0.11, –0.11				
			13.815	0.489	–0.004	0.38, 0.44	–0.08, –0.08				
			13.833	0.481	–0.016	0.37, 0.43	–0.10, –0.10				
12688835	18	13.801	13.806	0.169	0.025	0.01, 0.14	–0.09, 0.00	–0.078, 0.178	–0.072	–0.118	–0.018

For those narrow-lined stars for which equivalent widths (EWs) of unblended lines could be reliably measured, the curve-of-growth (COG) method, also known as the EW method, was used to derive a second set of estimated atmospheric characteristics. The analyses were performed using both the MOOG program (Sneden 1973) and vWA (Bruntt et al. 2002). For the MOOG analyses, the EWs were measured using ARES (Sousa et al. 2007, 2015), while for the vWA

analyses, they were measured as part of the reductions. To help ensure the comparability of the results from vWA and MOOG, every attempt was made to measure the same iron lines; usually there was good agreement. vWA diagnostic diagrams were plotted, including derived iron abundances, $A(\text{Fe}) (= \log N_{\text{Fe}}/N_{\text{tot}})$, versus measured EW, and $A(\text{Fe})$ versus lower excitation potential (EP). The T_{eff} values were derived by requiring independence of $A(\text{Fe})$ and EP.

The microturbulent velocities ξ_t were derived by requiring independence of A(Fe) and EW and the $\log g$ were derived by requiring similar mean A(Fe) values for the Fe I and Fe II lines (i.e. ionization equilibrium).

The results of the spectral analyses are summarized in Table 4, where the first row for each star summarizes the parameter estimates derived using SME, and the second row gives, if available, the results of the most reliable VWA/MOOG analyses; also given are the photometric estimates from the KIC and from Huber et al. (2014). When individual parameters were assumed, such as for the difficult-to-measure surface gravity, the values that were assumed are given in parentheses, otherwise derived values (with uncertainties) are recorded. Since the T_{eff} and $\log g$ estimates ignore variation over the pulsation cycle, the true uncertainties are difficult to estimate and may be larger than the reported values.

2.5.1 Effective temperatures

In BN12, the primary source of temperature information was the KIC, where the T_{eff} values were derived from Gunn–Thuan (SDSS) *griz* and 2MASS *JHK* photometric magnitudes and colours. Since then, several photometric investigations have provided additional information about the temperatures (and other atmospheric characteristics) of the *Kepler*-field programme stars: Pinsonneault et al. (2012) found that for stars with T_{eff} in the range 4000–6500 K, the KIC temperature scale needed a correction of about +200 K; Greiss et al. (2012) presented the *Kepler* Isaac Newton 2.5-m Telescope Survey (KIS) consisting of stellar photometry through *U, g, r, i* and H α filters for over ∼50 per cent of the *Kepler* field; Everett et al. (2012) presented Johnson *U, B, V* photometry for over 4 million sources in the *Kepler* field; and Huber et al. (2014, hereafter H14) constructed a catalogue of revised stellar properties for over 196 000 stars in the *Kepler* field. In Table 5, much of this new photometric data, in particular, colour indices relevant for estimating effective temperatures, have been summarized for our programme stars.

The spectroscopic (SME, VWA/MOOG) and photometric (KIC; H14) effective temperatures for the programme stars are compared in Fig. 10. The stars are seen to have SME temperatures ranging from 7300 to 8600 K (i.e. $3.863 < \log T_{\text{eff}} < 3.934$ K). The upper temperature matches well the blue edge of the theoretical δ Scuti instability strip (e.g. Dupret et al. 2004); however, the lower temperature is a few hundred Kelvins hotter than the theoretical red edge. The top panel reveals a systematic offset of ∼240 K between the KIC and H14 photometric temperatures, consistent with the Pinsonneault et al. upward revision of the KIC temperatures and extending its range to temperatures ∼8600 K. The most extreme outlier is the crowded optical double KIC 6227118 (*27). The middle panel shows that for most of the cooler stars, the SME temperatures are hotter than the H14 temperatures, the average difference being ∼300 K; the largest discrepancies occur for KIC 7765585 (*28) and KIC 7301640 (*10), both of which are rapid rotators. For the five hottest stars, the H14 temperatures appear to be ∼200 K hotter than the SME temperatures, i.e. more in line with the original KIC temperatures. In the bottom panel, the SME and VWA/MOOG spectroscopic temperatures are compared. Apart from a scatter ∼200 K, there is reasonable agreement. The largest discrepancy, ∼500 K, is for KIC 6520969 (*21). We suspect that a large part of the observed difference can be attributed to the different wavelength intervals that were measured.

The T_{eff} values from asteroseismology, 7100 ± 150 K for KIC 11754974 (Murphy et al. 2013b) and 6622 K for KIC 9244992

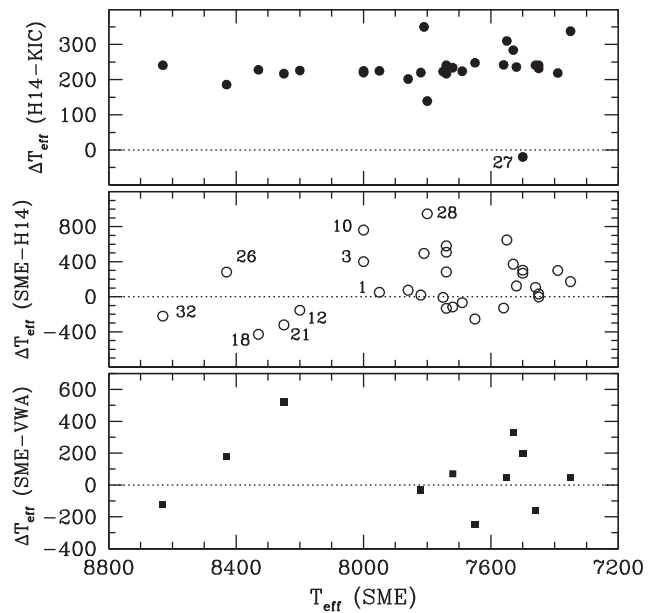


Figure 10. (Top) Comparing the KIC and H14 photometric effective temperatures for the SX Phe candidates reveals a systematic difference of ∼240 K, in agreement with, and extending to hotter temperatures, the conclusion reached earlier by Pinsonneault et al. (2012). KIC 6227118 (*27) is an obvious outlier. (Middle) Comparison of the SME spectroscopic T_{eff} and the H14 photometric T_{eff} values – nine stars have been labelled with the CFHT star number; (Bottom) Comparing the spectroscopically derived effective temperatures.

(Saio et al. 2015), are both somewhat cooler than the spectroscopic values: the KIC 11754974 value is within the measuring errors, but the asteroseismology value for KIC 9244992 is ∼1000 K cooler than that derived here!

In order of decreasing temperature, the five hottest stars ($T_{\text{eff}} > 8100$ K) appear to be: KIC 10989032 (*32), KIC 5036493 (*26), KIC 12688835 (*18), KIC 6520969 (*21) and KIC 9267042 (*12). The hottest of these is a 2.3 d semidetached binary (see Section 3). All five stars have early-A spectral types (see Table 3) and are correspondingly hot in the H14 study. The five coolest stars (excluding the misclassified binary KIC 12643589) appear to be: KIC 6780873 (*5) the newly discovered SB2 system discussed above; the two faint stars not observed spectroscopically, KIC 5390069 and KIC 7300184; KIC 3456605 (*24); and KIC 7174372 (*8).

To establish a relative T_{eff} ranking, four photometric colour–colour graphs have been plotted in Fig. 11. The top-left panel compares the $r-i$ and $g-r$ colours, two of the main indices used by the KIC and by H14. The top-right panel is a plot of the Everett et al. (2012) $B-V$ colours versus the *Kepler*-INT $g-r$ colours and the bottom-left panel shows the near-infrared $H-K$ versus $J-K$ two-colour diagram. In all three graphs, significant linear correlations are seen, which appear to confirm that KIC 10989032 (*32), KIC 12688835 (*18) and KIC 9267042 (*12) are among the hottest stars in the sample (KIC 5036493 was not measured in the near-IR).

The bottom-right panel of Fig. 11 is a two-colour plot of $U-B$ versus $B-V$, where, unlike the other three panels, the broad-band colours have been dereddened using the new reddenings in Table 2 (column 4). The $(B-V)_0$ ordering should, therefore, be closer to a temperature ranking. The graph includes the well-known $U-B$, $B-V$ two-colour main-sequence curve (in this case, based on the colours given in table 1.1 of Böhm-Vitense 1989) with the

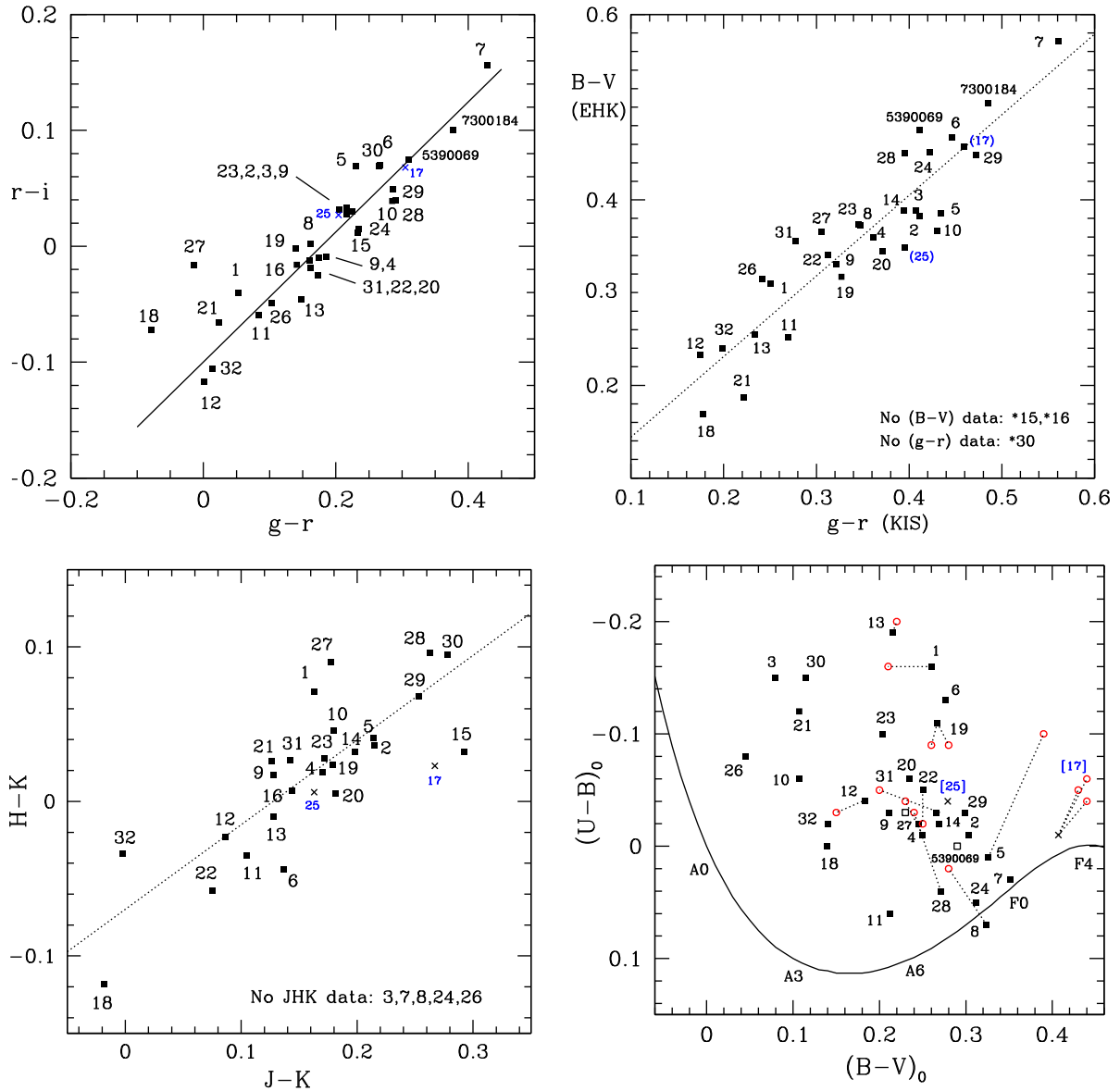


Figure 11. Two-colour diagrams for the candidate SX Phe stars. In each panel, the stars have been labelled with the CFHT star numbers, except the two stars too faint to have been observed spectroscopically that have been labelled with their KIC numbers. (Top left) Gunn-Thuan griz (SDSS) system two-colour diagram, $r-i$ versus $g-r$ (both from the KIC), for the candidate SX Phe stars. The equation of the line, $r-i = 0.5611(g-r) - 0.0998$, was derived excluding the two outliers, KIC 6227118 (*27) and KIC 12688835 (*18), and excluding the two misclassified non-SX Phe stars, KIC 12643589 (*17) and KIC 9535881 (*25). (Top right) Two-colour diagram for the candidate SX Phe stars, comparing the $B-V$ colours from Everett et al. (2012) with the $g-r$ colours given in the Greiss et al. (2012) Kepler-INT survey (KIS). The equation of the line, $B-V = 0.870(g-r) + 0.057$, with $R^2 = 0.85$, was derived after excluding the two misclassified stars, KIC 12643589 (*17) and KIC 9535881 (*25). For KIC 4662336 (*14), the KIC $g-r$ colour, 0.225, transformed to the KIS system using the relation $g-r(\text{KIS}) = 0.817g-r(\text{KIC}) + 0.199$, i.e. 0.383, rather than the too-red KIS colour, 0.584, was used. (Bottom left) Near-infrared (2MASS) two-colour diagram for the candidate SX Phe stars. The equation of the line is: $H-K = 0.5478(J-K) - 0.0698$, with $R^2 = 0.68$. (Bottom right) Reddening-corrected $(U-B)_0$ versus $(B-V)_0$ diagram. The adopted E_{B-V} reddening values are the new values given in Table 2 and the E_{U-B} reddening values were calculated using the relation $(U-B)_0 = (U-B) - 0.72E_{B-V}$. The curve is the standard relation for unreddened main-sequence stars; the solid black squares represent the Everett et al. (2012) photometry reddening-corrected with the new reddening values; and the red open circles correspond to the new Bohyunsan Observatory UVB photometric observations.

corresponding spectral types given along the curve. Also plotted for 11 of the programme stars are the new UVB colours based on photometric observations made in 2014 October with the 1.8-m Bohyunsan Observatory telescope (the magnitudes and colours are given in Table 5). The new colours agree well with the Everett et al. (2012) colours, the largest differences occurring, as one might expect, for the SB2 system KIC 6780873 (*5). Note that at a given

$(B-V)_0$ colour, the programme stars have $(U-B)_0$ colours that lie well above the main-sequence curve (but well below the blackbody curve that passes through the point $[(B-V)_0, (U-B)_0] = [+0.20, -0.68]$). As seen clearly in fig. 16 of Preston & Sneden (2000), there is, unfortunately, considerable overlap of curves of constant metal abundance and apparent age; as a consequence, the UV-excess is rendered ‘an ambiguous indicator of abundance’ in this situation.

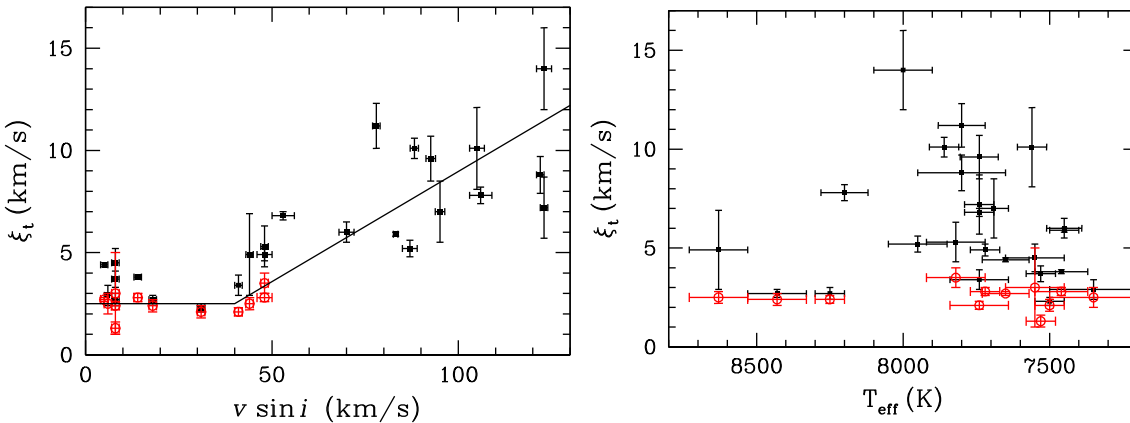


Figure 12. Microturbulent velocity ξ_t versus projected equatorial velocity $v \sin i$ (left) and versus SME effective temperature (right). The black filled squares are the SME values and the red open circles are vwa values. Both graphs exclude the four very rapidly rotating stars (i.e. those with $v \sin i > 190 \text{ km s}^{-1}$), the problematic star KIC 6227118 (*27) and the two misclassified stars.

2.5.2 Surface gravities

The surface gravities derived from the CFHT spectra are listed in column 4 of Table 4. When there are many overlapping echelle spectral orders, $\log g$ is not an easy parameter to measure (Smalley 2004; Catanzaro et al. 2011); therefore, and the derived values are not, in many cases, well-constrained. In Table 4, the values measured using SME are in the top row and vwa (or MOOG) values are in the row below; assumed or uncertain values are in enclosed parentheses. Also listed are the KIC and H14 gravities that were derived by matching observed photometric colours to stellar atmosphere models. All stars, except KIC 6227118 (*27) and KIC 7765585 (*28), have KIC and H14 values that are practically identical (note: the KIC does not give $\log g$ for KIC 11754974, but all other surface gravity derivations, including that by Murphy et al. (2013b), suggest a value close to 4.0). It is important to recall that Brown et al. (2011) warned against relying on the KIC estimates of $\log g$ for hot main-sequence stars, such as those being investigated here.

A comparison of the photometric and spectroscopic $\log g$ values shows that for all but the hottest stars, there is reasonably good agreement for the mean difference between the H14 and SME values being 0.05, with a standard deviation of the differences amounting to 0.29. For the hottest stars, the spectroscopic $\log g$ values tend to be significantly larger than the photometric values (which has the effect of increasing the derived temperatures and metal abundances). No attempt was made to constrain the spectroscopic $\log g$ values using the photometric values (see Torres et al. 2012).

The surface gravity of KIC 6227118 (*27) clearly is a problem. The KIC value, $\log g = 1.03$, is exceptionally small, resulting in an unrealistically high luminosity, $\log L/L_{\odot} \sim 4.0$. The revised gravity given by H14, $\log g = 2.84$, is higher but is still much smaller than expected for an SX Phe (or δ Sct) star. KIC 6227118 is an outlier in the top panel of Fig. 10 – presumably because it is an optical double (see footnote 1) and highly reddened (see Table 2). The gravity derived using SME, $\log g = 4.5 \pm 0.3$, is quite uncertain but is more consistent with the star being close to the main sequence.

Two stars for which the photometric and spectroscopic gravities differ significantly are KIC 5036493 (*26) and KIC 7174372 (*8). For KIC 5036493, the SME and vwa estimates of $\log g$ are both greater than $\log g = 4.3$, the expected value for an A5 zero-age main-sequence star and larger than the H14 photometric value of 3.97. The spectroscopic values for KIC 7174372 suggest that $\log g$

is closer to 3.5 (which is consistent with the A9 III spectral type) than the H14 value of 4.1.

In fig. 2 of BN12, two other stars appear to have low gravities (and therefore high luminosities since for stars of a given temperature $g \propto L^{-1}$): KIC 1162150 (*15) and KIC 9244992 (*7). Both stars are relatively cool and may represent stars that have evolved away from the main sequence. Although KIC 1162150 has a relatively bright neighbour to its north-west and an even closer faint blue star to its southeast, the spectroscopically and photometrically derived $\log g$ values are in close agreement and are near $\log g = 3.5$. In contrast, there was a lack of agreement between the spectroscopic and photometric estimates for KIC 9244992, the star studied in detail by Saio et al. (2015). The $\log g \sim 4.5$ derived assuming ionization balance differs by 1.0 from the SME and photometric values, which are all close to 3.5. For now, little can be said except that the value, $\log g = 4.0$, derived by Saio et al., lies mid-way between the SME and vwa spectroscopic estimates.

2.5.3 Microturbulent velocities

The concept of microturbulence was introduced by Struve & Elvey (1934) as a means of deriving, using the COG method, consistent chemical abundances from weak and strong spectral lines (see Gray 1988, 2005; Böhm-Vitense 1989; Landstreet et al. 2009; Aerts et al. 2014). Physically, the microturbulent velocity, ξ_t , is related to the mean free path of a photon through small convection cells. In practice, ξ_t accounts for excess (Gaussian) line broadening over and above that of thermal broadening.

For each of the programme stars, ξ_t was estimated using SME. For the 12 stars with the narrowest lines, estimates were also derived using vwa and MOOG (by adjusting ξ_t until the derived abundances were independent of EW). The resulting ξ_t values are given in column 7 of Table 4, where, for each star, the SME value is given in the first row and the vwa/MOOG value is in the second row.

Fig. 12 shows that there is a systematic difference between the SME and vwa microturbulent velocities, with the SME values (black filled squares) being $\sim 1-2 \text{ km s}^{-1}$ larger than the vwa values (red open circles), which are more in line with expectation for A-type stars. The left-hand panel shows that the broad line (more rapidly rotating) stars, for which only SME measurements were made, exhibit a significant trend of increasing ξ_t with increasing $v \sin i$. Whether

this trend is real, or a result of the increasing difficulty of measuring ξ_t as line blending increases, is uncertain. The right-hand panel shows that for the slow rotators, i.e. the stars with narrow lines and $v \sin i < 50 \text{ km s}^{-1}$ (red open circles), there is no apparent dependence of ξ_t on surface temperature.

How do these results compare with previous ξ_t measurements for similar stars? Gray (1988) discusses variations of microturbulence across the HR diagram and concludes that ‘there is no strong change in ξ with effective temperature within a given luminosity class’; for main-sequence stars, the adopted value for ξ_t was 1 km s^{-1} . More recently, Gray (2014) concludes from his analysis of five slowly rotating early-A stars that ‘an upper limit of $\lesssim 2 \text{ km s}^{-1}$ is placed on the microturbulence dispersion’. On the other hand, Landstreet (1998) found ξ_t values as large as 4.5 km s^{-1} in his analysis of later A-type stars. More recently, Landstreet et al. (2009) concluded (see their fig. 2) that ξ_t reaches a maximum of $\sim 4 \text{ km s}^{-1}$ near 8000 K, falling as temperatures increase or decrease, with the highest values occurring where chemical peculiarities (such as are seen in Am stars) are exhibited. Smalley’s (2004, fig. 4) graph shows a variation of ξ_t with T_{eff} , suggesting ξ_t values $\sim 3 \text{ km s}^{-1}$ for stars with temperatures in the range 7500–8300 K. Thus, while ξ_t values $\sim 4\text{--}5 \text{ km s}^{-1}$ are known for A-type stars from high-dispersion high SNR spectra, values as large as $10\text{--}15 \text{ km s}^{-1}$ (as derived here using SME) are unusually high, suggesting that they may be the result of difficulties in measuring ξ_t for fast rotators with broad and blended lines.

2.5.4 Metal abundances

The spectral synthesis method (as implemented in SME) was used to measure metal abundances for the programme stars. For those narrow-lined stars with unblended lines and reliable EWs, the COG method (as implemented in vwa and MOOG) was also used to measure [Fe/H]. Most of the measurements were made of co-added spectra, but when high SNR spectra were available, the abundance calculations were repeated using individual spectra and the results were folded into those from the co-added spectra. Unfortunately, our spectra were too noisy at near-UV wavelengths for reliable Ca II K-line EWs to be measured and used for [Fe/H] determinations (see Preston & Sneden 2000). The final derived abundances are given in the last column of Table 4.

The most metal-poor star in the BN12 sample is KIC 11754974 (*13), the 343 d TD binary (Murphy et al. 2013b). The mean abundance estimated from our spectra, $[Fe/H] = -1.2 \pm 0.3 \text{ dex}$, is lower than (but within the measurement error of) the abundance $-0.5 \pm 0.5 \text{ dex}$ reported by Murphy et al. that was based on lower dispersion spectra. Other low metal abundance stars include the narrow-lined star KIC 6520960 (*21) with $[Fe/H] = -0.8 \pm 0.2 \text{ dex}$ and KIC 8004558 (*1) with $[Fe/H] = -0.3 \pm 0.2 \text{ dex}$. All three stars are halo objects with retrograde galactic orbits and exhibit UV excesses in the bottom-right panel of Fig. 11 (see also fig. 1a of Preston et al. 1994). The other two stars on retrograde orbits, KIC 7174372 (*8) and KIC 10989032 (*32), are not metal-poor and do not show UV excesses.

Discrepancies between the SME and vwa/MOOG abundances are most likely due to the difficulties associated with line blending; the fact that our spectra have only moderate SNRs and the differences between the methods (e.g. SME includes several ‘metals’ in addition to iron in the various wavelength windows, whereas the vwa and MOOG analyses were restricted to iron lines). For those stars with broad lines, i.e. with $v \sin i$ between ~ 50 and 230 km s^{-1} ,

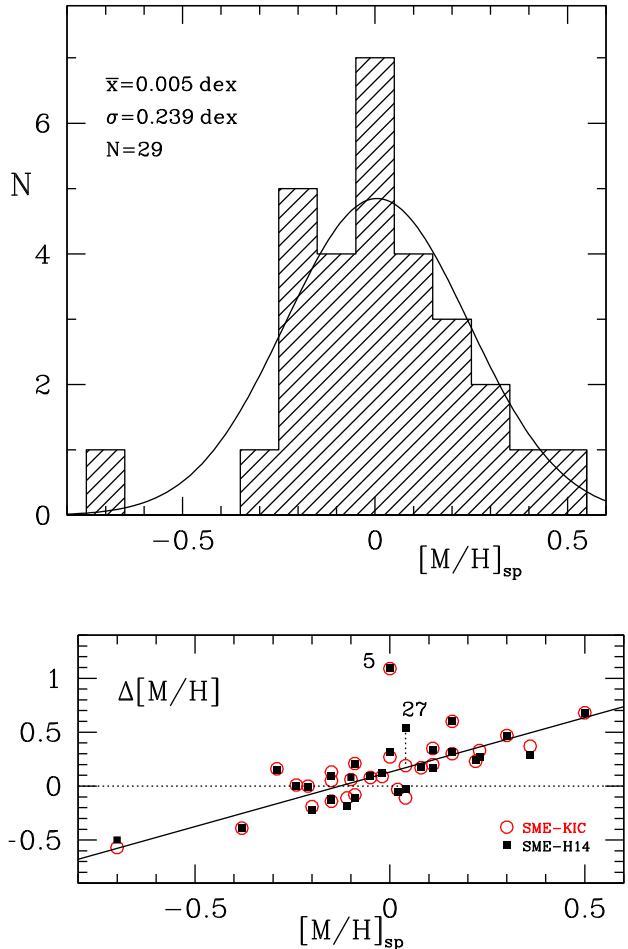


Figure 13. (Top panel) Histogram of spectroscopic metal abundances, $[M/H]_{\text{sp}}$, for 29 of the BN12 SX Phe candidates, fitted with a Gaussian of mean 0.005 dex and standard deviation 0.239 dex; note that KIC 11754974 is off-scale at $[M/H]_{\text{sp}} = -1.2 \pm 0.3 \text{ dex}$. (Bottom panel) Comparing the spectroscopic metallicities from SME and the photometry-based KIC (red circles) and H14 (black squares) metallicities, a well-defined linear trend is seen. The equation of the fitted line, after excluding the double-lined spectroscopic binary KIC 6780873 (*5), is $\Delta[M/H] = 0.949 [M/H]_{\text{sp}} + 0.127$, with $R^2 = 0.73$.

accurate measurement of [Fe/H] became increasingly difficult as $v \sin i$ increased. Given the size of the overall uncertainties, the small differences between [M/H] and [Fe/H] have been ignored.

The KIC and H14 photometric metal abundances tend to be within $\pm 0.10 \text{ dex}$ of each other. The largest difference (0.35 dex) occurs for KIC 6227118 (*27), the star identified earlier as an outlier with respect to other quantities. Excluding this star from the calculations, the mean difference between the KIC and H14 [Fe/H] values is 0.00 dex, with a standard deviation for the 31 stars of only 0.04 dex.

A histogram of the spectroscopic metallicities is shown in the upper panel of Fig. 13 and the spectroscopic and photometric metal abundances are compared in the lower panel. The differences, $\Delta[M/H]$, are in the sense ‘SME minus H14’ (solid black squares) and ‘SME minus KIC’ (open red circles). The observed trend implies that for metal-poor stars, the KIC/H14 abundances are more metal-rich than the spectroscopic abundances, and for the metal-rich stars, the KIC/H14 abundances are too metal-poor. For example, the KIC and H14 metallicities for KIC 3456605 (*24) are both -0.18 dex , compared with the SME value of $+0.50 \pm 0.10 \text{ dex}$;

and for KIC 11754974 (*13), the KIC metallicity is +0.01 dex, compared with the SME value of -1.1 ± 0.2 dex. The largest difference is for KIC 6780873 (*5), the newly discovered SB2 system discussed above. For it, both the KIC and H14 give -1.1 dex, compared with the SME metallicity 0.0 ± 0.3 dex and the vwa abundance $+0.16 \pm 0.20$ dex; no attempt was made to disentangle the spectral lines and so the uncertainties should be considered to be the minimum values.

3 KEPLER PHOTOMETRY

The *Kepler* photometry available at the time of the BN12 analysis comprised long-cadence (LC) data from quarters Q0 to Q5 and limited SC data for three stars: KIC 1162150 (Q4.3), KIC 9267042 (Q3.3) and KIC 11754974 (Q3.1). Since then, three additional years of LC photometry have become available, including two additional full quarters (Q6, Q7) of SC photometry for KIC 11754974; the latter have been analysed in detail by Murphy et al. (2013b) and Balona (2014b). BN12 give pulsation frequencies for the four stars that most closely resemble large-amplitude field SX Phe stars, as well as periodograms for the 10 stars located well above the Galactic plane.

Periodograms (also referred to as Fourier transforms ‘FTs’) based on the four years of available *Kepler* photometry (Q0–Q17) are presented below for all 34 candidate stars. Included are the two stars too faint to have been observed spectroscopically and the two close eclipsing binaries misclassified as candidate SX Phe stars. Pulsation frequencies, amplitudes and rotation periods have been derived from the periodograms and subsequently analysed. A significant result is the discovery of numerous binary systems and the derivation of their orbits.

3.1 Pulsations

Periodograms derived using the *Kepler* LC and SC photometry are shown in Figs 14 and 15, respectively. The frequency searches were made using the Lomb–Scargle algorithm (Press & Rybicki 1989). Six of the stars (KIC 4168579, 4662336, 4756040, 9966976, 11649497 and 11754974) were located on *Kepler*’s failed Module 3 and thus every fourth quarter is missing from the LC photometry. The gaps slightly altered the spectral windows but otherwise were not found to cause serious problems.

Another surmountable problem was the discrimination between ‘real’ and ‘alias’ peaks in the LC periodograms due to aliasing of pulsation frequencies higher than the LC Nyquist frequency at 24.462 d^{-1} (i.e. at half the sampling rate of ~ 49 photometric observations per day). The problem of identifying ‘super-Nyquist’ frequencies has been discussed by Murphy (2012), Murphy et al. (2013a), Chaplin et al. (2014) and others. For the three stars with SC photometry, such aliasing was not a problem owing to the high Nyquist frequency of the SC data, 734 d^{-1} (= half the sampling rate of 1468 points per day), and the fact that SX Phe and δ Sct stars have, in the past, been found to have maximum frequencies under 100 d^{-1} . The SC periodogram for KIC 9267042 clearly reveals a dominant real super-Nyquist frequency at 24.66 d^{-1} (responsible for the strong 24.26 d^{-1} alias peak seen in the LC periodogram).

For the majority of the stars, only LC photometry is available. To identify the super-Nyquist frequencies, searches from 0 to 50 d^{-1} were conducted using both Lomb–Scargle periodograms and the Fourier methods implemented in the PERIOD04 program of Lenz & Breger (2005). The criterion used to discriminate between real and alias frequencies was based on the assumption that the alias

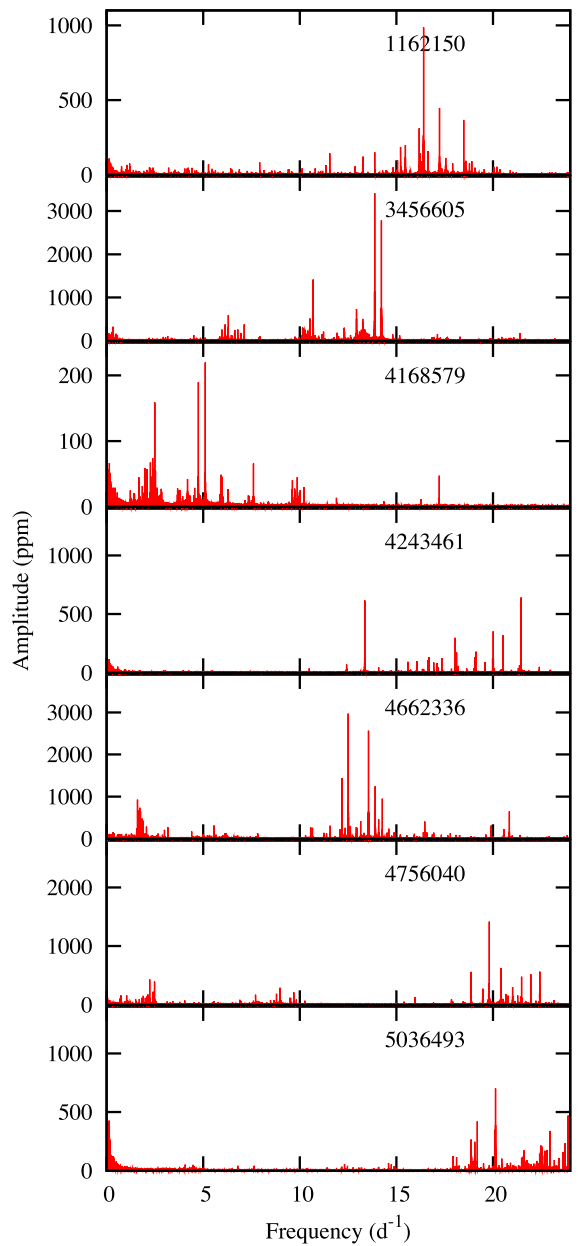
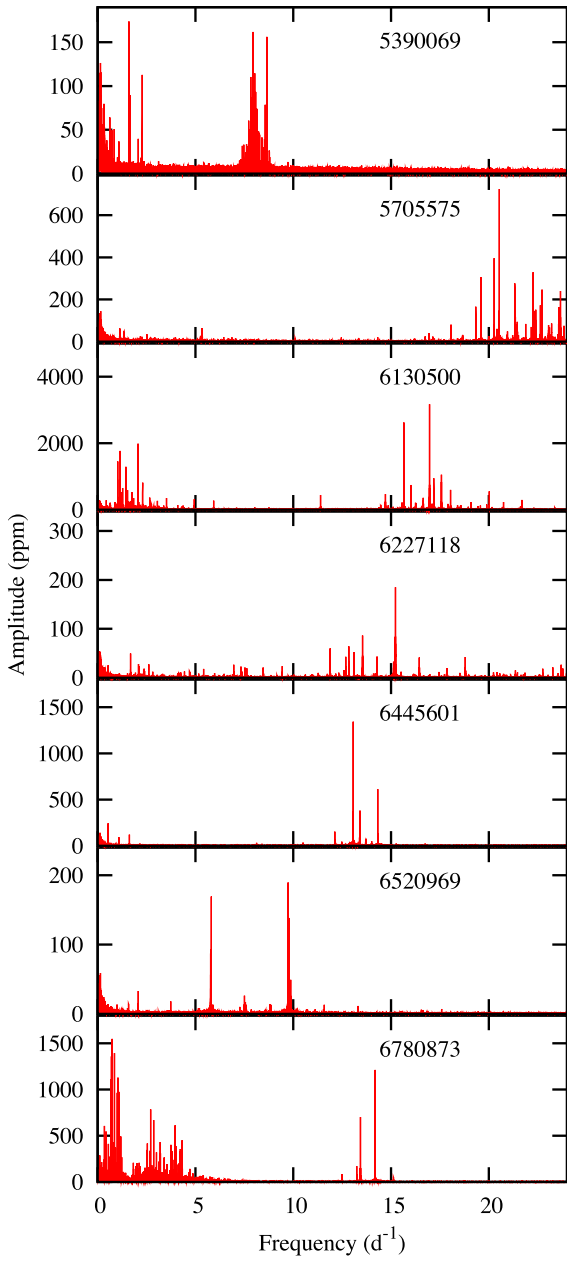


Figure 14. Periodograms for the 34 candidate SX Phe stars. The graphs are ordered by KIC number and the frequency maximum has been set to 24.46 d^{-1} , the Nyquist frequency of the *Kepler* LC data. The number of brightness measurements that were analysed usually amounted to $\sim 52\,000$ long-cadence points per star, sampled over $\sim 1470 \text{ d}$. Erratum: in fig. 3 of BN12, there are two panels with the label ‘11649497’; the lower label is correct and the upper label should have been ‘10989032’.

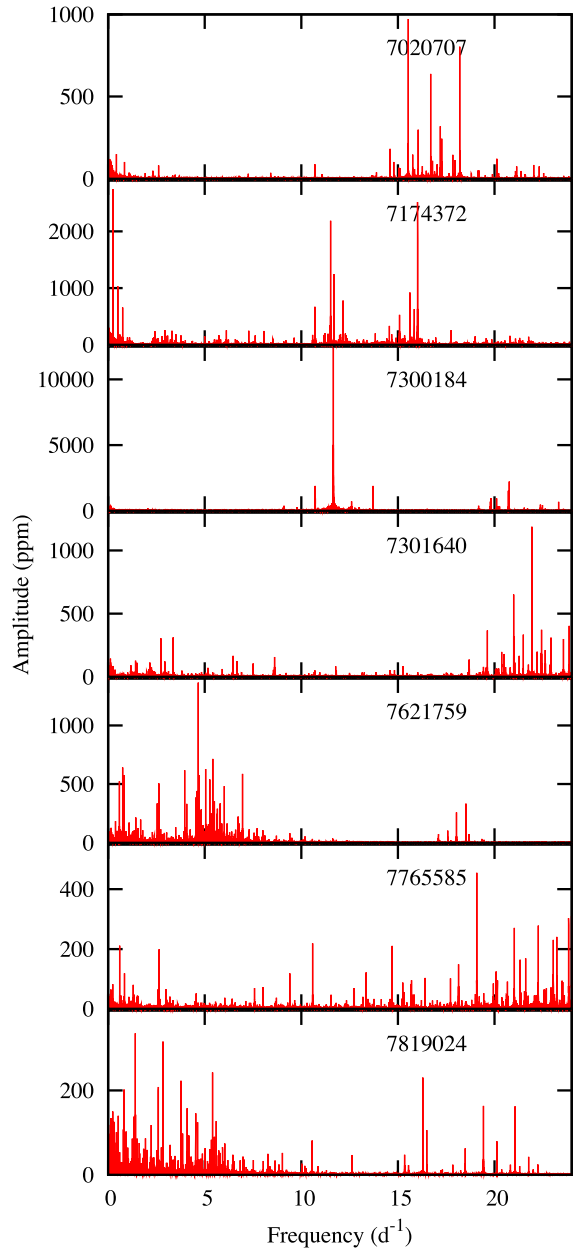
(which, for real super-Nyquist frequencies, occurs at twice the LC Nyquist frequency minus the real frequency) has a smaller peak amplitude than the corresponding real frequency. This classification rule appears to be borne out by the detailed analyses discussed in the references given above. By applying this rule, half of the programme stars were found to have super-Nyquist frequencies, with the highest dominant real frequency occurring at 54.7 d^{-1} (for KIC 6520969).

In Table 6, the pulsation frequencies, $v_n (\text{d}^{-1})$, and amplitudes, $A_n (\mu\text{mag})$, for the periodogram peaks with the largest amplitude and greatest significance are given for the programme stars. The numbers in the table are based on PERIOD04 analyses of the Q0–Q17 LC

Figure 14 – *continued*

(and any available SC) photometry. In general, the uncertainties in the frequencies are smaller than 10^{-5} d^{-1} , while the amplitude uncertainties depend on the method used to construct the periodogram and may amount to as much as 10 per cent.

CoRoT and *Kepler* observations have shown that most, if not all, δ Sct stars exhibit both low- and high-frequency pulsations (Balona 2014a). All 32 of the *Kepler*-field SX Phe candidates show frequencies $> 5 \text{ d}^{-1}$ (by definition) and ~ 25 of the stars also exhibit significant pulsation at low frequencies. Since most δ Sct stars are too hot to possess a significant outer convection zone, expectation was that the low frequencies are unlikely to be due to the convective blocking mechanism that is thought to drive the γ Dor pulsations seen at frequencies $0.3 < \nu_{\text{puls}} < 3.3 \text{ d}^{-1}$ (Guzik et al. 2000). However, the asteroseismic analysis of KIC 9244992 by Saio et al. (2015) showed that at least one of the stars exhibits rotationally split

Figure 14 – *continued*

core g-modes characteristic of γ Dor pulsators, as well as surface p-mode multiplets.

Detailed examination of the periodograms provides fundamental information about pulsation modes, a means for identifying binary systems (from TDs and phase modulations, PMs) and a framework for making inferences (which involves identification of rotationally split multiplets or light variations due to rotational modulation and the presence of possible starspots). A brief summary of the main findings for each star follows; many of the stars deserve a more detailed study.

KIC 1162150 (*15) – The strongest frequencies are between 15 and 20 d^{-1} , all of which are below the LC Nyquist frequency. The three highest peaks occur at 16.407, 17.232 and 18.490 d^{-1} and give rise

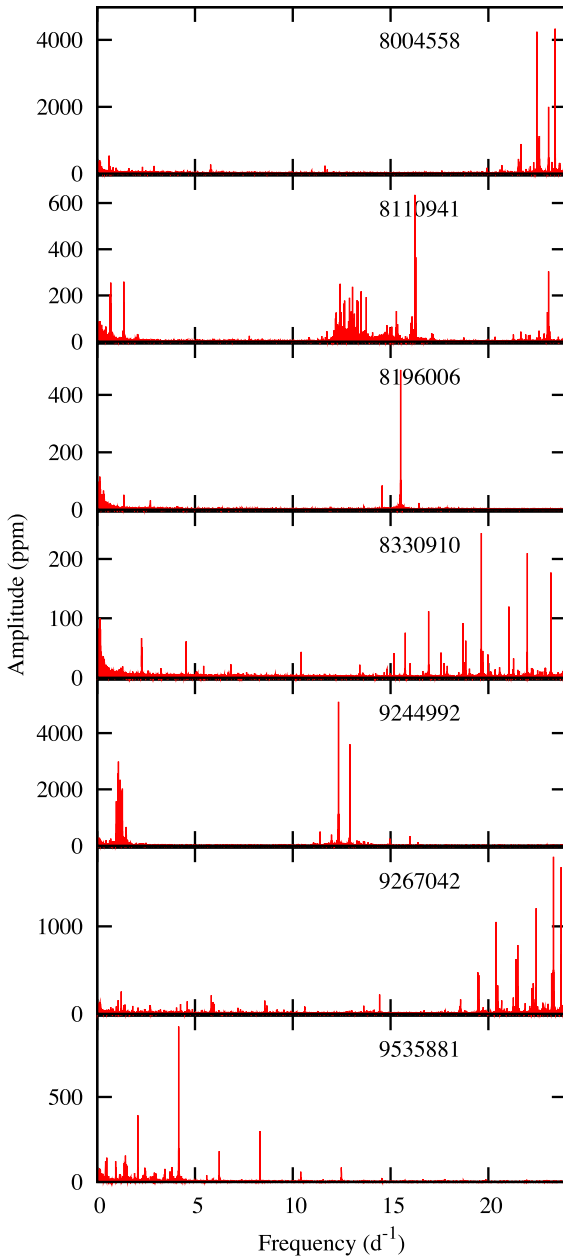


Figure 14 – continued

to a beat pattern of (variable) period $\sim 1.0\text{--}1.3$ d (best seen in the SC light curve).

KIC 3456605 (*24) – The two strongest peaks occur at 13.8771 and 14.2277 d^{-1} , with a third strong frequency at 10.6943 d^{-1} . Two of these, 10.6943 and 13.8771 d^{-1} , have a ratio 0.77 that might be the ratio of the fundamental to the first overtone radial mode (and therefore indicative of the star's mass). All the frequencies appear to be sub-Nyquist.

KIC 4168579 (*23) – The periodogram is dominated by low frequencies near 2.5 , 5.0 , 7.5 and 10 d^{-1} , and a distinct, but not very strong, p-mode frequency at 17.22 d^{-1} . Quite possibly, the former are harmonics (retrograde modes?) caused by the pulsator's rapid rotation ($<v \sin i > \sim 200$ km s^{-1}), in which case the rotation frequency is 2.49 d^{-1} . However, other modes also are possible (for example, see Breger et al. 2013). Also present at low frequencies

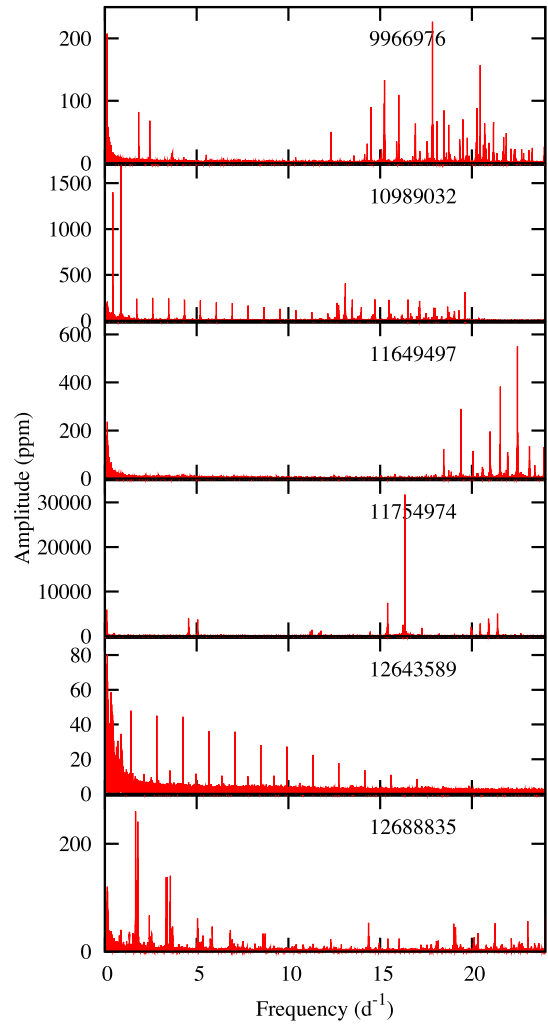


Figure 14 – continued

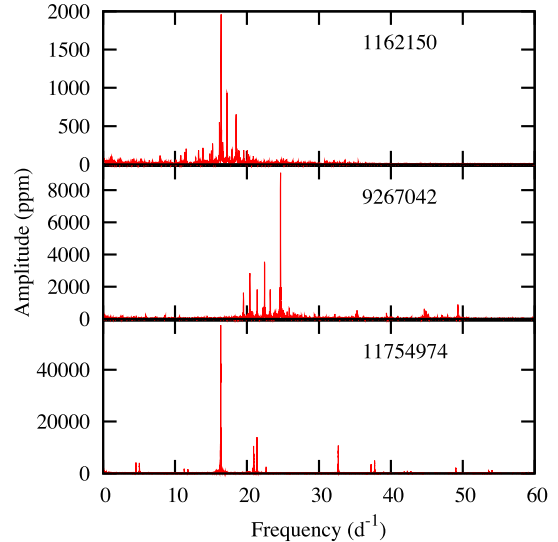


Figure 15. Periodograms derived from the short-cadence *Kepler* photometry for KIC 1162150 (*15, Q4.3, $\sim 42\,000$ points), KIC 9267042 (*12, Q3.3, $\sim 42\,000$ points) and KIC 11754974 (*13; Q3.1,Q6,Q7; $\sim 300\,000$ points). The maximum frequency of the graphs, 60 d^{-1} , is well below the 734 d^{-1} Nyquist frequency of the SC data.

Table 6. Pulsation frequencies, v_n (d^{-1}), and amplitudes, A_n ($\mu\text{mag} = \text{ppm}$), for the periodogram peaks of largest amplitude and greatest significance. The numbers are based on analysis of the short cadence data if available, otherwise of the Q0–Q17 long cadence data. When the amplitude of the super-Nyquist peak (at $v > 24.4615 d^{-1}$) was greater than that of the corresponding sub-Nyquist peak, the former was assumed to be the real frequency and the latter an alias frequency. Binary systems are identified with boldface KIC numbers and frequencies used in the TD analyses have been underlined and rotation (and/or orbital) frequencies are in red colour italics.

KIC (CFHT)	$v_1(A_1)$ $v_7(A_7)$	$v_2(A_2)$ $v_8(A_8)$	$v_3(A_3)$ $v_9(A_9)$	$v_4(A_4)$ $v_{10}(A_{10})$	$v_5(A_5)$ $v_{11}(A_{11})$	$v_6(A_6)$... etc.
1162150 (*15)	16.407 93 (1601)	17.231 22 (816)	18.490 44 (648)	16.400 05 (563)	16.183 82 (523)	15.221 77 (285)
3456605 (*24)	13.877 06 (4640)	14.227 73 (3559)	10.694 31 (1650)	13.872 17 (1167)	12.940 50 (789)	13.259 48 (721)
4168579 (*23)	5.109 53 (234)	4.746 23 (199)	<i>2.491 31</i> (165)	17.218 41 (75)	2.382 02 (79)	7.600 83 (73)
4243461 (*4)	21.458 19 (1300)	<u>13.361 51</u> (817)	<u>20.015 40</u> (650)	<u>18.045 97</u> (461)	<u>19.135 58</u> (306)	<u>18.115 25</u> (291)
	16.678 78 (209)	17.350 07 (208)				
4662336 (*14)	12.511 32 (4037)	13.554 32 (3428)	12.190 13 (1854)	13.907 94 (1672)	14.268 49 (1277)	20.844 69 (1249)
4756040 (*20)	19.807 61 (2566)	26.515 36 (1455)	20.410 56 (1183)	21.960 26 (1092)	2.234 50 (447)	20.678 29 (363)
5036493 (*26)	28.809 41 (1439)	23.896 70 (1164)	23.733 28 (568)	30.069 47 (531)	26.391 05 (535)	29.880 74 (502)
5390069	7.944 64 (183)	8.653 58 (181)	8.031 56 (143)	7.831 05 (130)	8.080 36 (112)	1.600 96 (186)
	2.273 98 (116)	1.662 93 (93)	0.1593 (40)	0.3187 (45)	0.4710 (48)	0.6220 (55)
5705575 (*22)	<u>20.535 86</u> (1387)	26.667 37 (872)	<u>20.278 54</u> (751)	25.277 48 (706)	25.362 01 (469)	22.395 38 (317)
	22.311 21 (317)	<u>21.356 56</u> (276)	<u>23.994 75</u> (211)	<u>24.784 04</u> (211)		
6130500 (*9)	16.969 20 (4988)	15.653 90 (3785)	17.191 23 (2164)	17.583 45 (1700)	17.191 23 (1396)	17.580 05 (1371)
	20.024 12 (1023)	18.040 89 (998)	21.695 12 (654)	16.651 37 (537)	11.398 45 (537)	2.070 24 (2005)
	<i>1.151 58</i> (1767)	1.021 88 (1413)	1.444 98 (1325)	1.116 45 (901)	2.297 61 (821)	1.275 16 (605)
6227118 (*27)	33.716 04 (304)	33.714 45 (159)	35.394 88 (134)	36.092 99 (99)	37.055 46 (88)	30.143 56 (85)
6445601 (*2)	13.067 92 (1696)	14.326 17 (838)	13.418 06 (487)	13.730 40 (108)	13.707 03 (93)	16.739 54 (49)
	10.507 16 (40)	8.128 04 (36)	1.624 31 (136)	1.082 96 (107)	<i>0.5416</i> (76)	
6520969 (*21)	39.195 36 (265)	54.748 94 (230)	39.152 03 (198)	39.064 51 (69)		
6780873 (*5)	<u>14.187 57</u> (1635)	<u>13.436 27</u> (912)	0.745 35 (1507)	0.702 28 (1360)	0.864 15 (1358)	0.670 20 (1154)
	1.040 91 (1077)	1.085 73 (945)	0.998 81 (947)	1.063 23 (919)		
7020707 (*16)	15.535 14 (1428)	18.203 83 (1332)	16.701 10 (986)	17.200 74 (496)	16.052 42 (454)	17.837 31 (244)
	17.961 63 (196)	16.789 14 (169)	22.026 07 (182)	22.312 78 (170)	21.150 35 (151)	17.035 94 (145)
	14.783 36 (141)	10.707 60 (105)	15.044 19 (100)	0.335 02 (153)	0.846 09 (97)	2.617 67 (87)
7174372 (*8)	16.021 62 (3692)	11.521 11 (2560)	11.683 48 (1601)	15.623 32 (1419)	12.157 87 (957)	15.843 35 (907)
	10.703 99 (823)	<i>0.2500</i> (2700)	0.5000 (1028)	0.7501 (642)		
7300184	<u>11.659 81</u> (28895)	20.766 54 (4324)	20.722 39 (2982)	13.712 37 (2524)	20.112 22 (1941)	23.319 61 (1637)
	22.481 31 (960)	0.253 25 (2081)	0.297 38 (1348)			
7301640 (*10)	21.936 07 (2483)	26.506 09 (977)	23.866 95 (1007)	23.571 56 (702)	19.632 72 (652)	26.726 37 (498)
	20.367 86 (373)	20.497 22 (339)	26.984 85 (286)	27.183 51 (250)	3.367 53 (317)	2.732 81 (311)
7621759 (*6)	4.669 61 (1487)	5.418 67 (741)	3.963 93 (693)	5.050 30 (685)	4.712 98 (616)	5.259 11 (572)
	18.519 80 (564)	6.014 97 (532)	2.620 24 (531)	0.836 35 (515)	0.749 07 (486)	18.035 28 (427)
7765585 (*28)	19.078 62 (873)	24.161 14 (765)	23.987 15 (622)	22.270 04 (609)	21.024 92 (552)	21.613 66 (353)
	14.705 50 (317)	10.581 27 (263)	23.535 83 (197)	20.151 50 (191)	2.642 22 (188)	0.843 29 (112)
7819024 (*19)	<u>16.290 36</u> (332)	<u>21.062 14</u> (315)	<u>19.427 95</u> (297)	<u>16.493 67</u> (158)	<u>21.765 67</u> (89)	<i>1.4066</i> (339)
	2.837 17 (322)	5.407 61 (252)	3.768 15 (228)	2.595 83 (214)	0.8252 (206)	
8004558 (*1)	<u>25.521 39</u> (11886)	24.915 83 (5381)	<u>26.329 43</u> (2689)	<u>25.685 62</u> (916)	<u>27.301 28</u> (864)	0.605 55 (604)
8110941 (*29)	16.240 03 (941)	24.919 33 (788)	16.294 38 (547)	12.419 64 (320)	13.060 36 (299)	23.959 00 (289)
	13.346 05 (285)	13.502 47 (283)	1.361 14 (265)	<i>0.687 93</i> (204)	1.376 57 (173)	0.642 87 (127)
8196006 (*30)	15.510 33 (701)	<i>1.359 86</i> (49)	2.721 24 (40)	4.080 92 (14)	5.443 20 (8)	
8330910 (*3)	24.141 47 (547)	21.992 15 (445)	19.639 65 (464)	16.943 67 (175)	15.755 56 (115)	18.842 84 (108)
	<i>2.2724</i> (69)	4.5513 (64)	6.8246 (24)			
9244992 (*7)	12.339 37 (6515)	12.920 06 (4642)	15.992 98 (502)	12.312 46 (495)	14.966 47 (359)	12.352 30 (313)
	1.091 00 (2987)	1.075 91 (2580)	1.158 51 (2265)	1.174 32 (2256)	1.211 47 (2046)	1.293 32 (2019)
9267042 (*12)	<u>24.6637</u> (9099)	<u>22.4487</u> (3617)	<u>20.4008</u> (2872)	23.2384 (1864)	<u>21.4236</u> (1800)	19.5155 (1650)
9535881 [*25]	2.081 52 (409)	4.163 01 (972)	6.244 52 (219)	8.326 02 (347)	10.407 54 (79)	12.489 03 (106)
	<i>0.488 85</i> (172)	0.423 86 (140)	0.946 85 (133)	1.449 71 (157)	1.381 11 (125)	1.487 14 (102)
9966976 (*31)	17.8582 (376)	20.4512 (302)	33.7040 (218)	30.4500 (165)	20.2785 (168)	16.0114 (165)
	0.1145 (197)	0.228 (50)	0.346 (40)	1.8407 (82)	2.4505 (71)	
10989032 (*32)	<i>0.433 82</i> (1415)	0.867 64 (1790)	29.319 30 (768)	35.831 61 (709)	32.421 00 (494)	33.450 78 (451)
	34.219 88 (449)	31.792 24 (466)	35.452 44 (404)	36.283 55 (334)	31.015 11 (258)	36.205 60 (249)
11649497 (*11)	22.489 21 (1161)	19.403 47 (495)	27.942 19 (384)	24.858 30 (340)	26.993 22 (263)	27.930 27 (207)
11754974 (*13)	<u>16.344 77</u> (67903)	<u>21.399 04</u> (14121)	<u>20.907 45</u> (10566)	<u>20.943 60</u> (7289)	<u>22.660 36</u> (2263)	
12643489 [*17]	0.070 80 (61)	0.128 17 (75)	0.333 54 (61)	0.338 68 (54)	0.708 23 (30)	0.884 63 (35)
	1.416 78 (48)	2.125 19 (10)	2.833 59 (46)	3.542 04 (13)	4.250 41 (46)	4.958 81 (12)
	5.667 22 (37)	6.375 65 (12)	7.084 01 (38)	7.792 39 (10)	8.500 86 (32)	9.209 22 (12)
12688835 (*18)	<i>1.674 30</i> (264)	1.787 84 (239)	1.782 63 (178)	3.5704 (100)	3.3798 (90)	3.3389 (85)
	5.0452 (40)	23.981 74 (178)	27.667 17 (111)	19.011 77 (79)	29.835 00 (78)	34.568 46 (72)

Table 7. KIC 4662336 (*14) – sequence of periodogram peaks around 1.7 d^{-1} , at frequencies $\nu_n (\text{d}^{-1})$ with amplitudes $A_n (\mu\text{mag})$, consecutive frequency spacings $\Delta\nu = \nu_{n+1} - \nu_n (\text{d}^{-1})$, periods $P_n (\text{day})$ and consecutive period spacings $\Delta P = P_n - P_{n+1} (\text{d}^{-1})$. Frequencies 1, 2, 4 appear to be aliases of 3, while 5, 7, 8 appear to be aliases of 6; and in general, the frequency spacings are increasing.

n	ν_n	A_n	$\Delta\nu$	P_n	ΔP
1	1.5486	197	0.0236	0.6457	0.0096
2	1.5722	275	0.0251	0.6361	0.0100
3	1.5973	957	0.0269	0.6261	0.0104
4	1.6242	192	–	0.6157	–
5	1.6843	702	0.0339	0.5937	0.0117
6	1.7181	754	0.0368	0.5820	0.0122
7	1.7550	643	0.0400	0.5698	0.0127
8	1.7950	401	0.0435	0.5571	0.0132
9	1.8385	494	0.0477	0.5439	0.0137
10	1.8861	425	–	0.5302	–

is an interesting group of peaks symmetric in spacing (and amplitude) at $\nu_1 = 5.872\,06$, $\nu_2 = 5.934\,02$, $\nu_3 = 5.969\,88$ and $\nu_4 = 6.031\,83 \text{ d}^{-1}$. While $\nu_4 - \nu_3 = \nu_2 - \nu_1 = 0.061\,95 \text{ d}^{-1}$, the meaning of this pattern is not clear. All the significant frequencies appear to be sub-Nyquist. Visual inspection of the periodogram gives the impression of equal spacing among some peaks, but closer study reveals that the spacings are not equal.

KIC 4243461 (*4) – Many peaks are present with frequencies higher than 13 d^{-1} and amplitudes in excess of 200 ppm. Frequency modulations also are seen. The peak of highest amplitude, at 21.458 d^{-1} , may be detectable from the ground. Also seen are a large number of frequencies below 4 d^{-1} , all with amplitudes less than 30 ppm; since the star is cool these are probably g modes. No evidence for spots is seen at low frequencies. The pulsator is in a TD binary system with a 460 d orbital period. In support of its binary nature, the observed RV range, $\Delta\text{RV} = 5.1 \text{ km s}^{-1}$, agrees well with the predicted $K_1 = 5 \text{ km s}^{-1}$.

KIC 4662336 (*14) – The frequencies of largest amplitude (above 500 μmag) are all sub-Nyquist and should be readily detectable from the ground. No obvious frequency modulation (FM) sidelobes are seen. A system of low-frequency peaks at around 1.7 d^{-1} (possibly g modes) is striking because of the almost equal spacing; the frequencies, periods and spacings are identified in Table 7. Although neither the frequencies nor the periods are equally spaced, the change in spacing forms a nice linear trend; similar such trends are seen in γ Dor stars (e.g. Bedding et al. 2015). Most of the peaks are concentrated in the range $10 < \nu < 22 \text{ d}^{-1}$, but there is no obvious pattern or common separation in this range.

KIC 4756040 (*20) – Shortward of the LC Nyquist frequency, the four highest amplitude peaks occur at 19.808 , 22.424 , 20.410 and 21.960 d^{-1} ; the second of these is an alias of the higher amplitude super-Nyquist frequency 26.515 d^{-1} . One also sees many low-amplitude peaks in the range $19\text{--}24 \text{ d}^{-1}$ and rich but low-amplitude peak systems in the frequency ranges $0.5\text{--}2.7$ (g modes?) and $7.3\text{--}10.0 \text{ d}^{-1}$. There are no apparent equidistant spacings. About half of the peaks between 15 and 24.4 d^{-1} are alias peaks and no frequencies of significant amplitude are seen above 35 d^{-1} .

KIC 5036493 (*26) – The $0\text{--}50 \text{ d}^{-1}$ LC periodogram is dominated by many peaks with frequencies between 18 and 31 d^{-1} and amplitudes in excess of 300 ppm; several of the super-Nyquist frequencies are real. The dominant real frequency is at 28.809 d^{-1} ,

with an alias at 20.130 d^{-1} . Low-amplitude peaks are seen in the range $12\text{--}15 \text{ d}^{-1}$, many of which have a spacing of 0.148 d^{-1} . There are very few peaks with $\nu < 5 \text{ d}^{-1}$, though there might be a long-term variation of $\nu = 0.135 \text{ d}^{-1}$ (similar to the frequency spacing just mentioned).

KIC 5390069 – The periodogram shows a clump of peaks between 7 and 9 d^{-1} and four prominent frequencies between 1.5 and 2.5 d^{-1} (at 1.601 , 1.663 , 2.081 and 2.274 d^{-1}), all of which have amplitudes smaller than 200 μmag . A series of equally spaced peaks seen at 0.1593 , 0.3187 , 0.4710 and 0.6220 d^{-1} may correspond to the rotation frequency and its harmonics, but the amplitudes increase with frequency.

KIC 5705575 (*22) – In the $0\text{--}50 \text{ d}^{-1}$ LC periodogram, nearly all the real peaks are located between 16 and 32 d^{-1} , some of which are super-Nyquist. Several low-amplitude peaks can be seen at low frequencies (5.3314 , 1.1367 , 1.3427 , 2.5202 d^{-1}), but there is no evidence for the rotation frequency (i.e. no harmonic peaks). TDs suggest an orbital period close to 538 d (see Section 3.3). The nine spectra taken at seven epochs clearly show RV variability ($\Delta\text{RV} \sim 17 \text{ km s}^{-1}$) consistent with the photometry and with the photometrically derived RV curve.

KIC 6130500 (*9) – The pulsation is dominated by several p-mode frequencies between 15 and 20 d^{-1} , in addition to a rich spectrum of g-mode frequencies between 1 and 4 d^{-1} . There are no obvious super-Nyquist frequencies, no FM sidelobes and no obvious spacings. Ground-based observations probably would classify this star as a hybrid as there are several peaks with amplitudes greater than 1 mmag.

KIC 6227118 (*27) – The dominant peaks, none of which have amplitudes exceeding $\sim 300 \mu\text{mag}$, are all above the LC Nyquist frequency and amplitude modulation is visible in the light curve. All the major peaks exhibit a similar multiplet structure, caused mainly by aliasing with the 372.5 d orbital period of the *Kepler* telescope. The dominant peak, at $\nu_1 = 33.7160 \text{ d}^{-1}$, is flanked by the second highest peak at $\nu_2 = 33.7145 \text{ d}^{-1}$. This is the only system in which almost all the power is beyond the LC Nyquist frequency.

KIC 6445601 (*2) – The periodogram is relatively simple, with high p-mode peaks at 13.07 , 14.33 and 13.42 d^{-1} , and several low-frequency equally spaced peaks corresponding to the rotation frequency 0.5415 d^{-1} (Neilson et al. 2013) and its harmonics at 1.083 , 1.624 , 2.166 d^{-1} . No FM sidelobes are seen, but there exists the possibility of amplitude variability.

KIC 6520969 (*21) – Two real super-Nyquist frequencies, at $\nu_1 = 39.195 \text{ d}^{-1}$ and $\nu_2 = 54.749 \text{ d}^{-1}$, both of which are single and well-defined, dominate the $0\text{--}60 \text{ d}^{-1}$ periodogram. The latter is greater than twice the LC Nyquist frequency (i.e. $> 48.92 \text{ d}^{-1}$). The high peaks at 5.812 and 9.74 d^{-1} (and at 43.126 and 58.68 d^{-1}) are aliases of ν_1 and ν_2 , respectively. Near the ν_1 peak are less significant single peaks at 39.1520 and 39.0645 d^{-1} . Other significant super-Nyquist frequencies include 41.44 and 51.01 d^{-1} . In the vicinity of 43.13 , 54.72 , 58.68 , 58.72 and 58.81 d^{-1} , one sees frequency quintuplets with separations of $\sim 0.0027 \text{ d}^{-1}$; the splittings most likely are due to aliasing with the 372.5 d orbital period of the *Kepler* telescope. Below 4 d^{-1} the dominant frequencies are at 0.99 , 1.53 , 1.58 , 2.07 and 3.73 d^{-1} and show no evidence of rotational harmonics.

KIC 6780873 (*5) – The periodogram shows only two prominent peaks in the δ Sct range, at 14.188 and 13.436 d^{-1} , and a very rich low-frequency spectrum with many dozens of peaks concentrated

around 0.20–1.25, 2.25–3.33 and 3.33–4.45 d⁻¹, with amplitudes in the range 300–1625 ppm. No obvious frequency spacings can be detected. Except for the two p-mode peaks, this star would be classified as a γ Dor star. In Section 2.1.2, the RV variations revealed that this star is a double-lined spectroscopic binary, consistent with a TD analysis of the Q0-Q17 LC photometry (Section 3.3) that reveals it to be a close binary system with an orbital period $P_{\text{orb}} = 9.16 \pm 0.03$ d.

KIC 7020707 (*16) – The dominant frequencies are between 15 and 20 d⁻¹. The three highest peaks, at 15.54, 18.20 and 16.70 d⁻¹, are real (i.e. not aliases) and show no evidence of multiplet structure. At low frequencies, a few peaks are seen (all with amplitudes less than 150 μmag), two of which appear to be $v_{\text{rot}} = 0.43$ d⁻¹ and its harmonic at 0.85 d⁻¹.

KIC 7174372 (*8) – The LC periodogram exhibits two sets of complex p-mode pulsations (near 12 d⁻¹ and 16 d⁻¹), a distinct triplet of high-SNR peaks at 0.25, 0.50 and 0.75 d⁻¹, and many low-amplitude peaks distributed over a wide range of frequencies. In the light curve, the 0.25 d⁻¹ peak shows up as broad dips every 4 d, which, if not fictitious, may correspond to the rotation period claimed by Nielsen et al. (2013), or may be due to 4-d orbital motion in a close ‘ellipsoidal’ binary (see Section 3). The multiperiodic pulsations all occur at amplitudes below 0.01 mag.

KIC 7300184 – The periodogram shows an extreme peak at 11.66 d⁻¹, the amplitude of which, 28 900 μmag , is exceeded only by the 57 690 μmag dominant peak for KIC 11754974. Features with smaller amplitudes (\sim 4300–2500 μmag) are seen at 20.76, 20.72 and 13.71 d⁻¹. Four other peaks are also seen at 20.11, 20.19, 20.27 and 20.35 d⁻¹, all of which are separated by \sim 0.08 d⁻¹. A binarogram analysis shows the SX Phe star to be in a wide binary system with an orbital period of 640 \pm 60 d.

KIC 7301640 (*10) – Most of the power is at frequencies between 19 and 28 d⁻¹, including super-Nyquist frequencies 26.51, 26.73, 27.18 and 27.89 d⁻¹. At low frequencies, there are many scattered low-amplitude peaks (<400 ppm), the highest amplitude being at 3.37 and 2.73 d⁻¹. There are no obvious FM sidelobes and there is no evidence for v_{rot} harmonics.

KIC 7621759 (*6) – The highest peak is at 4.67 d⁻¹ and most of the peaks in the periodogram are of low frequency, with hundreds of peaks having $v < 8$ d⁻¹ (g modes?). The high frequencies at 18.52 and 18.04 d⁻¹ are of intermediate amplitude. There are no obvious equal spacings and no obvious FM sidelobes.

KIC 7765585 (*28) – Many frequencies are present, with most of the power above 18 d⁻¹ and no evidence for super-Nyquist frequencies. A few low-frequency peaks with moderate amplitudes are present (0.5992, 2.6422 d⁻¹) along with many dozens of low-amplitude peaks. Although $v \sin i$ is large, there is no evidence at short frequencies for rotational harmonics.

KIC 7819024 (*19) – The 0–25 d⁻¹ LC periodogram shows several high-frequency peaks, almost all having amplitudes higher than their super-Nyquist counterparts. Much of the power is at frequencies below 6 d⁻¹, including significant peaks at 1.41 and 2.84 d⁻¹. Frequency modulations due to binary motion suggest $P_{\text{orb}} \sim 216$ d.

KIC 8004558 (*1) – All the highest peaks in the 0–50 d⁻¹ LC periodogram occur at super-Nyquist frequencies. A variable beat pattern is seen in the light curve, mainly due to the three strongest frequencies at 25.521, 24.916 and 26.329 d⁻¹. At frequencies below 4 d⁻¹, the greatest power occurs at 0.6056 d⁻¹. Several other g-mode

peaks between 0.6 and 3.0 d⁻¹ are seen, with no evidence for v_{rot} harmonics. This high-velocity star is a TD binary system with an orbital period of \sim 262 d.

KIC 8110941 (*29) – The 0–50 d⁻¹ LC periodogram reveals two well-resolved triplets, at 16.2400, 16.2943 and 16.1856 d⁻¹, and at 24.9193, 24.9800 and 24.8578 d⁻¹. The latter triplet is located beyond the LC Nyquist frequency and so alias peaks appear at 24.0197, 23.9590 and 24.0812 d⁻¹. One also sees a distinct set of many closely spaced peaks between 12.1 and 13.9 d⁻¹ and some scattered peaks at high frequencies. Below 3 d⁻¹, one sees two sets of peaks, at \sim 0.66 d⁻¹ and near 1.36 d⁻¹, where each set contains many closely spaced unresolved peaks within a band of about 0.06 d⁻¹. These correspond to the $v_{\text{rot}} = 0.6456$ d⁻¹ (and its harmonic) given in the Nielsen et al. (2013) catalogue. A possible third harmonic at 2.07 d⁻¹ is also weakly visible.

KIC 8196006 (*30) – Almost all the pulsation power is at 15.51 d⁻¹ with no evidence for g-mode frequencies. At low frequencies, four low-amplitude peaks dominate, three of which (at 2.72, 4.08 and 5.44 d⁻¹) are harmonics of the rotation frequency 1.360 d⁻¹ (Balona 2013).

KIC 8330910 (*3) – The six highest peaks in the 0–50 d⁻¹ LC periodogram all occur at frequencies below the LC Nyquist frequency. No obvious FM sidelobes are seen and, possibly, the amplitudes are variable. The spacing and amplitudes of the peaks at 2.2725, 4.551 and 6.825 d⁻¹ suggest that the first of these is the rotation frequency and the other two are its harmonics. Such a high v_{rot} is consistent with the high $\langle v \sin i \rangle = 224 \pm 3$ km s⁻¹.

KIC 9244992 (*7) – The 0–50 d⁻¹ frequency spectrum is dominated by two p-mode peaks at 12.339 and 12.920 d⁻¹, which, after pre-whitening, reveal a ‘plethora’ of p-mode peaks between 11 and 17 d⁻¹ and a complex high-amplitude group of g-mode peaks between 0.9 and 1.3 d⁻¹. A detailed asteroseismic analysis of the pulsations and an asteroseismic application of their use for determining physical characteristics, including the rotation profile, was made by Saio et al. (2015). Their best-fitting model was: $M = 1.45 M_{\odot}$; $T_{\text{eff}} = 6622$ K; $L = 7.14 L_{\odot}$; $R = 2.03 R_{\odot}$; $\log g = 3.982$; age = 1.9 Gyr; and (X,Y,Z) = (0.724, 0.266, 0.010), corresponding to [Fe/H] = -0.15 dex. No peak in the low-frequency periodogram at the well-established asteroseismic rotation frequency of 0.015 d⁻¹ is seen, perhaps suggesting an absence of spots or other surface features.

KIC 9267042 (*12) – The SC periodogram (middle panel of Fig. 15) reveals that all of the significant real p-mode frequencies are higher than 19 d⁻¹ and that the highest peak is super-Nyquist at $v_1 = 24.664$ d⁻¹. Thus, in the LC periodogram, the sub-Nyquist high-amplitude peak at 24.26 d⁻¹ is an alias. The next highest real peaks occur at 22.449 and 20.401 d⁻¹ and are mainly responsible for the complex beat pattern seen in the *Kepler* light curve. The peak amplitudes may be variable. TD analyses suggest that the pulsator may be in a binary (triple?) system with P_{orb} longer than the 4-d duration of the *Kepler* photometry (see Section 3.3).

KIC 9535881 [*25, KOI 4228] – This W UMa-type interacting binary system is one of the two mistakenly classified SX Phe candidates. Initially, it was flagged as a *Kepler* Object of Interest (KOI) but it is now considered to be a ‘false positive’. The Villanova EB catalogue lists it as having an orbital period of 0.480 4213 d and a mid-time for the primary eclipse of $\text{BJD}_0 = 2455002.248121$. In the periodogram, this period corresponds to the peaks at 2.0815 and 4.1630 d⁻¹, with additional harmonics of these at 6.244, 8.326,

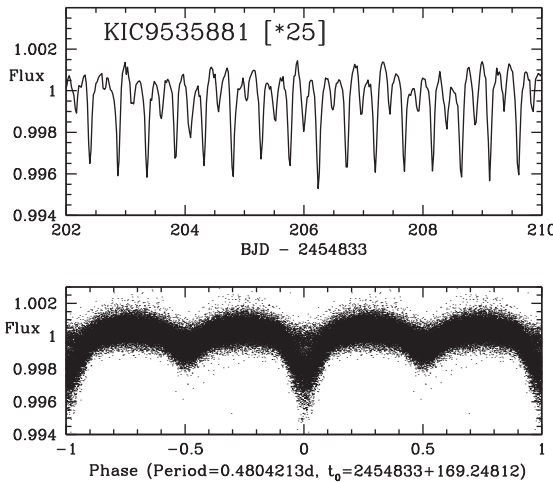


Figure 16. Light curves for the W UMa-type non-SX Phe binary KIC 9535881 [*25]. The top panel shows an 8-d portion of the light curve and the bottom panel shows all 63416 LC data points phased with the 0.48 d orbital period given in the Villanova EB catalogue.

10.407, 12.489, 14.571 and 16.652 d⁻¹. The primary and secondary minima both exhibit variable depths, shown in Fig. 16. At frequencies below 2 d⁻¹, several low-amplitude peaks are seen, possibly indicating that at least one component is a γ Dor variable or that $v_{\text{rot}} \sim 0.49$ d⁻¹ (i.e. $P_{\text{rot}} \sim 2.1$ d).

KIC 9966976 (*31) – The pulsations are of very low amplitude (<400 μmag), with most peaks occurring at frequencies higher than 12 d⁻¹, including real super-Nyquist frequencies at 33.704 and 30.450 d⁻¹ and a fairly sparse low-frequency spectrum. The strongest low- ν peak occurs at 0.1146 d⁻¹ (with harmonics at 0.228 and 0.346 d⁻¹), identified as v_{rot} by Balona (2013); all three peaks exhibit an underlying broad Gaussian feature somewhat similar to those seen in fig. 6 of Balona (2013). Additional low-frequency peaks are seen at 1.84 and 2.45 d⁻¹ (g modes?). Rømer TD analyses (see Section 3.3) suggest that the pulsator is in a binary system with an orbital period longer than 4 yr.

KIC 10989032 (*32, KOI 7397) – The *Kepler* light curve shows both eclipses and pulsations. These appear as two distinct sets of frequencies in the 0–25 d⁻¹ LC periodogram: (1) two high peaks associated with the 2.3 d orbital motion, one peak at $\nu_{\text{orb}} = 0.433$ 75 d⁻¹ and another at twice this, accompanied by a series of equally spaced harmonic peaks between 1.73 and \sim 12 d⁻¹ – the harmonics that are even multiples of ν_{orb} have much larger amplitudes than those at odd multiples of ν_{orb} ; and (2) a group of intermediate-amplitude pulsation peaks at frequencies between 12 and 20 d⁻¹, almost all of which are aliases of real p-mode pulsations at frequencies between 29 and 37 d⁻¹. As a KOI, it is characterized as a ‘false positive with a significant secondary event and a centroid offset’. The spectral type is based on an excellent match to the A5 V standard star HD 23194.

KIC 11649497 (*11) – Almost all of the significant real frequencies are above 15 d⁻¹, with many in the super-Nyquist region. All the major peaks show substructure due to aliasing caused by the orbital periods of *Kepler* and the Earth. ‘Low-amplitude eclipses’ were noted by BN12. The analysis is complicated by location on Module 3 and by amplitude modulation.

KIC 11754974 (*13) – Murphy et al. (2013b) discovered (from a careful asteroseismic investigation using the LC:Q0–Q13 and SC:Q6–Q7 data) that the SX Phe pulsator is in a 343-d non-eclipsing

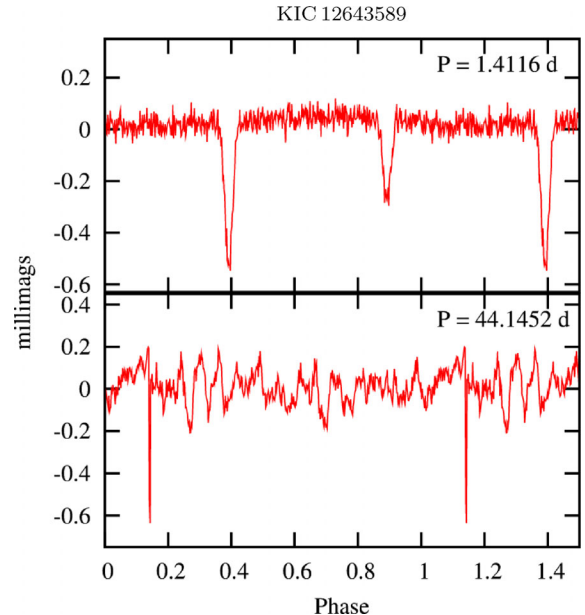


Figure 17. Light curves for the EB KIC 12643589 [*17], based on the *Kepler* Q1–17 LC photometry and phased with the orbital period 1.4116 d (upper panel) and with the 44.1452 d transit period (lower panel).

binary system. An independent pulsation and TD analysis using all the LC:Q0–17 data was later conducted by Balona (2014b). These studies identified five independent p-mode frequencies between 16 and 23 d⁻¹, the most powerful of which is at 16.344 75 d⁻¹. Also seen were many combination frequencies, including some very distinctive low-amplitude quintuplets. The strong peak at 0.095 24 d⁻¹ seen in the fig.13 binarogram of B14 is confirmed as fictitious; neither it nor the weaker peak at 16.24951 d⁻¹ (=16.344 75–0.095 24) is seen in the SC periodogram (see Fig. 15). No peaks are seen in the low-frequency LC or SC periodograms at the asteroseismic rotation frequency of 0.383 d⁻¹, perhaps suggesting the absence of spots or other surface features.

KIC 12643589 [*17, KOI 376] – This close binary (along with KIC 9535881) was mistakenly classified as an SX Phe star. The *Kepler* light curve plotted in Fig. 17 shows eclipses and transits that agree with the Villanova EB catalogue orbital periods of 1.411 6278 and 44.147 1769 d. As a KOI, it was identified as having two ‘false positive’ planet identifications. The well-defined harmonic series seen in Fig. 14 is due to the binarity; the harmonics with higher peaks are seen at even multiples of the orbital frequency, $\nu_{\text{orb}} = 0.70840$ d⁻¹, and those with lower peaks are seen at odd multiples of ν_{orb} . A secondary series of low-amplitude harmonics, equally spaced by an amount 0.022 65 d⁻¹ and caused by the transits, is seen in the periodogram out to \sim 6 d⁻¹. Two complex multipeaked gaussians of unknown origin are seen centred on 0.13 and 0.33 d⁻¹. No evidence for pulsations is seen.

KIC 12688835 (*18) – The periodogram is dominated by two sets of complex, relatively low-amplitude (\sim 150–250 μmag) peaks, at 1.67 and 1.78 d⁻¹, with possible harmonics (also complex) at 3.35 and 3.56 d⁻¹ and at 5.05 and 5.35 d⁻¹. If the harmonics are real and due to rotation, then $P_{\text{rot}} \sim 0.60$ d (Balona 2013). Differential rotation cannot be excluded. Concerning the pulsations, the low-frequency spectrum does not resemble that of a typical γ Dor star. Several of the strongest p-mode frequencies are in the super-Nyquist region.

3.2 Rotation

The *Kepler* data have proven to be useful for establishing surface and interior rotation periods for many stars across the HR diagram (see the review by Aerts 2015), including the two stars in our sample that were subjected to detailed asteroseismic investigations. For KIC 11754974 (*13), the inclination angle of the rotation axis ($= 47_{-15}^{+7}$ °), the equatorial rotation velocity ($= 34.18 \text{ km s}^{-1}$), and the radius ($= 1.764 R_{\odot}$) were determined by Murphy et al. (2013b). These values imply $\nu_{\text{rot}} = 0.383 \text{ d}^{-1}$ and $v \sin i = 25.0_{-6.9}^{+2.7} \text{ km s}^{-1}$, the latter being in close agreement with the mean projected rotation velocity measured from the spectra, $28.8 \pm 1.7 \text{ km s}^{-1}$. For KIC 9244992 (*7), the core and envelope rotation rates (both assumed to be constant) are available from Saio et al. (2015), who deduced from rotational splitting of its pulsation frequencies, a rotation period of $66.2 \pm 0.6 \text{ d}$ (i.e. $\nu_{\text{rot}} = 0.015 \text{ d}^{-1}$) at its surface and $63.9 \pm 0.2 \text{ d}$ at its core; such slow rotation corresponds to an equatorial rotation velocity of only 1.5 km s^{-1} , which is consistent with the measured $v \sin i < 7 \text{ km s}^{-1}$. Owing to the importance of rotation further such detailed investigations ought to be carried out.

Surface rotation frequencies have also been derived by examining low-frequency periodograms. If a star exhibits light variation due to the presence of a surface spot or other corotating surface feature, estimation of the rotation period may be possible. Light variations due to surface features are unlikely to be sinusoidal and therefore harmonics might be expected in the low-frequency periodogram. Thus, detection of a low-frequency peak and its harmonic(s) might reasonably be attributed to a revolving surface feature, in which case the rotation period of the star can be deduced (see Balona 2011; Balona & Dziembowski 2011). By identifying low-frequency peaks and their associated harmonics in *Kepler* periodograms, Balona (2013) derived rotation periods for 875 *Kepler* A-type stars, six of which are among the stars being considered here. Rotation periods for four other BN12 stars were similarly derived by Nielsen et al. (2013) as part of their programme to measure rotation periods for 12 000 *Kepler*-field main-sequence stars.⁸ Because the ν_{rot} range investigated by Nielsen et al. was limited to frequencies between 0.03 and 1.0 d^{-1} , none of the stars in their catalogue has a rotation period longer than 33 d or shorter than 1 d. Of course, other non-rotational interpretations of low-frequency peaks are possible, including that some or all of the low-frequency peaks have a pulsation origin and are combination frequencies (e.g. Kurtz et al. 2015), an interpretation favoured by SJM.

In Table 8, rotation rates from the papers by Balona (2013) and Nielsen et al. (2013) and from the two above-mentioned asteroseismic investigations have been summarized. Note that all of the rotation periods, except that for KIC 9244992, are shorter than 10 d, as might be expected for stars with spectral types earlier than $\sim F5$ (see fig. 2 of Nielsen et al. 2013).

A systematic search of the low-frequency periodograms of all the BN12 stars was conducted to identify low-frequency ‘peaks and harmonics’. For most of the stars, including KIC 11754974 and KIC 9244992, no obvious ν_{rot} harmonics’ were detected. However, possible rotation frequencies were identified for three previously unmeasured stars, KIC 7020707, KIC 8330910 and KIC 4168579, and for KIC 7819024, all fast rotators with $v \sin i$ values greater than 90 km s^{-1} ; these too are given in Table 8.

Table 8. Rotation rates for the programme SX Phe stars. Columns (2)–(4) contain the rotational frequency, ν_{rot} , the rotational period, P_{rot} , and a reference label, where **B13**, **N13**, **M13** and S15 represent Balona (2013); hereafter **B13**, Nielsen et al. (2013), Murphy et al. (2013b) and Saio et al. (2015), respectively. The last column contains the spectroscopically measured mean projected rotational velocity from Table 3. Boldface numbers identify binaries (see Section 3.3) and values followed by colons are considered uncertain.

KIC (CFHT)	ν_{rot} (d^{-1})	P_{rot} (d)	Ref.	$\langle v \sin i \rangle$ (km s^{-1})
(1)	(2)	(3)	(4)	(5)
9244992 (*7)	0.015	66.2	S15	$< 6.7 \pm 0.3$
9966976 (*31)	0.114	8.77	B13	123 ± 1
7174372 (*8)	0.2501	3.998	N13	41.6 ± 1.0
11754974 (*13)	0.383	2.61	M13	28.8 ± 1.7
7020707 (*16)	0.431	2.32	new	105 ± 2
10989032 (*32)	0.434	2.30	B13	45.0 ± 0.9
6445601 (*2)	0.5415	1.847	N13	71.3 ± 0.4
8110941 (*29)	0.6456	1.549	N13	$< 7.5 \pm 0.2$
7819024 (*19)	0.825:	1.21:	N13	95.1 ± 1.3
	1.407	0.711	new	95.1 ± 1.3
6130500 (*9)	1.152	0.87	B13	49.3 ± 1.1
8196006 (*30)	1.360	0.74	B13	92.6 ± 1.3
9267042 (*12)	1.360:	0.74:	B13	106 ± 3
12688835 (*18)	1.674	0.60	B13	230 ± 5
8330910 (*3)	2.273	0.44	new	224 ± 3
4168579 (*23)	2.491	0.40	new	197 ± 4

Low-frequency periodograms for 12 of the surveyed stars are plotted in Fig. 18. The locations of the highest peaks, all with high S/N ratios, usually correspond to the rotation frequency (or its harmonic) given by Balona or Nielsen et al. An exception is KIC 7819024 (*19). For it, the moderate-amplitude peak at the Nielsen et al. rotation frequency, 0.825 d^{-1} , shows no harmonic at 1.65 d^{-1} and thus 0.825 d^{-1} is probably spurious; on the other hand, large peaks at 1.41 and 2.84 d^{-1} suggest that ν_{rot} is 1.41 d^{-1} .

Another discrepancy was found for KIC 9267042 (*12). Below 3 d^{-1} , several significant, but low-amplitude peaks are seen, the strongest of which occur at 1.226 , 1.0737 , 1.3604 and 2.701 d^{-1} , where the last two correspond to the value $\nu_{\text{rot}} = 1.360 \text{ d}^{-1}$ suggested by Balona (2013) and its harmonic. Since the first two frequencies have significantly higher amplitudes, $\nu_{\text{rot}} = 1.360 \text{ d}^{-1}$ must be considered questionable.

Further inspection of the periodograms shows that only five stars (CFHT nos. 8, 16, 2, 30 and 3) exhibit single, well-defined peaks at the presumptive ν_{rot} , with lower amplitude harmonics at two (and sometimes three) times ν_{rot} . KIC 9966976 (*31) has a dominant peak at 0.114 d^{-1} , the ν_{rot} value given by Balona (2013), with apparent harmonics of lower amplitude at two and three times ν_{rot} , but the peaks are broad and made up of several distinct frequencies, possibly due to differential rotation in a spotted star or due to combination frequencies. Such groupings of two, three or more frequencies at the peaks and harmonics, rather than single frequencies, also are seen for CFHT nos. 29, 9, 12, 18 and 23 (Fig. 18).

Since $v \sin i = 2\pi R \sin i \nu_{\text{rot}}$, one might expect to observe a positive correlation between ν_{rot} and $v \sin i$, where the degree of correlation depends on the distributions of the unknown radii and unknown inclination angles of the stars. Fig. 19 is a plot of $v \sin i$ versus ν_{rot} for the stars in Table 8, where the location of any given point below, say, the $R = 2 R_{\odot}$ line, can be understood as arising from either a smaller radius or an inclination angle less than 90° or some combination of the two possibilities. For instance, the location of

⁸ Nielsen et al. (2013) assume that their sample stars are Sun-like with convective envelopes and spots due to dynamo-driven magnetic fields, a situation which may not apply to the radiative envelopes of SX Phe stars.

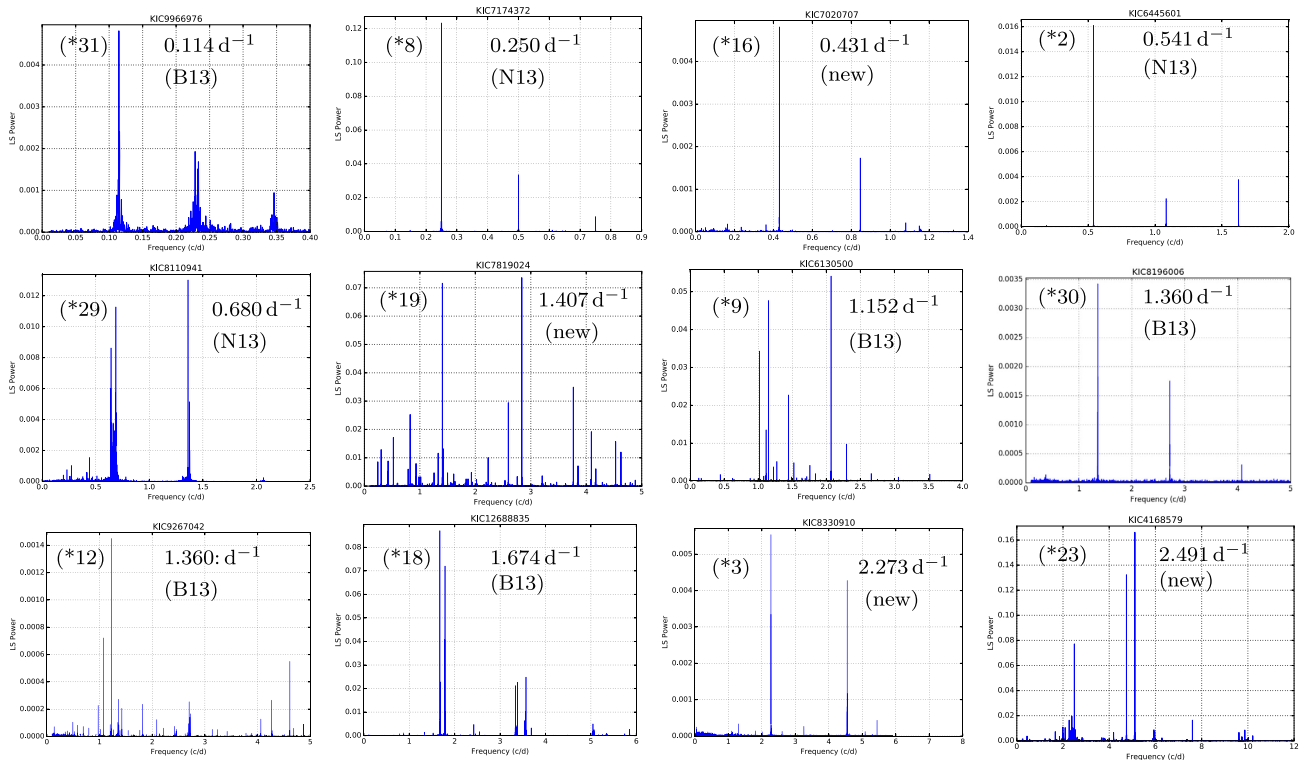


Figure 18. Peaks and possible harmonics seen at low frequencies in *Kepler* Q0–Q17 LC periodograms. KIC number (on top), CFHT star number (in parentheses), rotation frequency, ν_{rot} (rotations per day) and source of the rotation frequency (see Table 8), are noted in each panel.

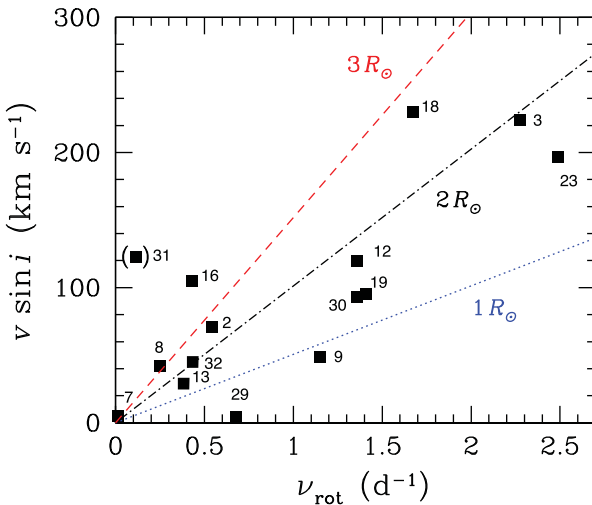


Figure 19. Projected rotational velocity as a function of rotational frequency for the SX Phe stars in the *Kepler* field (see Table 8). The three lines show the equatorial velocities (i.e. $v \sin i$ when $i = 90^\circ$) as a function of ν_{rot} for typical A-type stars having radii of $1 R_{\odot}$ (blue dotted line), $2 R_{\odot}$ (black dash-dotted line) and $3 R_{\odot}$ (red dashed line). The labels are the CFHT star numbers.

KIC 8110941 (*29), a narrow-lined star with $v \sin i < 7 \pm 1 \text{ km s}^{-1}$, is readily explained if its inclination angle is near 0° (i.e. it is observed pole-on). On the other hand, the estimated rotation frequency of KIC 9966976 (*31), $\nu_{\text{rot}} = 0.114 \text{ d}^{-1}$, is too low to account for a $v \sin i$ as large as the measured value, which suggests that the features seen in its low-frequency periodogram may not be attributable to a spot or other corotating feature, but could be an artefact at-

tributable to the long-term trends and jumps in *Kepler* photometry or due to combination frequencies (see Kurtz et al. 2015).

3.3 Binary systems

SX Phe stars are Pop.II BSs in the lower instability strip, and BSs are believed to be binary (or triple) systems that have experienced mass transfer or possibly coalescence (Hoyle 1964; McCrea 1964; Iben & Tutukov 1984; Iben 1986; Mateo et al. 1990; Nemec & Mateo 1990b; Bailyn 1995; Ferraro et al. 2006, Ferraro et al. 2015; Perets & Fabrycky 2009), from which it follows that SX Phe stars likewise have a binary (or triple star) nature. Of course, if coalescence has occurred, then the original binary nature may no longer be visible. In any case, since only a few SX Phe stars in binary systems are known (see Section 3.3.3), determination of the fraction of binaries among the BN12 stars and their properties is of considerable interest.

During the course of this investigation, 11 SX Phe binaries have been identified. Three of these stars are close binaries with orbital periods less than 10 d, and the other eight stars were discovered from Rømer TD analyses to be in wider binaries with orbital periods ~ 200 –1800 d. Orbital periods and other significant characteristics for the 11 SX Phe binaries are summarized in Table 9. The quantities recorded are: the orbital period, P_{orb} ; the half-range of the primary star's RV variation, K_1 ; the orbital eccentricity, e ; the argument of periastron, ω ; the time of periastron passage, T_{per} ; the projected semimajor axis of the primary, $a_1 \sin i$; and the mass function for the secondary star, $f_2(M_1, M_2, \sin i)$. Table 9 also gives the orbital characteristics for the two misclassified non-pulsating binaries: KIC 9535881 [*25] is a W UMa system with $P_{\text{orb}} = 0.4804$ d (and possible γ Dor pulsations); and KIC 12643589 [*17] is a triple

Table 9. Orbital elements for the *Kepler*-field SX Phe stars in binary systems, ordered by orbital period. The columns contain: (1) KIC and CFHT star numbers; (2) orbital period; (3) half-range of the RV variation of the primary star (i.e. the more massive SX Phe star); (4) projected semimajor axis of the orbit of the primary star; (5) orbital eccentricity; (6) argument of periastron; (7) time of periastron passage; and (8) mass function of the (less-massive) secondary star, f_2 . The last column indicates the source of the information in that row, where ‘TD’ stands for the TD (binarogram) method of Balona (2014b), ‘FM’ and ‘PM’ refer to the frequency and PM methods described by Shibahashi & Kurtz (2012) and Murphy et al. (2014), ‘EB’ refers to the Villanova EB catalogue and ‘RV’ refers to a ‘Spectroscopic Binary Solver’ (Johnson 2004) solution using the RVs in Table 1. Also given in the table are the previously published orbital elements for KIC 11754974 from Murphy et al. (2013b, hereafter ‘M13’) and from Balona (2014b, hereafter ‘B14’), and the results of simultaneously solving for the PMs given the observed RVs (‘PM+RV’).

KIC (CFHT) (1)	P_{orb} (d) (2)	K_1 (km s $^{-1}$) (3)	$a_1 \sin i$ (au) (4)	e (5)	ω ($^{\circ}$) (6)	T_{per} 2450000+ (7)	$f_2(M_1, M_2, i)$ (M $_{\odot}$) (8)	Method (9)
(a) Close binaries (orbital periods < 10 d)								
10989032 (*32)	(2.3050976) 2.3050976	18.3 ± 0.5	3.86×10^{-3}	0.08 ± 0.03	211 ± 15	6547.6 ± 0.1	$(1.45 \pm 0.18) \times 10^{-3}$	RV
7174372 (*8)	4.0 ± 0.1	1.3 ± 0.5	4.9×10^{-4}	0.0	undef.	undef.	$(9.5 \pm 0.1) \times 10^{-7}$	EB, RV
6780873 (*5)	9.1547 ± 0.0003 9.156 ± 0.046 9.16 ± 0.03 9.161 ± 0.001	$38.73 \pm .12$ 44.4 ± 6.0	$0.0325 \pm .0001$ 0.037 ± 0.005	$(5 \pm 5) \times 10^{-4}$	undef.	undef.	$(5.51 \pm 0.05) \times 10^{-2}$ $(8.0 \pm 3.0) \times 10^{-2}$ $(7.2 \pm 12.8) \times 10^{-2}$	PM+RV
						6531 ± 1	$(5.5 \pm 0.2) \times 10^{-2}$	TD
						6518.7 ± 0.3		FM
								RV
(b) Rømer time-delay (wide) binaries								
7819024 (*19)	216.6 ± 0.7 216.2 ± 3.9 216.2 ± 3.1	7.27 ± 0.43 7.37 ± 0.95	0.144 ± 0.007 0.147 ± 0.019	0.09 ± 0.08	299 ± 82	5050 ± 50	$(8.48 \pm 1.24) \times 10^{-3}$ $(8.96 \pm 3.42) \times 10^{-3}$ $(9.2 \pm 3.2) \times 10^{-3}$	PM+RV
8004558 (*1)	259.8 ± 0.2 262.1 ± 0.2 261.2 ± 0.9	9.70 ± 0.08 10.57 ± 0.08	0.231 ± 0.002 0.255 ± 0.002	0.020 ± 0.012	287 ± 11	4993 ± 8	$(2.45 \pm 0.06) \times 10^{-2}$ $(3.21 \pm 0.07) \times 10^{-2}$ $(2.83 \pm 0.04) \times 10^{-2}$	TD
11754974 (*13)	342.6 ± 0.5 344.8 ± 0.2 343.3 ± 0.3 343.1 ± 0.8	8.39 ± 0.08 8.19 ± 0.06 8.35 ± 0.04	0.264 ± 0.003 0.259 ± 0.002 0.263 ± 0.002	0.013 ± 0.012 0.01 ± 0.01	37 ± 8 102 ± 38	5110 ± 6 4999 ± 37	$(2.09 \pm 0.06) \times 10^{-2}$ $(1.96 \pm 0.04) \times 10^{-2}$ $(2.07 \pm 0.03) \times 10^{-2}$ $(2.06 \pm 0.07) \times 10^{-2}$	FM
4243461 (*4)	481.6 ± 1.8 488.8 ± 2.9 475.5 ± 6.2	5.29 ± 0.12 5.34 ± 0.28	0.233 ± 0.005 0.240 ± 0.013	0.045 ± 0.031	163 ± 36	5296 ± 48	$(7.35 \pm 0.41) \times 10^{-3}$ $(7.69 \pm 0.12) \times 10^{-3}$ $(8.17 \pm 1.09) \times 10^{-3}$	TD
5705575 (*22)	537.7 ± 0.9 537.2 ± 1.5 539.5 ± 4.1 (537.5)	6.70 ± 0.04 6.60 ± 0.18	0.331 ± 0.003 0.326 ± 0.009	0.018 ± 0.014	52 ± 10	5367 ± 16	$(1.68 \pm 0.04) \times 10^{-2}$ $(1.60 \pm 0.13) \times 10^{-2}$ $(1.57 \pm 0.09) \times 10^{-2}$	FM
								PM+RV
7300184	635 ± 20 640 ± 60	0.02 ± 0.02 0.07 ± 0.04	0.001 ± 0.001 0.004 ± 0.002	(0.0)	undef.	undef.	$(1.57 \pm 0.59) \times 10^{-2}$ $(3.2 \pm 3.2) \times 10^{-11}$ $(1.8 \pm 1.8) \times 10^{-8}$	PM
9966976 (*31)	>1500 1750 ± 100	0.62 ± 0.05 0.66 ± 0.08	0.088 ± 0.006 0.106 ± 0.011				$(3.8 \pm 1.0) \times 10^{-5}$ $(5.2 \pm 1.7) \times 10^{-5}$	TD
9267042 (*12)	$(>1500?)$ $1760 \pm 70?$	0.72 ± 0.02 0.70 ± 0.03	0.091 ± 0.003 0.113 ± 0.004				$(5.4 \pm 0.5) \times 10^{-5}$ $(6.3 \pm 0.6) \times 10^{-5}$	PM
								TD
(c) Close eclipsing binaries (Pop.II) that do not contain an SX Phe star								
9535881 [*25]	0.4804213	2.1 ± 0.2	9.2×10^{-5}	0.0	undef.	undef.	$(4.4 \pm 0.9) \times 10^{-7}$	EB, RV
12643589 [*17]	1.4116278 44.147177	1.7 ± 0.1	2.2×10^{-4}	0.0	undef.	undef.	$(7.0 \pm 1.0) \times 10^{-7}$	EB, RV
								EB

system consisting of a 1.41 d EB with additional transits every $P_{\text{orb}} = 44$ d (see bottom panel of Fig. 17). Both systems are of interest in their own right because they are binaries belonging to the galactic halo stellar population; however, we are concerned in this paper primarily with the SX Phe stars, so little more will be said about these two stars.

3.3.1 Close binaries

Based on the appearance of their light curves, their observed RV variations and their broad CCFs, it is clear that KIC 10989032 (*32), KIC 7174372 (*8) and KIC 6780873 (*5) have orbital periods less

than 10 d and small separations. Their orbital and other properties are discussed next.

KIC 10989032 (*32) – This eclipsing system is listed in the Villanova EB catalogue as having $P_{\text{orb}} = 2.305\,0976(35)$ d, and a ‘morphology classification parameter’, 0.53, indicating that it is probably semidetached (morph ~ 0.5 –0.7) but is close to being detached (morph $\lesssim 0.5$). Other basic characteristics include: mid-eclipse time for the primary eclipse, $\text{BJD}_0 = 2454966.705 \pm 0.013$; primary and secondary eclipse depths of 0.0095 and 0.0043 (i.e. very low amplitude grazing eclipses); primary and secondary phase widths of 0.025 and 0.034; and a separation in phase between the primary and secondary eclipses of 0.499, suggesting a near-circular orbit

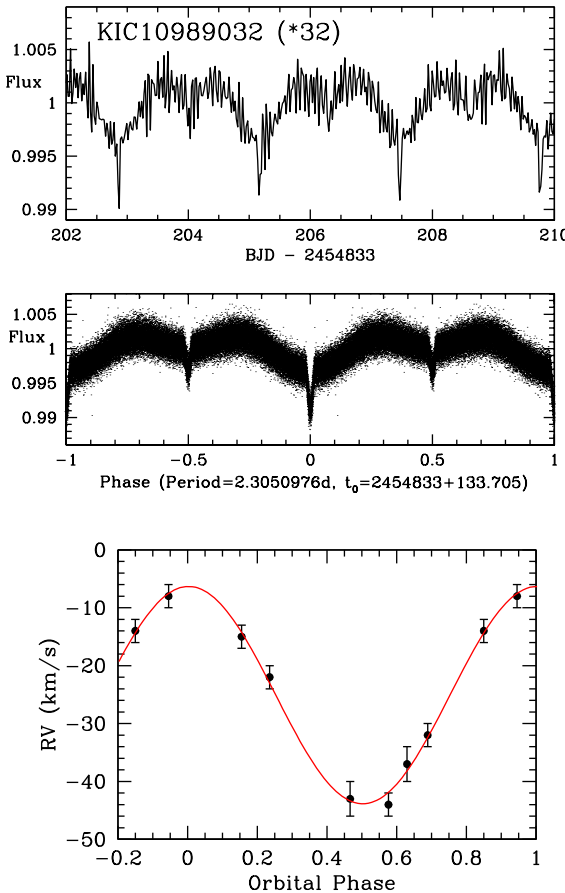


Figure 20. *Kepler* light curves (top, normalized LC fluxes) and RV curve (bottom) for KIC 10989032 (*32), phased with the 2.3-d orbital period and mid-eclipse time of the primary eclipse given in the Villanova EB catalogue. The fitted cosine curve is shown in red.

(unless the major axis of the orbital ellipse is orientated towards us, i.e. $\omega = \pm 90^\circ$). Additional parameters of the system include (see table 1 in Prša et al. 2011): temperature ratio, $T_2/T_1 = 0.454$; sum of the fractional radii, $(R_1 + R_2)/a = 0.208$ (where a is the semimajor axis of the orbit, equal to the separation of the two stars, $a_1 + a_2$); orbital inclination angle, $\sin i = 0.9947$ (i.e. nearly edge-on, $i = 84^\circ 10'$); and radial and tangential components of the orbital eccentricity, $e \sin \omega = -0.241$ and $e \cos \omega = 0.459$.

Fig. 20 shows an 8-d portion of the *Kepler* light curve (top panel), the LC fluxes phased with the Villanova P_{orb} and BJD_0 (middle panel) and the RV curve (bottom panel). The RVs are well fit with a cosine function. From the optimum RV fit, the eccentricity $e = 0.08 \pm 0.03$, with systemic velocity $\gamma = -24.96 \pm 0.31 \text{ km s}^{-1}$, RV amplitude $K_1 = 18.28 \pm 0.45 \text{ km s}^{-1}$, argument of periastron $\omega = 211^\circ \pm 16^\circ$ and time of periastron passage $2456\,547.61 \pm 0.09$. With these values, the mass function for the secondary, $f_2 = (M_2 \sin i)^3 / (M_1 + M_2)^2$, which can also be expressed as $P_{\text{orb}} K_1^3 (1 - e^2)^{3/2} / 2\pi G$, has the value $0.001\,45 \pm 0.000\,18 \text{ M}_\odot$; also, the projected semimajor axes, $a \sin i = 8.60$ and 0.83 R_\odot . Since $\sin i$ is so close to 1.0, this mass function is practically identical to the de-projected mass function, $f'_2 = 0.001\,49$, and the observed RV curve is practically identical to the curve that would be seen if the system were viewed edge-on. Combining the separation, $a = 8.65 \text{ R}_\odot$, with the sum of the fractional radii given above, implies $R_1 + R_2 = 1.8 \text{ R}_\odot$. From the cosine fit to the observed RVs, the time of maximum RV occurs at $\text{BJD} = 2456\,548.563 \pm 0.011$,

from which one can infer that eclipses occurred $\frac{1}{4} P_{\text{orb}}$ earlier and later, i.e. at $\text{BJD} 2456\,547.986$ and $2456\,549.139$, respectively. These ‘observed’ eclipse times are to be compared with the primary eclipse time predicted from the Villanova EB catalogue: $\text{BJD}_0 + 686P_{\text{orb}} = 2456\,548.002$, the time difference amounting to only 0.016 d or 23 min. This difference is much smaller than the error expected from the propagated uncertainties and is consistent with the observed lack of eclipse timing variations (see Conroy et al. 2014, and the online EB catalogue). Finally, with no RV information for the secondary, the mass ratio, q , and the individual masses are unknown. However, if the primary of KIC 10989032 were a typical A5 V star (see Table 3), it might be expected to have a mass $\sim 2.0 \text{ M}_\odot$ and a radius near 1.7 R_\odot (Gray 2005). Models of Pop. II BSs that have undergone mass transfer suggest lower total masses, possibly in the range $1.1\text{--}1.5 \text{ M}_\odot$ (see Fiorentino et al. 2014, 2015). Assuming 1.5 M_\odot for the mass of the primary, the observed $K_1 = 18.28 \text{ km s}^{-1}$ suggests $q = 0.11$ and a mass for the secondary of 0.16 M_\odot . The mass–radius relation of Demory et al. (2009) suggests that such a low-mass star might be expected to have a radius $R_2 \sim 0.15\text{--}0.20 \text{ R}_\odot$, consistent with the above discussion of sizes.

KIC 7174372 (*8) – As noted earlier, the *Kepler* light curve shows low-amplitude, high-frequency oscillations superimposed on periodic low-amplitude dips. It is possible that the 4-d period of the dips is due to rotation (Nielsen et al. 2013); however, the dips may also be due to orbital motion in an ellipsoidal binary system, i.e. a system comprising ‘non-eclipsing close binaries whose components are distorted by their mutual gravitation’ where ‘the light variations are due to the changing cross-sectional areas and surface luminosities that the distorted stars present to the observer at different phases’ (Morris 1985). The star is not listed in the Villanova EB catalogue. Owing to large uncertainties in the measured RVs (caused by the broad spectral lines), it is difficult to tell if the RVs are varying ($\Delta \text{RV} = 4.9 \pm 4.8 \text{ km s}^{-1}$); however, considerable broadening is seen in the CCFs (Fig. 5). If both P_{orb} and P_{rot} are near 4.0 d, then the system is tidally synchronized; such synchronization is common in binary systems with short orbital periods (Duquennoy & Mayor 1991).

KIC 6780873 (*5) – This double-lined spectroscopic binary (see Section 2.1) exhibits the largest RV range of all the programme stars, $\Delta \text{RV} = 69.9 \pm 0.3 \text{ km s}^{-1}$. Six of the nine CCFs resolve into two components, with heights that clearly identify the primary and secondary components (see Fig. 3). From an FM analysis, the orbital period was initially estimated to be 9.16 ± 0.03 d. Similar periods were derived from a TD binarogram analysis, a PM analysis (where a sampling window of 3 d instead of the usual 10 d was needed) and an analysis based only on the 18 RVs (using the ‘Spectroscopic Binary Solver’, sbs, program of Johnson 2004). The current best estimate of the orbital period, $P_{\text{orb}} = 9.1547 \pm 0.0003$ d, combines the results of the PM method with RV information (see Murphy, Shibahashi & Bedding 2016). With this period, the symmetric RV curves were well fit with eccentricity, $e = 0.0$, and gamma velocity (i.e. median RV), $\gamma = 10.07 \pm 0.26 \text{ km s}^{-1}$ (see Fig. 4). The observed amplitudes of the two RV curves, $K_1 = 38.8 \pm 0.9 \text{ km s}^{-1}$ and $K_2 = 52.4 \pm 1.0 \text{ km s}^{-1}$, give a mass ratio, $q = 0.74 \pm 0.03$, which is independent of the orbital inclination angle. The projected semimajor axis, $a \sin i = 16.48 \text{ R}_\odot (= 0.077 \text{ au})$, follows from $K_1 (P_{\text{orb}} / 2\pi) ((1+q)/q)$. Assuming the parameters given in the caption for Fig. 4, the predicted RV curves fit well the measured individual RVs, with standard deviations of the O–C residuals $\sim 0.62 \text{ km s}^{-1}$ for both components. Since the

Table 10. Example orbital properties for the non-eclipsing SB2 system KIC 6780873 (*5), for four possible primary-star masses. The quantities were calculated assuming the following observational constraints: $P_{\text{orb}} = 9.161 \pm 0.001$ d; $e = 0.04 \pm 0.02$; $a \sin i = 16.48$ R $_{\odot}$; $\gamma = 10.07 \pm 0.26$ km s $^{-1}$; $K_1 = 38.8 \pm 0.9$ km s $^{-1}$; $K_2 = 52.4 \pm 1.0$ km s $^{-1}$; $q = 0.74 \pm 0.03$; time of periastron passage, $T_{\text{per}} = 2455\,518.73 \pm 0.33$; argument of periastron for the primary and the secondary, $\omega_1 = 311^\circ \pm 14^\circ$ and $\omega_2 = 131^\circ \pm 14^\circ$. The velocities in the last two rows were calculated assuming circular orbits.

M ₁ =	0.9 M $_{\odot}$	1.2 M $_{\odot}$	1.5 M $_{\odot}$	1.8 M $_{\odot}$
M ₂ (M $_{\odot}$)	0.67	0.89	1.11	1.33
i ($^{\circ}$)	50.40	44.43	40.53	37.70
a (R $_{\odot}$)	21.39	23.56	25.38	26.97
a_1 (R $_{\odot}$)	9.10	10.02	10.79	11.47
a_2 (R $_{\odot}$)	12.29	13.54	14.59	15.50
v_1 (km s $^{-1}$)	50.3	55.4	59.6	63.4
v_2 (km s $^{-1}$)	67.9	74.8	80.6	85.7

photometry shows no evidence of eclipses, the individual masses and the orbital inclination angle, i , could not be determined; only the mass functions for the individual components, $f_1 = 0.136$ and $f_2 = 0.055$ M $_{\odot}$ could be estimated.

To resolve the degeneracy between mass and inclination angle, four different masses were assumed for the SX Phe (primary) star, M₁ = 0.9, 1.2, 1.5 and 1.8 M $_{\odot}$, and inclination angles were calculated by constraining the predicted RV curves to have the observed K_1 and K_2 values. Some properties of the binary system for the assumed masses are summarized in Table 10, where: M₂ follows from the observed mass ratio $q (=K_1/K_2)$; the semimajor axis, a , follows from Kepler's third law, $a^3 = G(M_1 + M_2)P^2/(4\pi^2)$; and the individual distances from the centre of mass, a_1 and a_2 , were computed from the a and K values. RV curves were computed for each mass, from which the best-fitting inclination angles, i , were found. Since e is near zero, the individual velocities, v_1 and v_2 , which follow from the a_1 , a_2 and P_{orb} values, are very nearly constant. Note that for a doubling of M₁, from 0.9 to 1.8 M $_{\odot}$, the inclination angle changed little, from 50 $^{\circ}$ 4 to 37 $^{\circ}$ 7.

3.3.2 Rømer time-delay (wide) binaries

Shibahashi & Kurtz (2012), Shibahashi et al. (2015), Telting et al. (2012), M13, Murphy et al. (2014, 2015, 2016), B14, Balona et al. (2015), Kurtz et al. (2015), Koen (2014) and others have shown that it is possible, using only *Kepler* time series photometry, to derive RV curves and orbital elements for binary systems in which one or more of the stars is pulsating. As the pulsating star orbits the barycentre of the binary system, its distance changes, resulting in Rømer TDs of the pulsation frequencies (also seen as PMs) that are equivalent to FMs. When working in the time domain, these methods have been variously referred to as the ‘TD’ method (Telting et al. 2012; B14), the ‘PM’ method (Murphy et al. 2014, 2016; Murphy & Shibahashi 2015), and the ‘O–C (and light travel time)’ method (Koen 2014); and in the frequency domain, the ‘FM’ method (Shibahashi & Kurtz 2012; Shibahashi et al. 2015). Successful application of these methods requires: (1) high-precision photometry (in order to derive accurate pulsation frequencies and to detect contamination by nearby frequencies); (2) photometry with a time baseline sufficiently long to resolve long orbital periods and sufficiently short to resolve close binaries with short orbital periods; and (3) one or more members of the binary system pulsating with one or more high-amplitude frequencies that are uncontaminated

by close frequencies (i.e. no significant neighbouring peaks in the periodogram) and which exhibit steady pulsation (i.e. no amplitude or intrinsic variations). The 32 SX Phe candidates and associated *Kepler* photometry meet all these requirements in the case of binary systems that have orbital periods in the range \sim 10 d to \sim 1700 d.

One prior application of the TD method was the detailed asteroseismic analysis of KIC 11754974 (*13) by M13. TDs of up to \sim 180 s revealed the SX Phe star to be the primary in a non-eclipsing 343 d binary system that has an almost circular orbit; assuming 1.5 M $_{\odot}$ for the mass of the primary and orbital inclination angle $i = 90^\circ$, gives a secondary mass of 0.6 ± 0.2 M $_{\odot}$, which is characteristic of a K- or early-M main-sequence star. More recent analyses of KIC 11754974 using the complete *Kepler* Q0–17 data set have been made by B14 and Murphy et al. (2014).

For this paper, both time- and frequency-domain methods were used to search the BN12 stars for SX Phe pulsators residing in binary systems. The analyses were carried out using the TD (binarogram) method described by B14 and the FM and PM methods described by Shibahashi & Kurtz (2012), Shibahashi et al. (2015), Murphy & Shibahashi (2015) and Murphy et al. (2014, 2016). All the available Q0–Q17 *Kepler* photometry was utilized, and for the time-domain analyses, a sampling interval of 10 d was adopted, which corresponds to a Nyquist frequency of 0.05 d $^{-1}$ and precludes measurement of orbital periods shorter than \sim 20 d. Care was taken to select only real frequencies with amplitudes high enough to allow the detection of binary motion (use of an incorrect alias frequency often results in an apparent ‘orbital period’ close to that of the *Kepler* satellite, i.e. 372 d). For the FM analyses, the short-period limit was reduced to \sim 4 d and led to the initial discovery of the 9.16 d orbital period for KIC 6780873 and the 4.0 d orbital period for KIC 7174372. Sensitivity to short periods is the biggest advantage that the frequency domain has over the time domain. Orbital elements derived from the current analysis are summarized in Table 9.

Observed phase shifts from the TD analyses are shown in Fig. 21 for six of the stars. The graphs for each star give, for the frequencies noted on the right-hand side of each graph, the phase variation as a function of orbital phase. The points in each graph represent the measured pulsation phase (10 d segments) of the photometry. The six stars have orbital periods between 208 and 670 d and therefore can be classified as ‘wide’ binaries. The high S/N of the phase variations leave little doubt about the binary nature for five of the six stars. In the case of KIC 7300184, only one pulsation frequency was employed in the analysis, therefore the orbital parameters e , ω and T_{per} could not be calculated.

In Fig. 22, TD diagrams and FTs of the weighted average TDs from PM analyses are plotted for seven of the wide binaries. The panels are ordered by orbital period, shortest at the top and longest at the bottom. For each TD graph (left-hand side), individual extracted frequencies that were used for the analysis are plotted with different symbols (see the legend on right). For all but the two longest period binaries, the null hypothesis that there is no TD can be ruled out with considerable confidence. The panel for KIC 11754974 (third row from the top) shows that dominant pulsation frequencies do not always lead to the same TD (or PM) curve. In some cases, the chosen pulsation frequencies may have been contaminated by other close frequency peaks, which would have had the effect of perturbing the phases at the sampling times and obscuring the frequency variation due to binarity; by analysing multiple frequencies, this problem was largely overcome.

The derived orbital periods for KIC 9267042 (*12) and KIC 9966976 (*31), if real, are longer than the \sim 4-yr duration

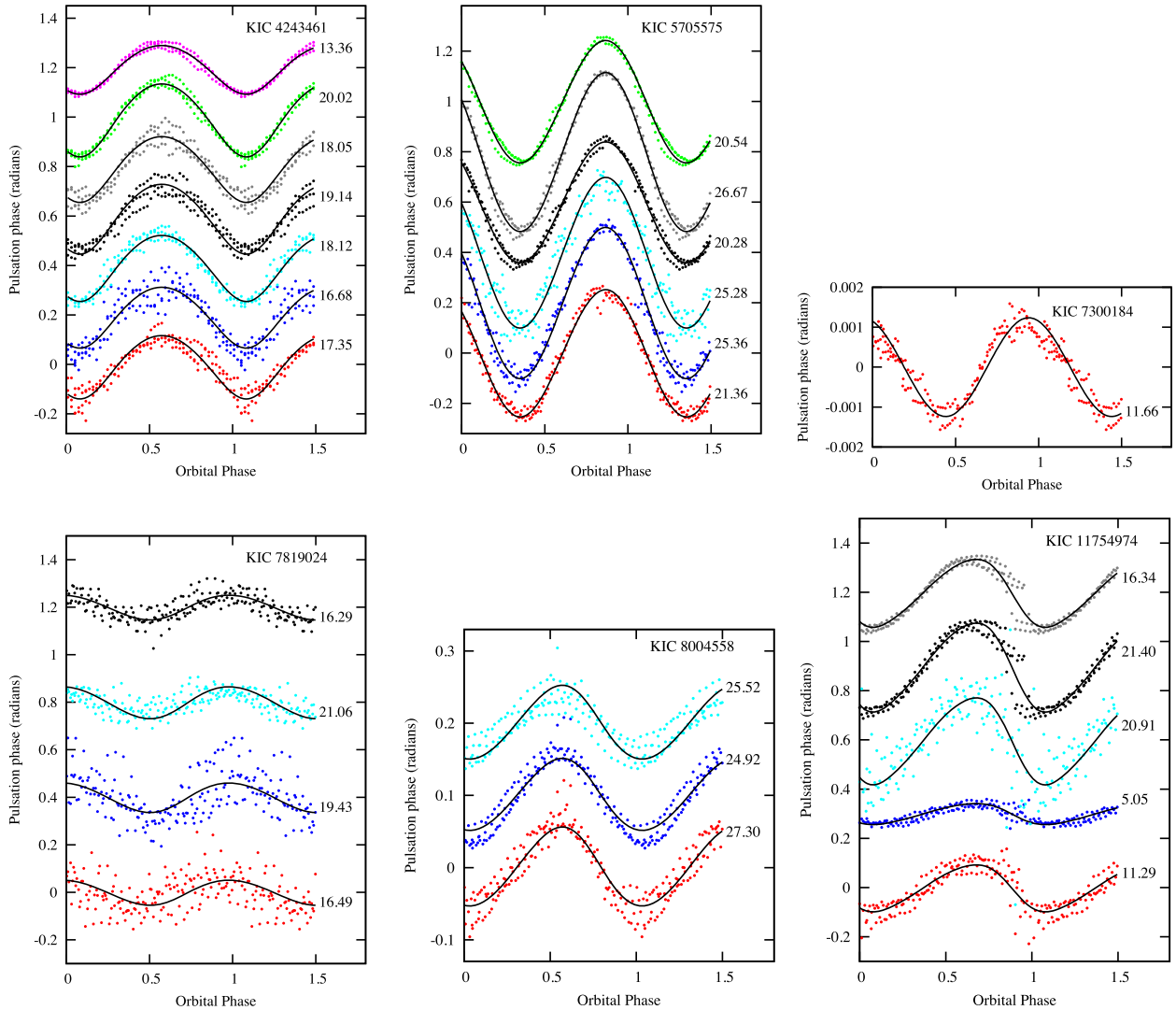


Figure 21. TD results for six binary stars: phase variation of the pulsation modes as a function of the orbital phase. For clarity, an arbitrary vertical displacement has been made (and different colour used) for each pulsation frequency and the particular frequency (units of d^{-1}) is given on the right. For KIC 7300184, the periodogram shows only one pulsation frequency of sufficiently high amplitude to reveal possible pulsation phase variations. The solid (black) curves are the fitted phase variations assuming the orbital parameters given in Table 10.

of the *Kepler* data set and are too long to be resolved by the FM method. However, phase variations indicative of binarity were found using both the PM and TD methods (see Table 9). The strongest argument that can be made for the reality of the measured TDs is that in Fig. 22, similar curvatures can be seen for all of the pulsation frequencies employed for the analyses, a finding that is consistent with variation caused by binary motion. When KIC 9966976 was analysed using the binarogram method, the same P_{orb} was found for the four frequencies that were considered and similar values of $a \sin i$ were derived for all four frequencies, which lends considerable support to the conclusion of its binary nature. The evidence was less convincing for KIC 92670423; while the same dominant peak (i.e. P_{orb}) was found for the four test frequencies, a range was seen in the amplitudes of the associated peaks (i.e. $a \sin i$), thereby reducing the likelihood of the binary conclusion.

Fig. 23 shows the results of PM+RV analyses for six TD binaries where both the PMs and the RVs were included in the orbit solutions. The graphs were created using the method outlined in Murphy et al. (2016). Inclusion of the RVs extended the time baselines by

almost 2 yr and added weight to several of the orbital solutions. The biggest improvement compared to the single-method results was for KIC 6780873 (*5), the 9.1 d double-lined spectroscopic binary; in this case, the precision of the orbital period improved to a few tens of seconds for a light travel time (across the orbit) of only a few tens of milliseconds, and the uncertainty of its orbital eccentricity improved to within 0.0005 of zero (signifying circular orbits). For the binaries with large $v \sin i$ values, the addition of the RVs to the solutions resulted in minimal improvement over the PM-only solutions; and for KIC 11754974 (*13), the maximum TD is now seen to be ~ 140 s, down from the ~ 180 s noted earlier.

Masses and radii for the programme stars, taken from H14, are given in Table 11. The average mass, $1.70 M_{\odot}$, and average radius, $2.25 R_{\odot}$ (excluding the extreme outlier KIC 6227118), were adopted for the two stars that are missing from the Huber et al. sample, KIC 5390069 and KIC 7300184. For the binary systems, lower limits for the masses of the secondary stars are also in the table. These were derived by assuming an orbital inclination angle, $i = 90^\circ$ (i.e. edge-on), adopting the Huber et al. mass for the

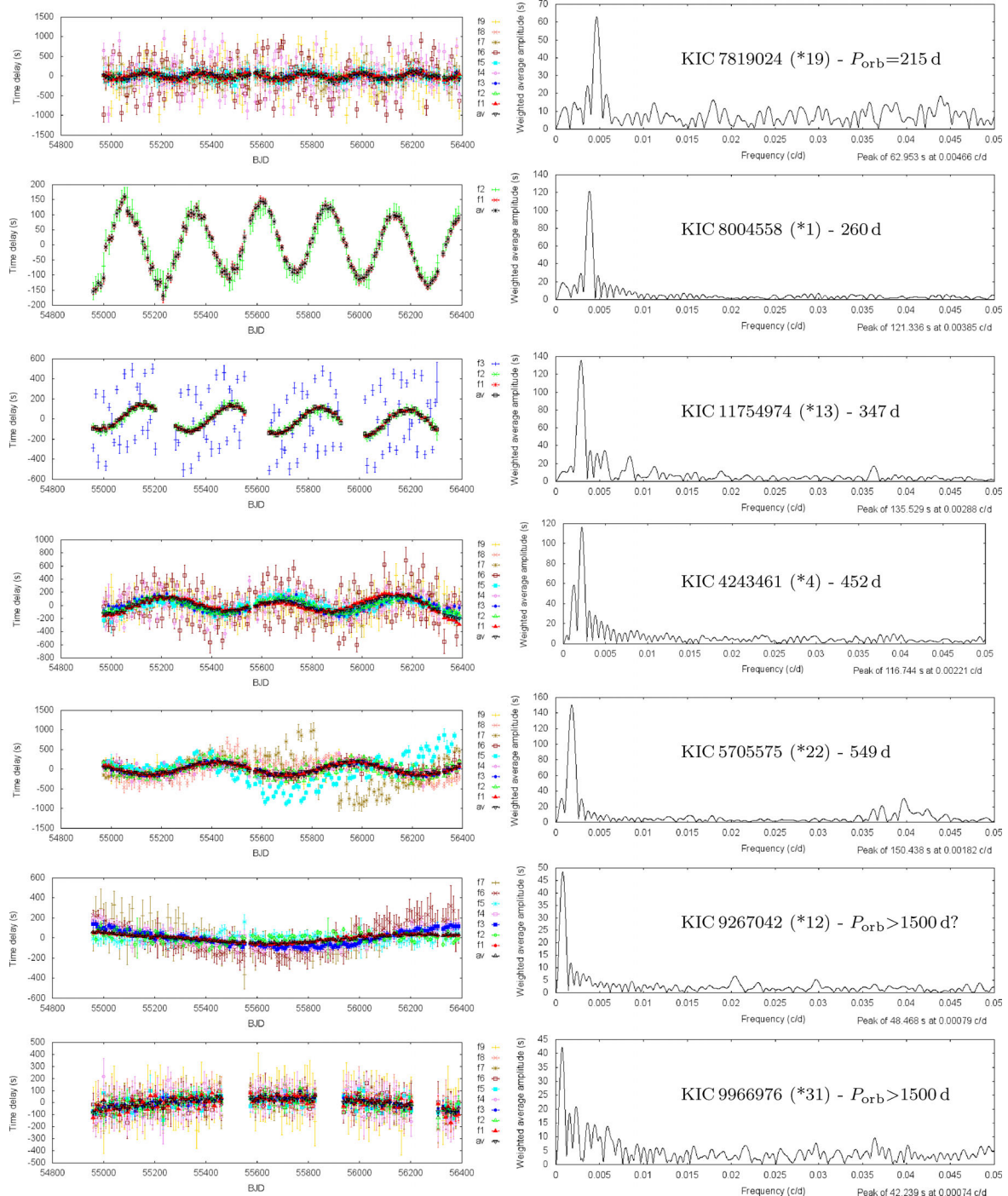


Figure 22. Phase Modulation (PM) analysis results: Time Delay (TD) diagrams (left) and Fourier Transforms (FTs) of the weighted average TDs (right) for six of the photometric binary systems, including the two long-period stars. The ordering (top to bottom) is by increasing orbital period. For each star, the weighted-average TDs are shown with black symbols (inverted open triangles).

primary star and using the mass function $f_2(M_1, M_2, \sin i)$ given in Table 9 to solve for the minimum mass of the secondary. Assuming $1.5 M_\odot$ for the KIC 11754974 primary star mass, instead of the H14 value of $1.73 M_\odot$, gives a slightly lower minimum mass for the secondary, $0.43 \pm 0.15 M_\odot$, still characteristic of a K- or early-M main-sequence star. The secondaries for KIC 7174372 (*8), KIC 9267042 (*12) and KIC 9966976 (*31) are seen to have M_2 lower limits below $0.08 M_\odot$, which offers the possibility that the companions are brown dwarfs.

Based on our findings, eight of the SX Phe stars appear to have companions with orbital periods between 200 and 1800 d, seven of which are new discoveries (the binarity of KIC 11754974 having already been discovered by M13). The orbits for these stars are probably too large for there to have been the mass transfer necessary to create the SX Phe primary (i.e. a pulsating BS). Of course, if one star already entered the red giant phase, it could now exist as an extreme horizontal branch star with an exposed core, i.e. an sdB or WD star. It seems most likely that the primary of these ‘wide’

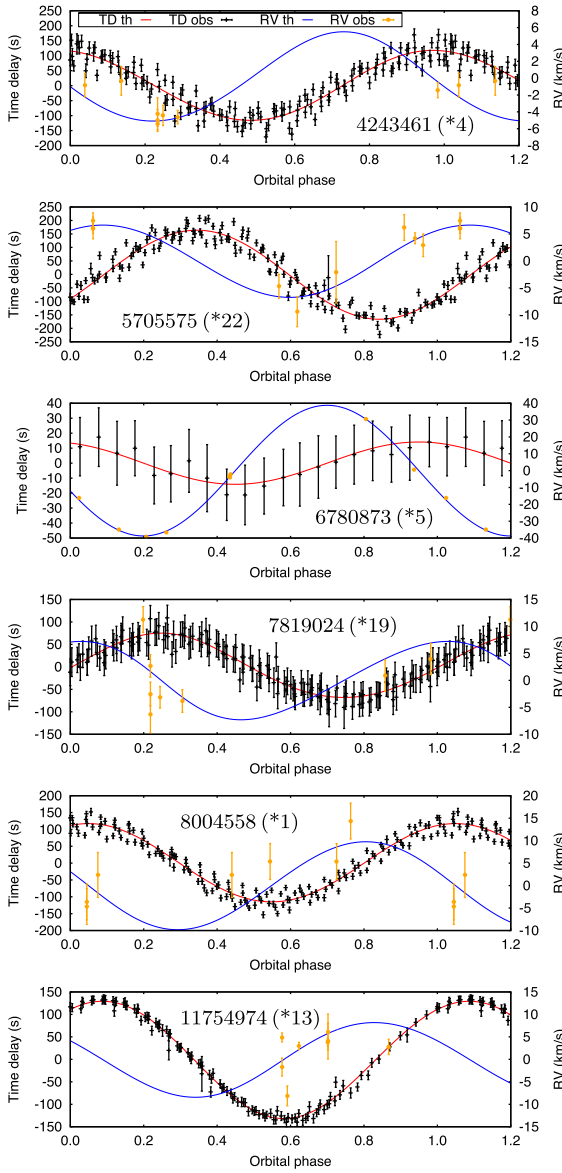


Figure 23. PM+RV analysis results for six wide binaries: TD and RV curves phased with the orbital periods given in Table 9. The RVs have been offset by the systemic RVs. Both the measured and fitted TDs (black points and red curves) and the measured and fitted RVs (yellow points and blue curves) are plotted.

binaries is a coalesced star, while the secondary is the third star in a triple system. Indirect evidence for the coalescence hypothesis comes from the presence in HR diagrams of various types of binary systems seen among the BSs found in globular clusters and dwarf galaxies (Mateo et al. 1990; Kaluzny et al. 2007, 2013; Rozyczka et al. 2010; Thompson et al. 2010). It would be interesting to know if any of the programme stars contain white dwarf companions of the sort recently observed in three BSs in the 7 Gyr-old open cluster NGC 188 (Gosnell et al. 2014).

3.3.3 Other SX Phe binaries

Approximately one-third of the BN12 sample of *Kepler*-field SX Phe stars (11 of 30 stars) have been found to be in binary systems with orbital periods ranging from a few days to several

Table 11. Radii and masses for the 34 programme stars. The radius and mass of the primary, R_1 and M_1 , are from table 5 of H14. The mass of the secondary, M_2 , was calculated by combining the mass function, $f_2(M_1, M_2, \sin i)$, from Table 9, with the H14 primary mass from column (4) and assuming $i = 90^\circ$; thus, the M_2 are lower limits. The KIC numbers of the binary systems are in boldface.

KIC no. (1)	CFHT no. (2)	R_1/R_\odot (H14) (3)	M_1/M_\odot (H14) (4)	M_2/M_\odot (this paper) (5)
1162150	15	4.31	2.09	
3456605	24	2.27	1.64	
4168579	23	2.78	1.94	
4243461	4	1.55	1.39	> 0.27
4662336	14	2.54	1.77	
4756040	20	1.97	1.74	
5036493	26	2.42	2.00	
5390069	–	[2.25]	[1.70]	
5705575	22	2.08	1.68	> 0.42
6130500	9	1.90	1.71	
6227118	27	11.32:	3.24:	
6445601	2	1.80	1.52	
6520969	21	3.03	2.01	
6780873	5	1.11	1.01	> 0.50
7020707	16	2.32	1.73	
7174372	8	1.77	1.46	> 0.01
7300184	–	[2.25]	[1.70]	
7301640	10	1.78	1.56	
7621759	6	1.99	1.52	
7765585	28	1.37	1.40	
7819024	19	1.83	1.53	
8004558	1	2.45	1.71	> 0.49
8110941	29	1.74	1.50	
8196006	30	1.35	1.27	
8330910	3	1.90	1.55	
9244992	7	3.93	1.87	
9267042	12	3.12	2.03	> 0.06
9535881	[25]	1.65	1.46	> 0.01
9966976	31	2.54	1.97	> 0.05
10989032	32	2.18	2.11	> 0.20
11649497	11	2.16	1.81	
11754974	13	2.23	1.73	> 0.46
12643589	[17]	1.12	1.15	> 0.01
12688835	18	2.88	1.97	

years. While these are not the first SX Phe stars in binary systems to be identified, the long baseline (4 yr) and high precision of the photometry has allowed us to define with great precision the orbits of several of the stars and their oscillations.

Other presently known SX Phe binaries (which exhibit a similarly large range of separations and types) include:

(1) four ‘blue metal poor’ (BMP) halo stars found by George Preston and his collaborators – CS 22966-043 (see Preston & Landolt 1998, 1999) that has an orbital period of ~ 319 d and pulsations closely resembling those of the SX Phe stars in the very metal-poor globular cluster NGC 5053 (Nemec et al. 1995), and CS 22871-040, CS 22896-103 and CS 29499-057 (Preston & Sneden 2000). Curiously, CS 22896-103 is not metal-poor but has a metallicity similar to the Sun, $[Fe/H] = -0.10$ dex, and is one of ~ 17 metal-rich BSs found among the sample of BMP stars studied by Preston & Sneden (see their tables 1 and 5).

(2) BL Cam, which from an analysis of its O–C diagram, is a multiperiodic low-metallicity high-amplitude SX Phe star and

was found to be in a 144.2 d close binary system, possibly orbited by a brown dwarf having an orbital period ~ 9.3 yr (Fauvaud et al. 2006, 2010);

(3) QU Sge in M71 is the first SX Phe binary found in a globular cluster (Jeon et al. 2006; see McCormac et al. 2014). It is a semide-tached Algol-type EB (orbital period 3.8 d) with ‘the secondary component fully filling its Roche lobe and the primary filling its Roche lobe by about 33 per cent’. After subtracting the eclipses, the primary star was seen to be an SX Phe star with two close frequencies, 35.883 and 39.867 d $^{-1}$ (corresponding to periods of 40.2 and 36.1 min, respectively) indicative of non-radial pulsations. Given that the mean [Fe/H] of M71 is near -0.80 dex, with a small (0.03 dex) standard deviation that suggests considerable homogeneity (Cordero et al. 2015, and references therein), it is reasonable to assume that QU Sge too has a similar metal abundance.

Relaxing the distinction between SX Phe and δ Sct stars, δ Sct binary systems were first identified over 40 yr ago. The first such identification was AB Cas, a δ Sct star in a 1.37 d Algol-type system (Tempesti 1971; Rodríguez et al. 1994, 1998), where the δ Sct star has a small amplitude range, $\Delta V \sim 0.05$ mag, and appears to be monoperiodic with $v = 17.16$ d $^{-1}$. Another early identification was Y Cam (See Broglia & Conconi 1984; Rodríguez et al. 2010), which shows several significant frequencies between 15 and 18 d $^{-1}$ (Kim et al. 2002). More recently, numerous low-amplitude δ Sct stars in EB systems have been identified by Rodríguez & Breger (2001), Mkrtchian et al. (2005) and Soydugan et al. (2006). The last of these papers identified 25 EBs containing low-amplitude (0.007–0.02 mag) δ Sct stars. Derekas et al. (2009) have investigated the question of binarity and multiperiodicity in 10 δ Sct (HADS) stars. Other recent studies include those by Southworth et al. (2011), Lampens et al. (2011), Hambleton et al. (2013), Debosscher et al. (2013) and Lee et al. (2016).

4 SUMMARY

Our goal was to characterize better the sample of 34 *Kepler*-field SX Phe stars identified by BN12. High-resolution spectra for 32 of the 34 stars were acquired and analysed, and all the available Q0-Q17 long- and SC *Kepler* photometry for the 34 stars were re-analysed.

RVs were derived from 184 programme star spectra (calibrated with 24 spectra of IAU standard stars). Approximately half of the stars show some evidence for RV variability. By combining the measured mean RVs with the tangential motions, U , V , W space motions were derived. Five of the stars were found to have large negative V -velocities and 29 of the 32 stars have a total space motion $T > 300$ km s $^{-1}$. All of the stars lie in the ‘galactic halo’ region of the Toomre diagram (except possibly KIC 6227118 that appears to lie in the ‘thick-disc’ region).

Also derived from the spectra were projected rotation velocities and macroturbulent velocities. Two-thirds of the stars are fast rotators with $v \sin i > 50$ km s $^{-1}$, including four stars with $v \sin i \geq 200$ km s $^{-1}$. Several stars were found to have macroturbulent velocities in the range 10–30 km s $^{-1}$; such turbulence may be an even larger contributor to observed broadening of spectral lines than rotation.

Other atmospheric parameters that were measured include T_{eff} , log g , v_{mic} and [Fe/H]; these spectroscopic estimates improve upon previous values, such as those that rely only on calibrations involving photometry (KIC, H14). The spectral types range from A2 to F2, corresponding to surface temperatures in the range 8600–6900 K.

The mean metallicity of the sample is near-solar, with only a few of the stars having a marked metal weakness; in this sense, the stars resemble the metal-rich A-stars (Perry 1969; Preston 2015). By analogy with metal-rich RR Lyrae stars, such as those found in metal-rich globular clusters, the BN12 sample can be characterized as ‘metal-rich SX Phe stars’. In fact, the existence of metal-rich SX Phe stars complements the recent finding by Torrealba et al. (2015) that suggests a higher concentration of more metal-rich stars near the galactic disc (see their figs 12 and 13).

SX Phe stars have, until now, been thought of as ‘metal-poor Population II variables that have high space velocities and fall in the BS domain of the colour–magnitude diagrams of globular clusters’ (McNamara 1995). The identification in this paper of *bona fide* metal-rich SX Phe stars suggests that the definition of such stars should not be limited to ‘metal-poor’ pulsators.

ACKNOWLEDGEMENTS

This paper is based on spectra acquired with the CFHT and the 3.5-m telescope at the APO, and on photometry from NASA’s *Kepler* mission and the Korean 1.8-m Bohyunsan Observatory. CFHT is operated by the National Research Council of Canada, the Institut National des Sciences de l’Univers of the Centre National de la Recherche Scientifique of France and the University of Hawaii. The CFHT pipeline, Upena, uses J.-F. Donati’s software LIBRE-ESPRIT (Donati et al. 1997). We wish to thank the CFHT time allocation committee for its generous awards of observing time and Nadine Manset and her team of service observers for making the ESPaDOnS observations. We also wish to thank Dr Suzanne Hawley, the director of the APO 3.5-m telescope which is owned and operated by the Astrophysical Research Consortium, for observing time, and the telescope operators for their assistance. Funding for the *Kepler* mission is provided by the NASA Science Mission directorate. The authors thank the *Kepler* team for their generosity in providing the photometric data and for their outstanding efforts which have made these results possible. JMN thanks Federico González for his ‘RCROS’ software (see Díaz et al. 2011) that was used for deriving the $v \sin i$ values, Dr Karen Kinemuchi for her hospitality at the Apache Point Observatory and at New Mexico State University, Dr Simón-Díaz for making public his IACOB software and the referee for useful comments. A special thanks is owed to Dr Amanda Linnell Nemec for helpful suggestions and for making critical readings of the paper. We also thank Drs Don Kurtz, Andrzej Pugalski, Conny Aerts and Patricia Lampens for useful discussions. JMN is grateful to the Camosun College Faculty Association for financial assistance. LAB wishes to thank the National Research Foundation and the South African Astronomical Observatory for financial support. SJM is supported by the Australian Research Council and by the Danish National Research Foundation and ASTERISK project (grant agreement numbers: DNRF106 and 267864, respectively). Some of the data presented in this paper were obtained from the Multimission Archive at the Space Telescope Science Institute (MAST). STScI is operated by the Association of Universities for Research in Astronomy, Inc., under NASA contract NAS5-26555. Support for MAST for non-*HST* data is provided by the NASA Office of Space Science via grant NNX09AF08G and by other grants and contracts. This research has also made use of the SIMBAD data base, operated at CDS, Strasbourg, France, of the Aladin Sky Atlas, and of the VALD3 data base (operated at Uppsala University, the Institute of Astronomy RAS in Moscow and the University of Vienna).

REFERENCES

- Adelman S., 2004, in Zverko J., Ziznovsky J., Adelman S. J., Weiss W. W., eds, Proc. IAU Symp. 224, The A-Star Puzzle. Kluwer, Dordrecht, p. 1
- Aerts C., 2015, *Astron. Nachr.*, 336, 477
- Aerts C., Puls J., Godart M., Dupret M.-A., 2009, *A&A*, 508, 409
- Aerts C., Simón-Díaz S., Groot P. J., Degroote P., 2014, *A&A*, 569, A118
- Asplund M., Grevesse N., Sauval A. J., Scott P., 2009, *ARA&A*, 47, 481
- Baily C. D., 1995, *ARA&A*, 33, 133
- Balona L. A., 2011, *MNRAS*, 415, 1691
- Balona L. A., 2013, *MNRAS*, 431, 2240 (B13)
- Balona L. A., 2014a, *MNRAS*, 437, 1476
- Balona L. A., 2014b, *MNRAS*, 443, 1946 (B14)
- Balona L. A., Dziembowski W., 2011, *MNRAS*, 417, 591
- Balona L. A., Nemec J. M., 2012, *MNRAS*, 426, 2413 (BN12)
- Balona L. A. et al., 2011, *MNRAS*, 413, 2403
- Balona L. A., Catanzaro G., Abedigamba O. P., Ripepi V., Smalley B., 2015, *MNRAS*, 448, 1378
- Bedding T. R., Murphy S. J., Colman I. L., Kurtz D. W., 2015, *EPJ Web Conf.*, 101, 01005
- Bensby T., Oey M. S., Feltzing S., Gustafsson B., 2007, *ApJ*, 655, L89
- Böhm-Vitense E., 1958, *Z. Astrophys.*, 46, 108
- Böhm-Vitense E., 1989, Introduction to Stellar Astrophysics, Vol. 2. Cambridge Univ. Press, Cambridge
- Böhm-Vitense E., Canterna R., 1974, *ApJ*, 194, 629
- Böhm-Vitense E., Nelson G. D., 1976, *ApJ*, 210, 741
- Böhm-Vitense E., Dettmann T., 1980, *ApJ*, 236, 560
- Breger M., 1975, *ApJ*, 201, 653
- Breger M., 1977a, *PASP*, 89, 55
- Breger M., 1977b, *PASP*, 89, 339
- Breger M., 1980, *ApJ*, 235, 153
- Breger M., Lenz P., Pamyatnykh A. A., 2013, *ApJ*, 773, 56
- Brewer J. M., Fischer D. A., Basu S., Valenti J. A., Piskunov N., 2015, *ApJ*, 805, 126
- Broglia P., Conconi P., 1984, *A&A*, 138, 443
- Brown T. M., Latham D. W., Everett M. E., Esquerdo G. A., 2011, *AJ*, 142, 112
- Bruntt H., Frandsen S., Gilliland R. L., Christensen-Dalsgaard J., Petersen J. O., Guhathakurta P., Edmonds P. D., Bono G., 2001, *A&A*, 371, 614
- Bruntt H. et al., 2002, *A&A*, 389, 345
- Bruntt H. et al., 2010a, *MNRAS*, 405, 1907
- Bruntt H. et al., 2010b, *A&A*, 519, A51
- Cantiello M. et al., 2009, *A&A*, 499, 279
- Carney B. W., Latham D. W., Laird J. B., Grant C. E., Morse J. A., 2001, *AJ*, 122, 3419
- Carney B. W., Latham D. W., Laird J. B., 2005, *AJ*, 129, 466
- Carollo D. et al., 2007, *Nature*, 450, 1020
- Carollo D. et al., 2010, *ApJ*, 712, 692
- Carollo D. et al., 2016, *Nature Phys.*, 12, 1170
- Carroll J. A., 1928, *MNRAS*, 553, 1928
- Carroll J. A., 1933, *MNRAS*, 93, 478
- Castelli F., Kurucz R. L., 2004, preprint ([arXiv:astro-ph/0405087](https://arxiv.org/abs/astro-ph/0405087))
- Catanzaro G. et al., 2011, *MNRAS*, 411, 1167
- Chaplin W. J., Elsworth Y., Davies G. R., Campante T. L., Handberg R., Miglio A., Basu S., 2014, *MNRAS*, 445, 946
- Cohen R. E., Sarajedini A., 2012, *MNRAS*, 419, 342
- Conroy K. E., Prša A., Stassun K. G., Orosz J. A., Fabrycky D. C., Welsh W. F., 2014, *AJ*, 147, 45
- Coppola G. et al., 2015, *ApJ*, 814, 71
- Cordero M. J., Pilachowski C. A., Johnson C. I., Vesperini E., 2015, *ApJ*, 800, 3
- Coşkunoğlu B. et al., 2011, *MNRAS*, 412, 1237
- Dall T. H., Bruntt H., Stello D., Strassmeier K. G., 2010, *A&A*, 514, A25
- Da Costa G. S., Norris J., Villumsen J. V., 1986, *ApJ*, 308, 743
- de Jager C., 1990, *Sol. Phys.*, 126, 201
- Debosscher J. et al., 2013, *A&A*, 556, A56
- Demory B.-O. et al., 2009 *A&A*, 505, 205
- Derekas A. et al., 2009, *MNRAS*, 394, 995
- Díaz C. G., González F., Levato H., Grossi M., 2011, *A&A*, 531, A143
- Donati J.-F., Landstreet J., 2009, *ARA&A*, 47, 333
- Donati J.-F., Semel M., Carter B. D., Rees D. E., Collier Cameron A., 1997, *MNRAS*, 291, 658
- Doyle A. P., Davies G. R., Smalley B., Chaplin W. J., Elsworth Y., 2014, *MNRAS*, 444, 3592
- Dravins D., 1982, *ARA&A*, 20, 61
- Dupret M.-A., Grigahcène A., Garrido R., Gabriel M., Scuflaire R., 2004, *A&A*, 414, L17
- Duquennoy A., Mayor M., 1991, *A&A*, 248, 485
- Eggen O. J., 1970, *PASP*, 82, 274
- Eggen O. J., 1979, *ApJS*, 41, 413
- Eggen O. J., Iben I., 1989, *AJ*, 97, 431
- Everett M. E., Howell S. B., Kinemuchi K., 2012, *PASP*, 316
- Fauvaud S. et al., 2006, *A&A*, 451, 999
- Fauvaud S. et al., 2010, *A&A*, 515, A39
- Ferraro F. R. et al., 2006, *ApJ*, 647, L53
- Ferraro F. R., Lanzoni B., Dalessandro E., Mucciarelli A., Lovisi L., 2015, *Astrophysics Space Science Library*, Vol. 413, Ecology of Blue Straggler Stars, Springer-Verlag, Berlin, Heidelberg, p. 99
- Fiorentino G., Lanzoni B., Dalessandro E., Ferraro F. R., Bono G., Marconi M., 2014, *ApJ*, 783, 34
- Fiorentino G., Marconi M., Bono G., Dalessandro E., Ferraro F. R., Lanzoni B., Lovisi L., Mucciarelli A., 2015, *ApJ*, 810, 15
- Fusi Pecci F., Ferraro F. R., Corsi C. E., Cacciari C., Buonanno R., 1992, *AJ*, 104, 1831
- Gilliland R. L., Bono G., Edmonds P. D., Caputo F., Cassisi S., Petro L. D., Saha A., Shara M. M., 1998, *ApJ*, 507, 818
- Gosnell N., Mathieu R. D., Geller A. M., Sills A., Leigh N., Knigge C., 2014, *ApJ*, 783, L8
- Grassitelli L., Fossati L., Langer N., Miglio A., Istrate A. G., Sanyal D., 2015, *A&A*, 584, L2
- Gray D. F., 1973, *ApJ*, 184, 461
- Gray D. F., 1975, *ApJ*, 202, 148
- Gray D. F., 1978, *Sol. Phys.*, 59, 193
- Gray D. F., 1988, Lectures on Spectral Line Analysis: F, G and K Stars. Arva, Ontario
- Gray D. F., 2005, The Observation and Analysis of Stellar Photospheres, 3rd edn. Cambridge Univ. Press, Cambridge
- Gray D. F., 2009, *ApJ*, 697, 1032
- Gray D. F., 2014, *AJ*, 147, 81
- Gray R. O., Corbally C. J., 1994, *AJ*, 107, 742
- Gray R. O., Corbally J. C., 2009, Stellar Spectral Classification. Princeton Univ. Press, Princeton, NJ
- Gray D. F., Nagle T., 1989, *ApJ*, 341, 421
- Gray D. F., Toner C. G., 1986, *ApJ*, 310, 277
- Gray R. O., Garrison R. F., 1989, *ApJS*, 70, 623
- Gray R. O., Graham P. W., Hoyt S. R., 2001, *AJ*, 121, 2159
- Green G. M. et al., 2014, *ApJ*, 783, 114
- Green G. M. et al., 2015, *ApJ*, 810, 25
- Greiss S. et al., 2012, *AJ*, 144, 24 (KIS)
- Guzik J. A., Kaye A. B., Bradley P. A., Cox A. N., Neuforge C., 2000, *ApJ*, 542, L57
- Hambleton K. M. et al., 2013 *MNRAS*, 434, 925
- Helt B. E., Jorgensen H. E., King S., Larsen A., 1993, *A&A*, 270, 297
- Hobbs L. M., Mathieu R. D., 1991, *PASP*, 103, 431
- Hodder P. J. C., Nemec J. M., Richer H. B., Fahrlan G. G., 1992 *AJ*, 103, 460
- Hoyle F., 1964, *R. Obs. Bull.*, 82, 90
- Huber D. et al., 2014, *ApJS*, 211, 2 (H14)
- Iben I., Jr, 1986, *Mem. Soc. Astron. Ital.*, 57, 453
- Iben I., Jr, Tutukov A. V., 1984, *ApJ*, 284, 719
- Jensen K. S., Jørgensen H. L., 1985, *A&AS*, 60, 229
- Jeon Y.-B., Lee M. G., Kim S.-L., Lee H., 2004, *AJ*, 128, 287
- Jeon Y.-B., Kim S.-L., Lee M. G., Lee H., Lee J. W., 2006, *ApJ*, 636, L129
- Johnson D. O., 2004, *J. Astron. Data*, 10, 3
- Johnson D. R. H., Soderblom D. R., 1987, *AJ*, 93, 864
- Jørgensen H. E., 1982, *A&A*, 108, 99

- Jørgensen H. E., Hansen L., 1984, A&A, 133, 165
- Kallrath J., Milone E. F., Stagg C. R., 1992, ApJ, 389, 590
- Kaluzny J., 2000, in Szabados L., Kurtz D., eds, ASP Conf. Ser. Vol. 203, The Impact of Large-Scale Surveys on Pulsating Star Research. Astron. Soc. Pac., San Francisco, p. 19
- Kaluzny J., Kubiak M., Szymanski M., Udalski A., Krzeminski W., Mateo M., 1996, A&AS, 120, 139
- Kaluzny J., Rucinski S. M., Thompson I. B., Pych W., Krzeminski W., 2007, AJ, 133, 2457
- Kaluzny J., Rozyczka M., Pych W., Krzeminski W., Zloczewski K., Narloch W., Thompson I. B., 2013, Acta Astron., 63, 309
- Kim S.-L., Lee J. W., Youn J.-H., Kwon S.-G., Kim C., 2002, A&A, 391, 213
- Koen C., 2014, MNRAS, 444, 1486
- Kupka F., Piskunov N., Ryabchikova T. A., Stempels H. C., Weiss W. W., 1999, A&AS, 138, 119
- Kurtz D., Shibahashi H., Murphy S. J., Bedding T. R., Bowman D. M., 2015, MNRAS, 450, 3015
- Kurtz M. J., Mink D. J., 1998, PASP, 110, 934
- Lampens P. et al., 2011, A&A, 534, A111
- Landstreet J. D., 1998, A&A 338, 1041
- Landstreet J. D., Kupka F., Ford H. A., Officer T., Sigut T. A. A., Silaj J., Strasser S., Townshend A., 2009, A&A, 503, 973
- Lee J. W., Hong K., Kim S.-L., Koo J.-R., 2016, MNRAS, 460, 4220
- Leigh N., Sills A., Knigge C., 2011, MNRAS, 416, 1410
- Lenz P., Breger M., 2005, Commun. Asteroseismol., 146, 53
- Leonard P. J. T., 1989, AJ, 98, 217
- Lucy L. B., 1976, ApJ, 206, 499
- Mccormac J., Skillen I., Pollacco D., Faedi F., Ramsay G., Dhillon V. S., Todd I., Gonzalez A., 2014, MNRAS, 438, 3383
- McCrea W. H., 1964, MNRAS, 128, 147
- McNamara D. H., 1995, AJ, 109, 1751
- McNamara D. H., 1997, PASP, 109, 1221
- McNamara D. H., 2011, AJ, 142, 110
- McNamara D. H., Feltz F. A., Jr, 1978, PASP, 90, 275
- McNamara D. H., Clementini G., Marconi M., 2007, AJ, 133, 2752
- Margon B., Cannon R. D., 1989, Observatory, 109, 82
- Markova N., Puls J., Simón-Díaz S., Herrero A., Markov H., Langer N., 2014, A&A, 562, A37
- Martínez-Vázquez C. E. et al., 2016 MNRAS, 462, 4349
- Massarotti A., Latham D. W., Stefanik R. P., Fogel J., 2008, AJ, 135, 209
- Mateo M., Harris H. C., Nemec J., Olszewski E. W., 1990, AJ, 100, 469
- Mateo M., Hurley-Keller D., Nemec J., 1998, AJ, 115, 1856
- Matijević G., Prša A., Orosz J. A., Welsh W. F., Bloemen S., Barclay T., 2012, AJ, 143, 123
- Mazur B., Krzeminski W., Thompson I. B., 2003, MNRAS, 340, 1205
- Michaud G., Charland Y., Vauclair S., Vauclair G., 1976, ApJ, 210, 447
- Mkrtichian D. E., Rodríguez E., Olson E. C., Kusakin A. V., Kim S.-L., Lehmann H., Gamarova A. Y., Kang Y. W. 2005 in Claret A., Giménez A., Zahn J.-P., eds, ASP Conf. Ser. Vol. 333, Tidal Evolution and Oscillations in Binary Stars. Astron. Soc. Pac., San Francisco, p. 197
- Momany Y., 2015, Astrophysics Space Science Library, Vol. 443, Ecology of Blue Straggler Stars. Springer-Verlag, Berlin, Heidelberg, p. 129
- Morris S. L., 1985, ApJ, 295, 143
- Murphy S. J., 2012, MNRAS, 422, 665
- Murphy S. J., Shibahashi H., 2015, MNRAS, 450, 4475
- Murphy S. J., Shibahashi H., Kurtz D. W., 2013a, MNRAS, 430, 2986
- Murphy S. J. et al., 2013b, MNRAS, 432, 2284 (M13)
- Murphy S. J., Bedding T. R., Shibahashi H., Kurtz D. W., Kjeldsen H., 2014, MNRAS, 441, 2515
- Murphy S. J., Bedding T. R., Niemczura E., Kurtz D. W., Smalley B., 2015a, MNRAS, 447, 3948
- Murphy S. J., Shibahashi H., Bedding T. R., 2016, MNRAS, 461, 4215
- Nemec J. M., 1989, in Schmidt E. G., ed., The Use of Pulsating Stars in Fundamental Programs in Astronomy. Cambridge Univ. Press, Cambridge, p. 215
- Nemec J. M., Cohen J. G., 1989, ApJ, 336, 780
- Nemec J. M., Harris H. C., 1987, ApJ, 316, 172
- Nemec J. M., Linnell Nemec A. F., 1991, PASP, 103, 95
- Nemec J. M., Linnell Nemec A. F., 1993, AJ, 105, 1455
- Nemec J. M., Mateo M., 1990a, in Kron R. G., ed., ASP Conf. Ser. Vol. 10, Evolution of the Universe of Galaxies. Astron. Soc. Pac., San Francisco, p. 134
- Nemec J. M., Mateo M., 1990b, in Cacciari C., Clementini G., eds, ASP Conf. Ser. Vol. 11, Confrontation between Stellar Pulsation and Evolution. Astron. Soc. Pac., San Francisco, p. 64
- Nemec J. M., Nemec A. F. L., Lutz T. E., 1994, AJ, 108, 222
- Nemec J. M., Mateo M., Burke M., Olszewski E. W., 1995, AJ, 110, 1186
- Nemec J. M., Cohen J. G., Ripepi V., Derekas A., Moskalik P., Sesar B., Chadiid M., Bruntt H., 2013, ApJ, 773, 181
- Nemec J. M., Balona L. A., Kinemuchi K., Murphy S. J., Jeon Y.-B., Kurtz D. W., Pigulski A., 2015, EPJ Web Conf., 101, 06049
- Nidever D. L., Marcy G. W., Butler R. P., Fischer D. A., Vogt S. S., 2002, ApJS, 141, 503
- Nielsen M. B., Gizon L., Schunker H., Karoff C., 2013, A&A, 557, L10
- Niss B., 1981, A&A, 98, 415
- Niss B., Jørgensen H. E., Laustsen S., 1978, A&AS, 32, 387
- Olech A., Dziembowski W. A., Pamyatnykh A. A., Kaluzny J., Pych W., Schwarzenberg-Czerny A., Thompson I. B., 2005, MNRAS, 363, 40
- Palaversa L. et al., 2013, AJ, 146, 101
- Park N.-K., Nemec J. M., 2000, AJ, 119, 1803
- Paxton B., Bildsten L., Dotter A., Herwig F., Lesaffre P., Timmes F., 2011, ApJS, 192, 3
- Paxton B. et al., 2013, ApJS, 208, 4
- Paxton B. et al., 2015, ApJS, 220, 15
- Perets H. B., Fabrycky D. C., 2009, ApJ, 697, 1048
- Perry C. L., 1969, AJ, 74, 139
- Petersen J. O., Hog E., 1998, Mem. Soc. Astron. Ital., 69, 59
- Pinsonneault M. H., An D., Molenda-Zakowicz J., Chaplin W. J., Metcalfe T. S., Bruntt H., 2012, ApJS, 199, 30
- Piskunov N. E., Kupka F., Ryabchikova T. A., Weiss W. W., Jeffery C. S., 1995, A&AS, 112, 525
- Poretti E. et al., 2008, ApJ, 685, 947
- Poznanski D., Prochaska J. X., Bloom J. S., 2012, MNRAS, 426, 1465
- Press W. H., Rybicki G. B., 1989, ApJ, 338, 277
- Preston G. W., 1974, ARA&A, 12, 257
- Preston G. W., 2015, Astrophysics Space Science Library, Vol. 443, Ecology of Blue Straggler Stars. Springer-Verlag, Berlin, Heidelberg, p. 65
- Preston G. W., Landolt A. U., 1998, AJ, 115, 2515
- Preston G. W., Landolt A. U., 1999, AJ, 118, 3006
- Preston G. W., Sneden C., 2000, AJ, 120, 1014
- Preston G. W., Beers T. C., Shectman S. A., 1994, AJ, 108, 538
- Prša A. et al., 2011, AJ, 141, 83
- Pych W., Kaluzny J., Krzeminski W., Schwarzenberg-Czerny A., Thompson I. B., 2001, A&A, 367, 148
- Ramírez I., Allende Prieto C., Lambert D. L., 2013, ApJ, 764, 78
- Ramsay G., Napiotzki R., Barclay T., Hakala P., Potter S., Cropper M., 2011, MNRAS, 417, 400
- Reiners A., Royer F., 2004, A&A, 415, 325
- Reiners A., Schmitt J. H. M. M., 2002, A&A, 384, 155
- Rodríguez E., Breger M., 2001, A&A, 366, 178
- Rodríguez E., López-González M. J., 2000, A&A, 359, 597
- Rodríguez E., Lopez de Coca P., Rolland A., Garrido R., Costa V., 1994, A&A, 106, 21
- Rodríguez E., Claret A., Sedano J. L., Garcia J. M., Garrido R., 1998, A&A, 340, 196
- Rodríguez E. et al., 2010, MNRAS, 408, 2149
- Royer F., Zorec J., Gómez A. E., 2007, A&A, 463, 671
- Rozyczka M., Kaluzny J., Pietrukowicz P., Pych W., Catelan M., Contreras C., Thompson I. B., 2010, A&A, 524, A78
- Rucinski S., 1999, in Hearnshaw J. B., Scarfe C. D., eds, ASP Conf. Ser. Vol. 185, IAU Colloq. 170: Precise Stellar Radial Velocities. Astron. Soc. Pac., San Francisco, p. 82
- Ryans R. S. I., Dufton P. L., Rolleston W. R. J., Lennon D. J., Keenan F. P., Smoker J. V., Lambert D. L., 2002, MNRAS, 336, 577

- Saar S. H., Osten R. A., 1997, MNRAS, 284, 803
 Saio H., Kurtz D. W., Takata M., Shibahashi H., Murphy S. J., Sekii T.,
 Bedding T. R., 2015, MNRAS, 443, 1946
 Sandage A. R., Fouts G., 1987, AJ, 93, 74
 Sandage A. R., Tammann G., 2006, ARA&A, 44, 93
 Sarajedini A., 1993, PhD thesis, Yale Univ.
 Schiode J. H., Quataert E., Cantiello M., Bildsten L., 2013, MNRAS, 430,
 1736
 Schlafly E. F., Finkbeiner D. P., 2011, ApJ, 737, 103
 Schlegel D. J., Finkbeiner D. P., Davis M., 1998, ApJ, 500, 525
 Schuster W. J., Moreno E., Nissen P. E., Pichardo B., 2012, A&A, 538, A21
 Shibahashi H., Kurtz D. W., 2012, MNRAS, 422, 738
 Shibahashi H., Kurtz D. W., Murphy S. J., 2015, MNRAS, 450, 3999
 Simón-Díaz S., Herrero A., 2007, A&A, 468, 1063
 Simón-Díaz S., Herrero A., 2014, A&A, 562, A135
 Simón-Díaz S., Herrero A., Uytterhoeven K., Castro N., Aerts C., Puls J.,
 2010, ApJ, 720, L174
 Slawson R. W. et al., 2011, AJ, 142, 160
 Smalley B., 2004, in Zverko J., Ziznovsky J., Adelman S. J., Weiss W. W.,
 eds, Proc. IAU Symp. 224, The A-Star Puzzle. Cambridge Univ. Press,
 Cambridge, p. 131
 Smith M. A., Gray D. F., 1976, PASP, 88, 809
 Sneden C., 1973, ApJ, 184, 839
 Soszynski I. et al., 2002, Acta Astron., 52, 369
 Soszynski I. et al., 2003, Acta Astron., 53, 93
 Sousa S. G., Santos N. C., Israeli G., Mayor M., Monteiro M. J. P. F. G.,
 2007, A&A, 469, 783
 Sousa S. G., Santos N. C., Adibekyan V., Delgado-Mena E., Israeli G.,
 2015, A&A, 577, A67
 Southworth J. et al., 2011, MNRAS, 414, 2413
 Soydugan E., Soydugan F., Demircan O., Ibanoglu C., 2006, MNRAS, 370,
 2013
 Struve O., Elvey C. T., 1934, ApJ, 79, 409
 Telting J. H. et al., 2012, A&A, 544, A1
 Tempesta P., 1971, Inf. Bull. Var. Stars, 596, 1
 Thompson I., Kaluzny J., Rucinski S. M., Krzeminski W., Pych W., Dotter
 A., Burley G. S., 2010, AJ, 139, 329
 Tillich A., Przybilla N., Scholz R.-D., Heber U., 2010, A&A, 517, A36
 Tonry J. L., Davis M., 1979, AJ, 84, 1511
 Torrealba G. et al., 2015, MNRAS, 2251
 Torres G., Fischer D. A., Sozzetti A., Buchhave L. A., Winn J. N., Holman
 M. J., Carter J. A., 2012, ApJ, 757, 161
 Udry S., Mayor M., Queloz D., 1999, in Hearnshaw J. B., Scarfe C. D.,
 eds, ASP Conf. Ser. Vol. 185, IAU Colloq. 170: Precise Stellar Radial
 Velocities. Astron. Soc. Pac., San Francisco, p. 383
 Valenti J. A., Fischer D. A., 2005, ApJS, 159, 141
 Valenti J. A., Piskunov N., 1996, A&AS, 118, 595
 Venn K., Irwin M., Shetrone M. D., Tout C. A., Hill V., Tolstoy E., 2004,
 AJ, 128, 1177
 Vivas A. K., Mateo M., 2013, AJ, 146, 141
 Yan L., Mateo M., 1994, AJ, 108, 1810
 Zacharias N. et al., 2010, AJ, 139, 2184

This paper has been typeset from a TeX/LaTeX file prepared by the author.